Dielectric and Hybrid Metal-Dielectric Nanoantennas for Fluorescence Enhancement

Dmitriev Pavel

School of Electrical & Electronic Engineering

A thesis submitted to the Nanyang Technological University
in partial fulfillment of the requirements for the degree of
Doctor of Philosophy

2022

Statement of Originality

I hereby certify that the work embodied in this thesis is the result of original research, is free of plagiarised materials, and has not been submitted for a higher degree to any other University or Institution.

September 14, 2022

Date

Dmitriev Pavel

Supervisor Declaration Statement

I have reviewed the content and presentation style of this thesis and declare it is free of plagiarism and of sufficient grammatical clarity to be examined. To the best of my knowledge, the research and writing are those of the candidate except as acknowledged in the Author Attribution Statement. I confirm that the investigations were conducted in accord with the ethics policies and integrity standards of Nanyang Technological University and that the research data are presented honestly and without prejudice.

15.09.2022

.....

Date

.....

Prof. Hilmi Volkan Demir

Authorship Attribution Statement

This thesis does not contain any materials from papers published in peer-reviewed journals or from papers accepted at conferences in which I am listed as an author.

The material presented in Chapter 4 and parts of Chapter 3 is currently being peer-reviewed for publication in ACS Photonics, with a pre-print available at [1], with the following co-authors: **Pavel A. Dmitriev**, Emmanuel Lassalle, Darren C. J. Neo, Lu Ding, Vytautas Valuckas, Ramón Paniagua-Dominguez, Joel K. W. Yang, Hilmi Volkan Demir and Arseniy I. Kuznetsov.

The contributions of the co-authors are as follows:

- P.D., E.L., R.P.-D., H.V.D. and A.I.K. developed the concept.
- R.P.-D., J.K.W.Y., H.V.D. and A.I.K supervised and coordinated the work.
- P.D. fabricated all the nanostructures and performed the SEM and all the optical measurements of the fabricated structures.
- E.L. developed the code based on reciprocity principle for the emission calculations and performed the numerical simulations of radiative emission spectra and emission patterns and designed the nanoantenna. E.L. also performed the quasi-normal mode analysis and the computation of the scattering cross-sections spectra. P.D. also performed the calculations of the field enhancement in excitation configuration, some scattering cross-section calculations, as well as some emission spectra and emission patterns calculations.
- L.D. provided support and supervised some of the optical measurements.
- D.C.J.N. synthesized the QDs and helped to spin coat them onto the samples.
- V.V. helped with SEM measurements.
- P.D. and E.L. wrote the manuscript, and all co-authors participated in results interpretation and read and reviewed the manuscript.

. September 14,. 2022 .

Date

Dmitriev Pavel

Acknowledgements

I wish to express my sincerest gratitude to my supervisors, for giving me the opportunity to pursue my graduate studies, and more importantly, for believing in me and letting me continue even when the outlook was bleak.

I want to thank my supervisors, Professor Hilmi Volkan Demir and Dr. Joel K. W. Yang, for all the positive reinforcement they gave during our discussions, both in-person and via teleconferencing, despite my overly aggressive and consistently missed timelines .

I thank my supervisor, Dr. Arseniy Kuznetsov, for helping me see the big picture when I would get bogged down with all the minor setbacks that any PhD project is sure to be riddled with.

I want to thank my advisor, Dr. Ramon Paniagua-Dominguez, for the countless hours he dedicated to repeatedly answering simple questions, reading my sloppily written manuscripts, and overall keeping me motivated and moving in the right direction.

This thesis would not be possible without the help of Dr. Lu Ding and Dr. Emmanuel Lassalle, their guidance helped me get through many challenges that, were I to be on my own, would have been insurmountable.

Dr. Egor Khaidarov deserves a special mention, for his scepticism and constant questioning the feasibility of my ideas helped keep my goals in the realm of science and not science fiction.

I would like to thank Dr. Jinfa Ho, Dr. Dmitry Kalashnikov, Dr. Darren C. J. Neo, Dr. Alok Ranjan, Dr. Ha Son Tung, Mr. Vytautas Valuckas, Dr. Viktor Leong, Dr. Anton Baranikov, Dr. Anna Paterova and all other current and former IMRE staff who helped me navigate the complexities of all the fabrication processes

and characterization experiments that I needed to master to complete my thesis projects.

In addition, I would like to express my gratitude to the NTU Luminous! Centre of Excellence for Semiconductor Lighting and Displays and NTU FACTS staff for entertaining my wildest experimental ideas, even if they didn't always succeed.

I would also like to thank Ms. Vino Prabakaran for her indispensable assistance dealing with all university administrative matters.

I have to mention my undergraduate supervisor Dr. Anton Samusev and the Department of Physics of ITMO University for introducing me to experimental physics and setting me off on this PhD journey.

And of course, I want to thank my family, most notably my mother, Renata Dmitrieva and my cousin Daniil Kitchaev, for helping me grow up curious about the world, giving me advice and constantly supporting me during these past five years.

And Finally, I want to thank Anastasia Cheong for helping me stay sane and tolerating my increasingly odd working hours, mounting stress and incoherent explanations of why my deadlines kept slipping.

Pavel Dmitriev, December 2021

Abstract

Fluorescence enhancement of localized light sources is important for both fundamental science, e.g. for study of quantum emitters and strong coupling effects, and for practical applications, e.g. for detection systems in genome sequencing or bioimaging. Traditionally, plasmonic nanostructures have been used for fluorescence enhancement applications. Plasmonic nanoantennas demonstrate very strong field confinement, but suffer from large dissipation losses. Plasmonic structures are typically limited to electric resonances, which makes designing nanoantennas for specific radiation patterns a very difficult task. Newer dielectric nanophotonic structures nearly eliminate dissipative losses and have greater flexibility in resonance tuning including both electric and magnetic resonances, but are unable to match the field confinement of their plasmonic counterparts.

In this thesis I experimentally demonstrate two approaches to combining plasmonic and dielectric nanostructures, harnessing the strengths of each to create a nanoantenna capable of providing both high enhancement factors and high out-of-plane directivity. One approach is based on coupling two standard plasmonic and dielectric nanostructures and optimizing their interaction, while the second approach is a proof-of-concept of a novel design of hybrid plasmonic-dielectric nanoantenna.

In the first approach I took two canonical antenna designs, a gold bowtie nanoantenna and a silicon ring nanoantenna and developed techniques to optimize their geometries to work as single efficient hybrid nanoantenna. Since the resulting structure geometry has many degrees of freedom, brute force scanning of parameters was not a feasible way of achieving an optimal design, so more elaborate iterative approaches were developed. Having achieved an optimal design, fabrication was the next hurdle to overcome, because of the complexity of integrating several distinct nanostructures on the same substrate. After fabrication, expected antenna performance was characterized by optical measurements.

In parallel, several techniques for the integration of my hybrid antenna with quantum emitters were being explored, from simple spin coating of quantum dots, to

precise fabrication of single quantum emitters via FIB. Ultimately, the full process of fabricating the hybrid nanoantenna and integration with quantum emitters was experimentally demonstrated, though the overall complexity was deemed too high.

Therefore focus shifted to a different approach, using a concept that drastically simplified the antenna fabrication process – replacing the gold bowtie nanoantenna integrated into the hybrid structure by a gold mirror placed under the silicon ring portion of the antenna. This also had the additional effect of simplifying the integration of quantum emitters with the hybrid structure, giving me more freedom to choose from all of the explored techniques.

Finally, the resulting silicon ring on gold mirror antenna structure was fabricated and coupled to quantum dots positioned beneath the silicon ring, and the structures high directional enhancement factor, as well as capabilities to tune the nanoantenna's directivity were demonstrated.

Contents

List of Figures

List of Tables

Symbols and Acronyms

Symbols

Acronyms

ACN	acetonitrile
AFM	atomic force microscopy
ALD	atomic layer deposition
APD	avalanche photodetector
BFP	back focal plane
CMOS	complementary metal-oxide–semiconductor
CVD	chemical vapor deposition
CW	continuous wave
DC	direct current
DF	dark field
EBL	electron beam lithography
EBPVD	electron beam physical vapor deposition
EF	enhancement factor
EG	ethylene glycol
EM	electromagnetic
EMCCD	electron multiplying charge-coupled device
EUV	extreme ultra violet
FDTD	finite-difference time-domain
FIB	focued ion beam
FS	fluorescent spheres
FWHM	full width at half maximum
HF	hydrogen fluoride

HSQ	hydrogen silsesquioxane
ICP	inductively coupled plasma
IPA	isopropyl alcohol
IR	infrared
IRF	instrument response function
ITO	indium tin oxide
LDOS	local density of states
MBE	molecular beam epitaxy
MIBK	methyl isobutyl ketone
MMP	multiple multipole
NA	numerical aperture
NIR	near infrared
NSOM	nearfield scanning optical microscopy
NPL	nanoplatelet
PL	photoluminescence
PMMA	poly(methyl methacrylate)
QD	quantum dot
QE	quantum efficiency
QNM	quasi-normal modes
QY	quantum yield
RF	radio frequency
RIE	reactive ion etching
SEM	scanning electron microscopy
SERS	surface-enhanced raman scattering
SPE	single photon emitter
SRR	split-ring resonator
STM	scanning tunneling microscope
TCSPC	time-correlated single photon counting
TE	transverse electric
TM	transverse magnetic
UV	ultraviolet
VIS	visible

Chapter 1

Introduction

1.1 Background

Fluorescence, or Photoluminescence is the emission of light by a substance after absorbing some form of light [2]. Typically, the emitted light has lower photon energy, and thus longer wavelength than the absorbed, excitation light, though certain non-linear effects allow for higher harmonic generation through the interaction of multiple photons. A Jablonksi diagram demonstrating the excitation, followed by non-radiative decay and light emission by a molecule is shown on Figure 1.1A.

Fluorescent molecules, fluorophores, are commonly used in life sciences as fluorescent markers that bind to studied molecules and are then detected by an imaging or spectroscopic setup. The applications for such fluorescent markers are numerous — DNA sequencing [3], glucose monitoring [4], tracking cell and protein interactions [5] and more.

Fluorescent quantum dots have been used in Light-emitting diodes (LED) [7] and fluorescent color defects in nanodiamonds have applications in quantum computing and quantum communications [8, 9].

Fluorescent molecules, quantum dots, and other nanoscale, localized light sources or quantum emitters tend to emit very weak signals, making their detection a challenge. A schematic of a typical microscopy setup used from fluorescence spectroscopy or fluorescence imaging is shown on Figure 1.1B. In such a setup, a fluorescent sample is excited by a laser and the fluorescence signal is collected by an

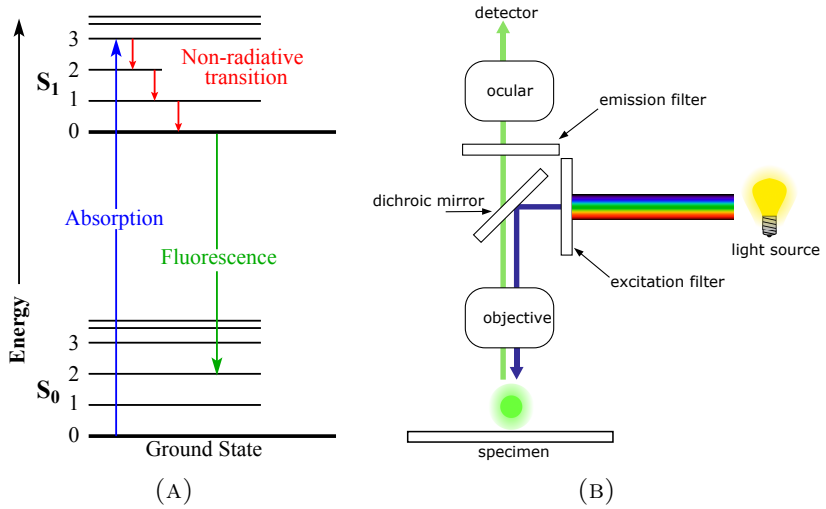

(A) (B)

FIGURE 1.1: **A** Energy diagram demonstrating the process of fluorescence. **B** Schematic diagram showing a typical spectroscopy microscope setup. Reproduced with permission from [6]

objective lens and sent to a detector for analysis. Because of the limited collection angle of the objective lens, only light emitted into the collection angle can be detected. To address this issue, one must first enhance the light emission from the quantum emitters and second, direct the emission into the collection angle of detection setup.

Nanostructures called optical nanoantennas are capable of addressing these challenges. These are resonant structures designed to enhance and shape light emission [10, 11, 12, 13, 14, 15, 16].

The study of nanostructures for fluorescence enhancement of quantum emitters is important from both a fundamental perspective, e.g. for the study of single quantum emitters and their interactions [11, 13, 17], and from a very practical, applied perspective, e.g. for fast and accurate biological sensing for medical applications [17, 18, 19, 20, 21, 22, 23], making sensing down to the single molecule level feasible.

A brief introduction to the topic of nanoantennas will be given in the first part of the introduction, where I highlight the different approaches to nanoantenna design, their pros and cons and their key differentiating factors.

Another important part in fluorescence enhancement of quantum emitters is the positioning of the emitters close enough to the antenna structures to actually be able to interact. Ideally, one would like to bring the emitters to those regions of the nanoantennas where the enhancement is maximum, the so-called “hot spots”.

This task, however, is highly complicated, as will be explained in the second part of the introduction.

1.2 Nanoantennas

The size mismatch between single quantum emitters, which can go down to single nanometers in size, and light, which is usually around several hundreds of nanometers, makes interactions between the two difficult and inefficient [18, 24]. Optical nanoantennas have proven to be essential to nanoscale light manipulation, including, among others, highly directional light scattering and fluorescence enhancement from localized light sources, both biological [25, 26, 27] and solid state [28, 29, 30].

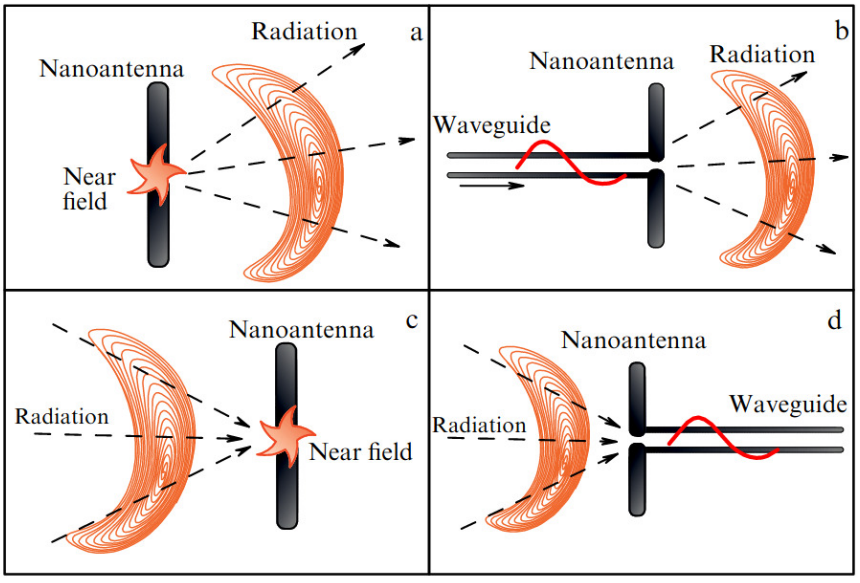

FIGURE 1.2: Principal applications of nanoantennas (exemplified by a dipole). Near field (a) or waveguide mode (b) transformation into freely propagating optical radiation; (c, d) illustrate a reception regime. Figure reproduced with permission from Ref. [31]

Classical antennas are used to transmit and receive radio-frequency electromagnetic radiation and convert it to electric signals for further processing. Optical antennas, similarly, are designed to interact with free propagating radiation and convert it to localized, near-field electromagnetic radiation, at optical (UV, VIS, IR) wavelengths (see Figure 1.2) [31, 32, 33].

Optical nanoantennas can be described by their two main properties, Directivity (D) and Radiation Efficiency (η_{rad}) [31, 33, 2]:

$$D = \frac{4\pi}{P_{\text{rad}}} \max[p(\theta, \phi)] \tag{1.1}$$

$$\eta_{\text{rad}} = \frac{P_{\text{rad}}}{P_{\text{rad}} + P_{\text{loss}}} \tag{1.2}$$

$$P_{rad} = \int_0^{2\pi} \int_0^{2\pi} p(\theta, \phi) \sin(\theta) d\theta d\phi \tag{1.3}$$

Where P_{rad} and P_{loss} are integral radiated and absorbed power, θ and ϕ are spherical angles and $p(\theta, \phi)$ is the radiated power density in a given direction. These two characteristics define a nanoantenna's overall efficiency and its ability to focus radiated power into a given angle.

A common use for optical nanoantennas is fluorescence enhancement of quantum emitters. A quantum emitter in an excited state can spontaneously decay back to its ground state (see Fig. 1.1A for and energy diagram showing the process) the rate at which this happens, the spontaneous decay rate, is, according Fermi's golden rule proportional to the local density of states (LDOS) [2]. In the presence of a nanoantenna, the LDOS is modified, and, in turn, affects the decay rate of the quantum emitter. Thus, nanoantennas can be used to "engineer" the LDOS and increase quantum emitter decay rate.

A figure of merit for fluorescence enhancement is the antenna's Purcell factor, the increase of spontaneous emission of a single quantum emitter in the presence of an antenna relative to spontaneous emission of the emitter in free space, represented as [2, 34, 35, 36]

$$F_p = \frac{3}{4\pi^2} \left(\frac{\lambda}{n}\right)^3 \frac{Q}{V} \tag{1.4}$$

where $\frac{\lambda}{n}$ is the resonant wavelength, Q is the quality factor of the mode excited in the antenna and V is the mode volume of the antenna. A mode's Q factor inversely proportional to the rate the modes loses energy, either through radiation or through non-radiative dissipation. V, the mode volume, represents the spatial confinement of the electromagnetic field of the mode. The Q/V ratio is proportional to the

LDOS, and thus a large part of nanoantenna design is trying to optimize Q/V [33, 37, 38, 39].

This can also be written in terms of decay rates [2]:

$$F_p = \frac{\gamma}{\gamma^0} \tag{1.5}$$

Where γ is the decay rate of the quantum emitter in the presence of the antenna and γ^0 is the decay rate of the emitter in free space. Decay rates of quantum emitters can be directly measured by time-resolved fluorescence microscopy [40], allowing one to directly measure an antenna's Purcell factor. Since quantum emitters are not perfect, an absorbed photon by an emitter will not always result in the emission of another photon (called radiative decay), sometimes the emitter will relax into its ground state through nonradiative means (hence, called nonradiative decay). A measure of a quantum emitter's quality is the ratio of emitted photons to absorbed photons, called quantum efficiency (QE) or quantum yield (QY):

$$\mathrm{QY} = \frac{\gamma_{\mathrm{rad}}}{\gamma_{\mathrm{rad}} + \gamma_{\mathrm{nonrad}}} \tag{1.6}$$

The presence of an antenna can modify both radiative and nonradiative decay rates of an emitter.

The Purcell factor is only part of the story when discussing fluorescence enhancement by a nanoantenna — efficiently exciting the emitter and efficiently collecting the resulting photons are two other important elements. The total fluorescence enhancement provided by a nanoantenna coupled to quantum emitters, compared to the quantum emitters in free space (denoted by the superscript "0"), can be described by the following equation [14, 10, 41]:

$$\mathrm{EF} = \frac{\gamma_{\mathrm{exc}}}{\gamma^0_{\mathrm{exc}}} \frac{\mathrm{D}_{\mathrm{em}}}{\mathrm{D}^0_{\mathrm{em}}} \frac{\mathrm{QY}}{\mathrm{QY}^0} \tag{1.7}$$

The first ratio represents the excitation enhancement of the quantum emitters, and is proportional to the change in quantum emitter excitation efficiency in the

presence of the nanoantenna. The second ratio represents the collection efficiency enhancement, which corresponds to enhancement of the collected signal into a given numerical aperture (NA). The last ratio represents the enhancement of the emitter quantum yield (QY).

This total enhancement factor is directly measurable by comparing the fluorescence intensity of free standing emitters to emitters coupled to the nanoantenna.

Nanoantennas can be classified into three main categories by the type of material they are made from: plasmonic, dielectric and hybrid.

1.2.1 Plasmonic Nanoantennas

Plasmonic nanoantennas, which are an extension of traditional radio-frequency antennas into infrared and optical wavelengths [42], were historically the first to be developed. At optical frequencies, electromagnetic radiation is capable of penetrating into the the surface of a metal an exciting oscillations in the free-electron gas. Typically, gold or silver are used as materials for plasmonic nanoantennas because of their low absorption and good metallic properties [43], though many other materials can also be used[44, 45].

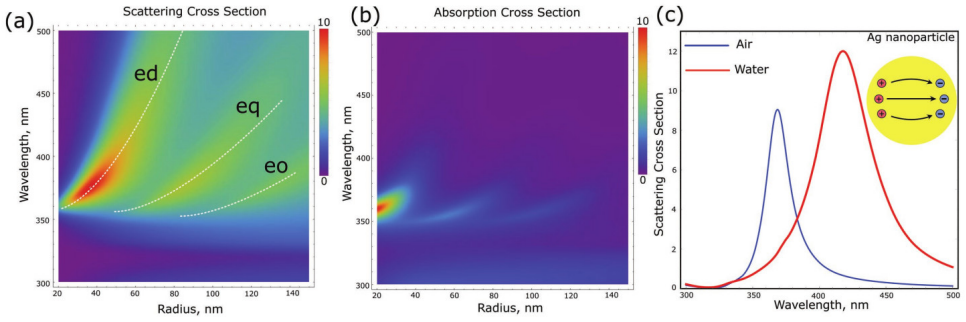

FIGURE 1.3: Optical properties of metallic (Ag) nanoparticles. **a** Normalized total scattering cross section (Q_{sct}) of the Ag nanoparticle. **b** Normalized absorption cross section (Q_{abs}) of the Ag nanoparticle. **c** Normalized scattering spectra of the Ag nanoparticle of radius 30nm Insets: schematic diagrams representing the fundamental modes of the metallic nanoparticle (electric dipole, plasmonic mode) Figure reproduced with permission from Ref. [18]

These collective oscillations of free electrons or plasmonic resonances, have been used to interact with light at the nanoscale [16, 27, 33, 18]. They have shown great utility in light manipulation due to their ability to concentrate electromagnetic

energy in extremely small regions, achieving great levels of field enhancement in these, so-called, "hot spots" [24, 25]. They exhibit easily tunable behavior, by changing their shape and size, of their electric resonances (see Fig. 1.3 and Fig. 1.4) and are able to provide field enhancement coefficients in the order of hundreds [24, 46]. Because of such high field confinement, plasmonic nanoantennas with Purcell factors in excess of 1000 have been demonstrated [10, 47, 12, 48].

This has led to their use in ultrafast emission in the picosecond range [10, 11, 12], strong coupling [49, 50] surface-enhanced Raman scattering (SERS) [51, 19, 17], optical interconnections [52, 53] and control of emission patterns [13, 14, 15], finding applications in near-field microscopy [54, 55, 56], biosensors [57, 58], photovoltaics [59, 60], and photodetection [61].

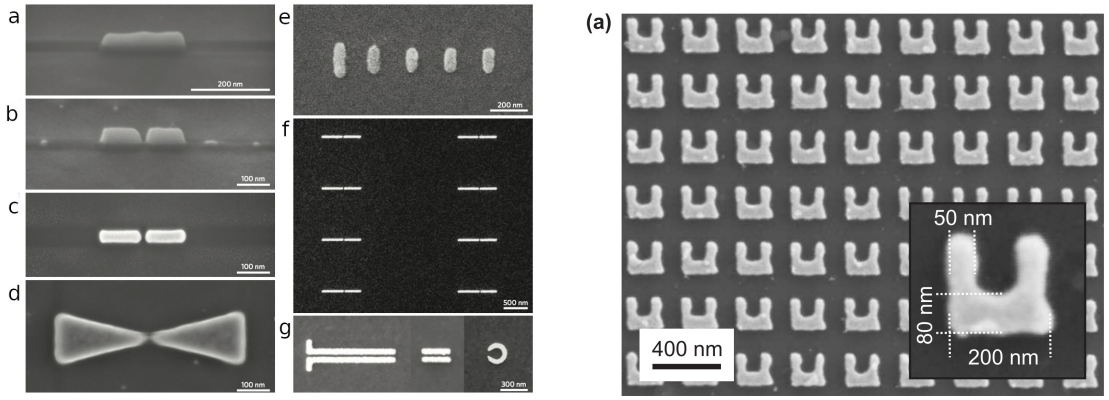

(A) (B)

FIGURE 1.4: Examples of plasmonic nanoantenna structures **A.** Various nanoantennas with gap sizes down to 10 nm, fabricated by focused ion beam milling. e–g, Yagi–Uda antenna (e), gap nanoantennas (f) and plasmonic waveguide and split-ring resonator (g), fabricated by electron-beam lithography and subsequent lift-off. Figure reproduced with permission from [16]. **B.** Split-Ring Resonator. Figure reproduced with permission from [62]

With the large local field enhancement being their main advantage, the flip side of plasmonic nanoantennas is their inherent high losses, related to the finite conductivities of the metals at optical wavelengths, leading to high absorption of light (see Fig. 1.3).This leads to plasmonic nanoantennas having relatively low efficiencies [18] and parasitic heating [63, 64], which can be a hindrance in certain applications [18]. This is especially important in fields related to biological sensing, where studied objects are very sensitive to temperature changes and can easily be destroyed[64].

Another limiting factor for plasmonic nanoantennas is the effect of quenching (see Fig. 1.5) — where the fluorescence of emitters is inhibited when brought too close to the nanoantenna because of the effect of non-radiative energy transfer [65]. This puts a lower limit on how close quantum emitters can be brought to the nanoantenna, yet because of the high field confinement achieved by the antenna, there is a upper limit on quantum emitter distance to the antenna without losing coupling efficiency. Thus, plasmonic nanoantenna design is often a balancing act between preventing quenching and maintaining coupling.

Another drawback of plasmonic nanoantennas is that they are limited to electrical modes, unless fabricated with complex shapes, for example split-ring as resonators (see Fig. 1.4)B [62].

This means that designing nanoantennas for specific directivity patterns usually requires large complex composite antennas, like micron scaled bulls-eye antennas [66, 67], multi-director Yagi-Uda antennas [13] or even large-scale metasurfaces [68, 69, 70]. Designing nanoscale, sub-wavelength, electrically small nanoantennas for directivity is a non-trivial task.

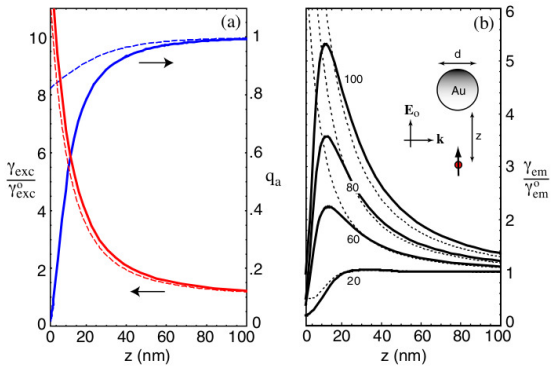

FIGURE 1.5: Calculated quantum yield q_a , excitation rate γ_{exc}, and fluorescence rate γ_{em} as a function of molecule-particle separation. γ_{exc} and γ_{em} are normalized with their corresponding free-space values ($z \to$ inf). The solid curves are the result of multiple multipole (MMP) calculations (max. error 2%) whereas the dashed curves correspond to the dipole approximation which fails for short distances z. In **a** the particle diameter is $d = 80$nm and in **b** it is indicated in the figure. Excitation wavelength is $\lambda = 650$nm and $\epsilon = -12.99 + i1.09$(gold). Figure reproduced with permission from [65]

1.2.2 Dielectric Nanoantennas

In dielectric nanoantennas, based on high refractive index materials (typically semiconductors, most commonly silicon), the interaction with light excites resonant polarization charges and displacement currents [18, 71, 72, 73].

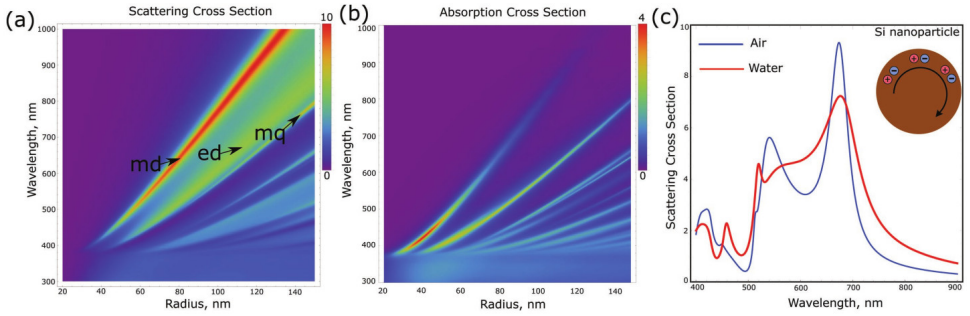

FIGURE 1.6: Optical properties of dielectric (Si) nanoparticles. **a** Normalized total scattering cross section (Q_{sct}) of the Si nanoparticle, depending on their radius (R) and wavelength. **b** Normalized absorption cross section (Q_{abs}) of the Si nanoparticle, depending on their radius and wavelength. Normalized scattering spectra of the Si nanoparticle (of radius 85nm) placed in air ($\epsilon_h = 1$, blue curves) and water ($\epsilon_h = 1.77$, red curves). Insets: schematic diagrams representing the fundamental modes of the dielectric nanoparticle (magnetic dipole, Mie mode). Figure reproduced with permission from Ref. [18]

These have inherently lower absorption losses, especially in the visible and infrared spectral ranges (see Fig. 1.6) and thus less heating than in their plasmonic counterparts [63, 18], though dielectric antennas designed specifically for localized, nanoscale heating have been reported [21, 20] (in contrast to [64], where dielectric antennas are used to minimize heating). This is one of the main advantages of this type of antenna. Another important advantage is the rich phenomenology of optical modes they can support. Even single dielectric nanoparticles of simple shapes support the excitation of both electric-like and magnetic-like modes [74, 71] (see Figure 1.6 and Figure 1.7 for modes supported by silicon nanospheres), whose mutual interference can lead to strong directionality [75, 76, 77, 78].

One more advantage of dielectric nanoantennas is that they, unlike plasmonic nanoantennas, can be manufactured using conventional, mature, nanofabrication processes, e.g. complementary metal-oxide–semiconductor (CMOS) processes for silicon nanoantennas antennas, while common plasmonic materials gold and silver are not CMOS-compatible materials [73, 72].

The main disadvantage of dielectric nanoantennas is that the achievable field enhancement and confinement is highly dependent on the contrast of refractive indices of the antenna and the surrounding medium, almost invariably resulting in lower enhancement factors than for plasmonic antennas [18], with the best nanoantennas demonstrating Purcell factors less than 50 [79]. The most commonly used material for dielectric nanoantennas, Silicon has a refractive index of $n \approx 3.5$ in the transparent near-IR region, another material, Gallium phosphide, with a transparent region extending further into the visible range, has a similar refractive index in the visible range. Germanium has a higher refractive index of $n \approx 4$ in its transparent region in the mid-IR. Other optically transparent materials like Silicon nitride or Gallium nitride have refractive indices of $n \lessapprox 2.5$ [80, 81, 82, 83].

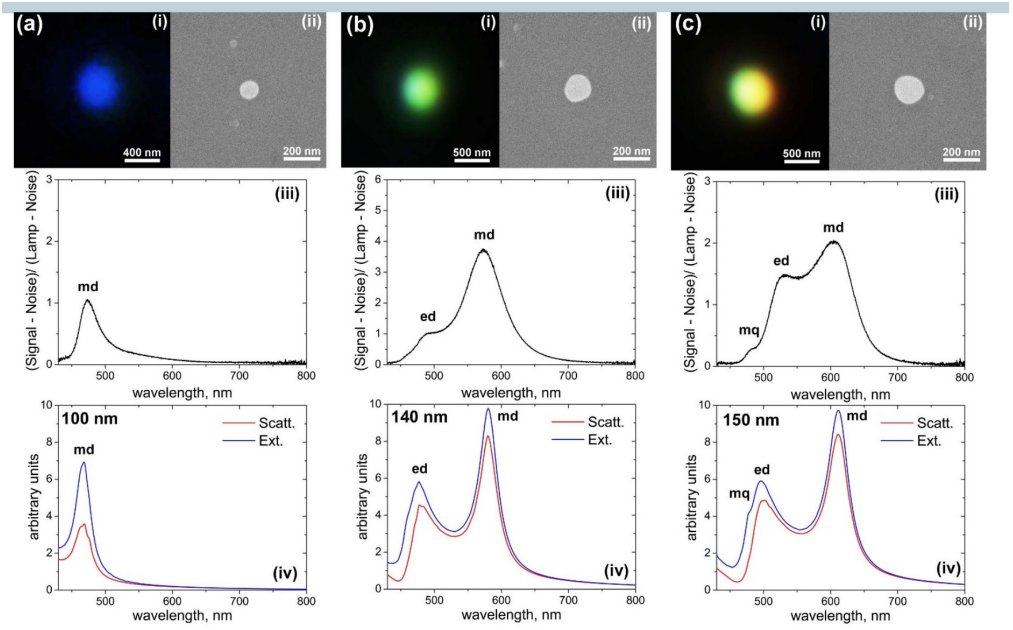

FIGURE 1.7: Close-view dark-field microscope (i) and SEM (ii) images of single nanoparticles. Figures 3 (a) to (c) correspond to nanoparticles of increasing diameter. (iii) Experimental dark-field scattering spectra of the nanoparticles. (iv) Theoretical scattering and extinction spectra calculated by Mie theory for spherical silicon nanoparticles of different sizes in free space. Corresponding nanoparticle sizes are defined from the SEM images (ii) and noted in each figure. Figure reproduced with permission from [74]

Figure 1.8 demonstrates the differences between plasmonic and dielectric nanoantennas: Fig. 1.8a and Fig. 1.8b show the interaction of a silicon dimer with a dipole, representing a localized source, in the two principal orientations, while Fig. 1.8c and Fig. 1.8d show the same dipole interacting with an equivalent gold dimer. We can see that the silicon dimer gets a significant response in both orientations of

the dipole, owing to the greater diversity of supported resonances, most notably the magnetic dipole resonance in each of the silicon particles, while the gold dimer only gets a significant response in one orientation. In that orientation, however, the gold dimer gets almost an order of magnitude stronger response than its silicon counterpart, for small gaps between the particles, owing to higher field enhancement and confinement. When the gap is increased, this difference decreases, and both nanoantennas can provide similar levels of enhancement.

Fig. 1.8e,f,g compare the thermal response of a silicon and gold dimer. It can be clearly seen that, because of the higher absorption of gold, the gold dimer exhibits massively larger heating, especially at higher energy densities of the exciting laser. This can be a limiting factor when working with biological objects that are sensitive to temperature changes[64].

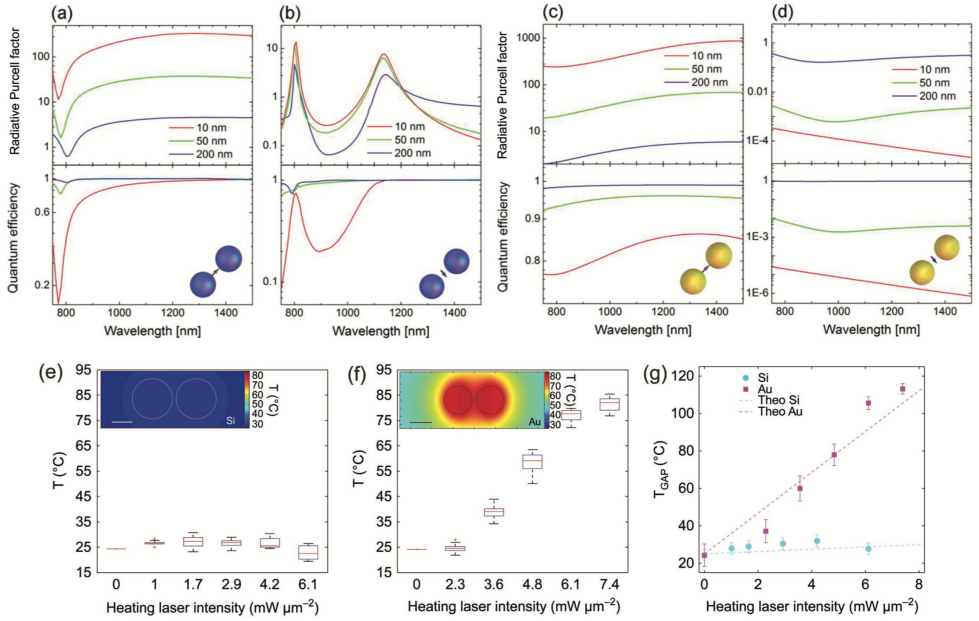

FIGURE 1.8: Comparison of the emission properties and temperature increase between Au and Si nanoantennas. Enhancement of the radiative decay rate and quantum efficiency of an electric dipolar emitter positioned in between two **a**,**b** Si and **c**,**d** Au nanospheres of 150nm radius. Orientations of emitters positioned at the centers of the systems are shown in the schematics. Gap widths are given in the legends. **e**–**g** Temperature measurements over Au and Si nanoantennas. Box plot shows the average temperature T, measured for **e** Si and **f** Au nanoantennas, excited at the resonance. The inset in each figure shows the calculated temperature map around the disks for the heating laser intensity of 5 mW μm^{-2} in both cases; scale bars are 100 nm. **g** Extracted temperature in the gap for selected silicon (cyan) and gold (magenta) nanoantennas as a function of the heating laser intensity at 860nm. The dashed lines show the numerical calculations for the temperature at the gap, presenting good agreement with the experimental data. Error bars show the standard deviation of the temperature measurements, obtained from error propagation from the fluorescence measurements. (**a**–**d**) reproduced with permission from [84]; (**e**–**g**) reproduced with permission from [64]

1.2.3 Hybrid Nanoantennas

These differing sets of advantages and drawbacks of the two different classes of nanoantennas have led to attempts at making hybrid plasmonic-dielectric nanoantennas that try to capitalize on the high field enhancement and confinement of plasmonic structures and low losses and greater flexibility of dielectric structures in a single operating device [85].

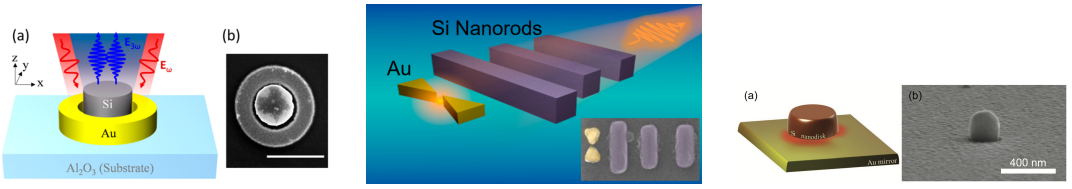

(A) (B) (C)

FIGURE 1.9: Examples of proposed and fabricated hybrid nanoantenna structures**A.** Silicon disk and gold ring antenna. Figure reproduced with permission from [86] **B.** Hybrid Yagi-Uda antenna. Figure reproduced with permission from [87] **C.** Dielectric particle on gold mirror antenna. Figure reproduced with permission from [88]

By combining plasmonic and dielectric elements in one structure one can get a wider array of different types of plasmonic and Mie-type resonances to manipulate light [85]. The interaction of these different type of resonances has been used to create nanoantennas for directional emission enhancement [89], switching and routing of light [90], unidirectional scattering [91] and higher harmonic generation [92].

Many of hybrid nanoantenna designs have been proposed [93] and fabricated, from simple dimer structures [86, 94, 95], to complex hybrid Yagi-Uda antennas [87] (see Fig. 1.9 for examples), but few works have demonstrated successful coupling of localized emitters to hybrid nanoantennas demonstrating directional enhancement. To the best of my knowledge, only in [96, 97], are localized quantum emitters coupled to micron-scaled hybrid bullseye nanoantennas [96, 97, 67, 66, 98, 99, 28] to demonstrate antenna directivity.

Hybrid nanoantennas often utilize a plasmonic structure to provide fluorescence enhancement and then couple the resulting emission to a dielectric structure for directivity tuning. A good example of this approach was shown in [87], where a gold bowtie nanoantenna provided fluorescence, which was then steered by a silicon Yagi-Uda antenna. The main appeal of this kind of approach is its simplicity —

known structures with known properties can be put together like Lego blocks to construct an antenna with desired properties.

An alternative approach would be to use the fundamental modes of plasmonic and dielectric nanostructures to create hybrid modes from the aggregate hybrid nanostructure that have the desired properties. An example of such an approach would be the theoretical exploration of different combinations of dielectric and plasmonic nanoparticles to create different directivity patterns done in [94].

1.2.4 Antenna Design

Up until the last couple of years, optical nanoantenna design processes have been been stuck using a few building blocks — spheres, cylinders, rings, bowties and SRRs, intuitive designs and parameter sweeps to create and optimize nanoantennas for specific purposes.

Radiofrequency antenna design has been using a huge variety of design algorithms for decades — from simple iterative algorithms to compensate for structural deformation [100], fractal antenna design [101, 102], iterative Fourier transform [103] to evolutionary algorithms [104].

The lagging of optical antenna design algorithms behind their radio-frequency counterparts can potentially be explained by the abundance of resonances supported by commonly used nanoantenna building blocks, meaning that for simple optical devices, there was no need for complex antenna designs and therefore, no need for complex optimization algorithms.

With the advent of optical metasurfaces and attempts at achieving complex beam deflection, beam forming, polarization conversions, etc [105], required performance of single nanoantenna components became more and more important. Paired with the development of the field of machine learning, a myriad of works using some form of machine learning algorithm either to directly solve the inverse problem of metasurface response or to solve the forward problem of arbitrary metasurface response coupled to some form of evolutionary optimization algorithm have been published [106, 107, 108, 109, 110, 111, 112, 113, 114].

Several works detailing novel design techniques for single nanoantennas have also been proposed — either machine learning algorithms solving for arbitrary plasmonic [115, 116, 117] or dielectric [117, 118, 119] geometries, or using a physics-first approach, tuning the local density of states of the antenna [120].

1.3 Quantum Emitter Manipulation

For efficient interaction between nanoantennas and localized light sources, one needs to bring the localized light source to the hot spot of the antenna. Such precise nanoscale manipulation of objects is a complicated task, with several different techniques developed.

Apart from randomly distributing emitters over the surface of the substrate and hoping to have emitters located close enough to the antenna to interact with it, quantum emitter localization techniques can be loosely grouped into three categories:

- Precisely determining the location of preexisting emitters and then fabricating the antenna at that location [121].
- Physically moving emitters to the desired location [122, 123]
- Fabricating emitters at the desired location [124, 125]

Choice of optimal technique is highly dependent on the requirements of the design — what is the operating environment, what are the planned emitters, etc.

1.3.1 Non-localized Emitters

Before getting into describing methods for quantum emitter localization, use of non-localized emitters to demonstrate the functioning of nanoantennas should be mentioned. This is the simplest way of characterizing nanoantenna functionality — taking a substrate with the target nanoantennas and covering the whole substrate uniformly with quantum emitters, often with a fluorescent dye [79, 126]. This simple method allows one to couple quantum emitters to nanoantennas without any complicated manipulation, but provides virtually no control over how many emitters are coupled to the antenna or how they are distributed at the nanoscale on the antenna. Figure 1.10 shows two examples of such an emitter distribution — a monolayer of quantum dots spin-coated onto a substrate or a monolayer CVD-grown WS_2 triangles transferred to a target gold-coated substrate.

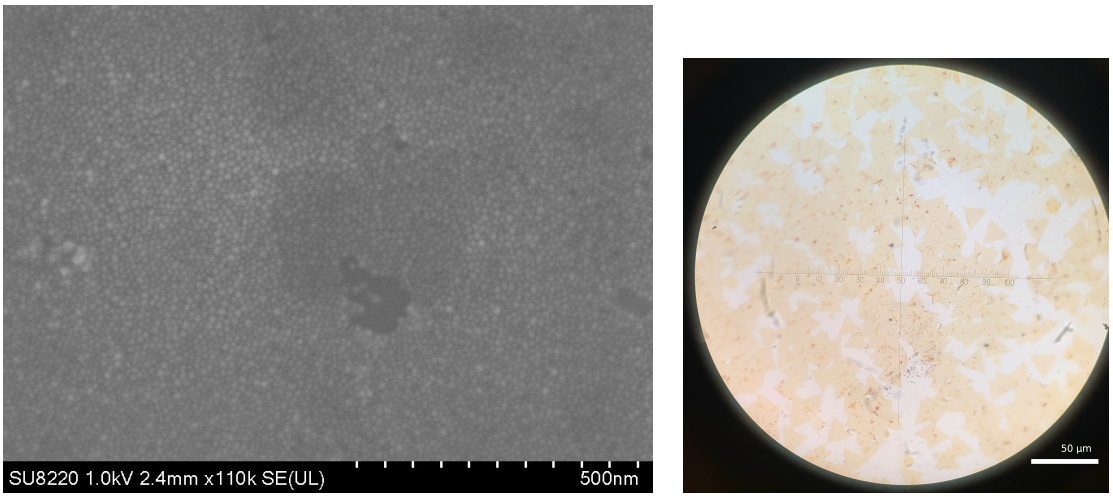

(A) (B)

FIGURE 1.10: **A.** SEM image of a monolayer of spin-coated colloidal quantum dots. **B.** Optical image of a monolayer WS_2 triangles after transfer.

A more recent development of this technique came with the active study of 2D materials with intrinsic fluorescence, where nanoantennas are deposited or fabricated on top of monolayer flakes of 2D materials like WS_2 or MoS_2 [127, 128, 129, 130, 131]. An interesting extension of this was shown in [132], where plasma etching after depositing nanoparticles on the MoS_2 flake was done, etching away the uncovered portion of the flake, effectively localizing the emitting material below the nanoparticle.

1.3.2 Preexisting emitter localization

If one has preexisting emitters on the target substrate, commonly these will be epitaxially grown quantum dots, measuring their position could allow further fabrication processes to align nanoantennas to the emitters. Many ways for doing this have been demonstrated [121].

The techniques usually go one of two routes. They can try to locate the emitters physically, by locating deformations in the surface of the samples caused by the presence of these quantum dots, as shown in Figure 1.11 [133]. This can be done using AFM, which is very precise and can easily detect single-nanometer sized bump on the surface created by the presence of QDs, but as with any scanning probe microscopy method, is very time consuming, or using SEM, which is a much faster imaging method, but will struggle to differentiate such small bumps in an otherwise

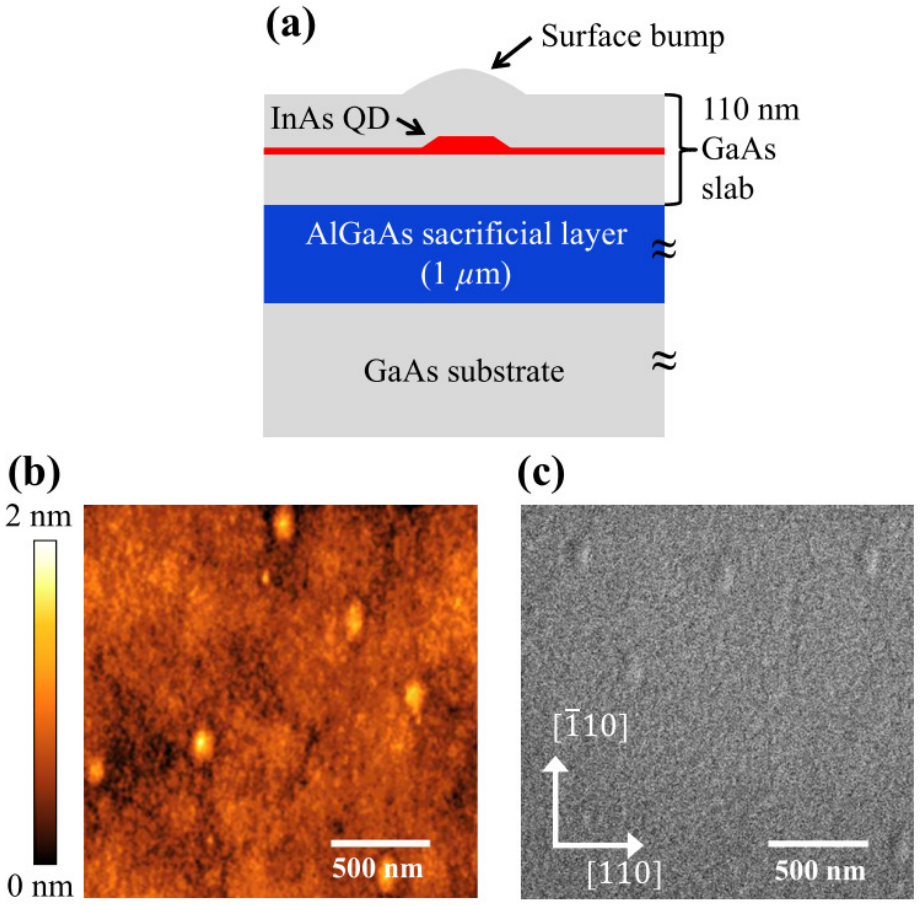

FIGURE 1.11: (a) Schematic of the QD wafer structure (not to scale). The wafer contains InAs QDs capped with a 55 nm-thick GaAs layer. (b) AFM image of the surface of the as-grown wafer. The typical height of the bumps is ¡2 nm. Capture time of the AFM image is 5 min. (c) SEM image of the same wafer as that in (b), obtained with an acceleration voltage of 1.0 kV. Surface bumps are originated from QDs underneath. Image capture time was a relatively long 80 s for a better signal to noise ratio.
Figure reproduced with permission from [133].

monolithic surface. A second approach would be to image the photoluminescence of the emitters and use that for positioning, as was done in [134] or [135], see Figure 1.12.

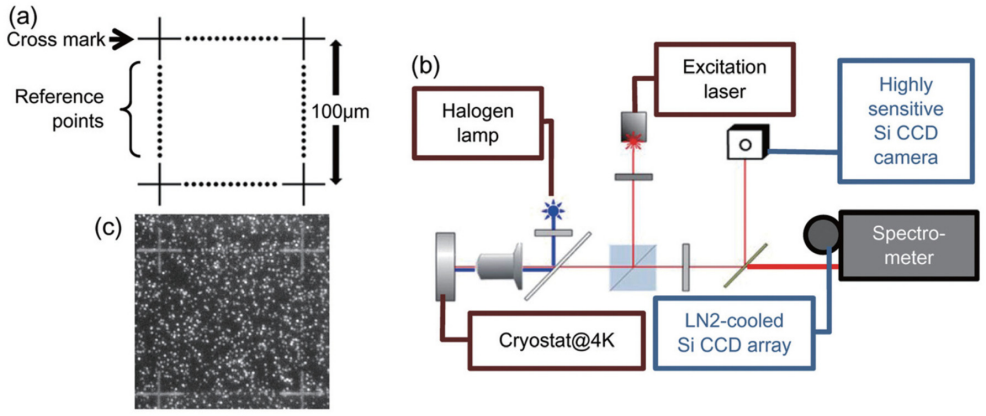

FIGURE 1.12: (a) Schematic view of cross- marks and reference points made on the GaAs wafer. The cross-marks have arms of length 31 mm, and the reference point diameter is 800 nm. (b) Schematic view of the l-PL setup used to detect the positions and wavelengths of QDs. An 830-nm continuous wave laser was used for excitation. (c) PL image of the QDs and positioning markers. The scale is the same as in (a).
Figure reproduced with permission from [134]

1.3.3 Physical Emitter Manipulation

Physically manipulating an emitter is also a relatively common technique, where micromanipulators or AFM probes are used to either push around or pick-and-place nanoparticles. Examples are shown on Figure. 1.13a and 1.13b [136, 137].

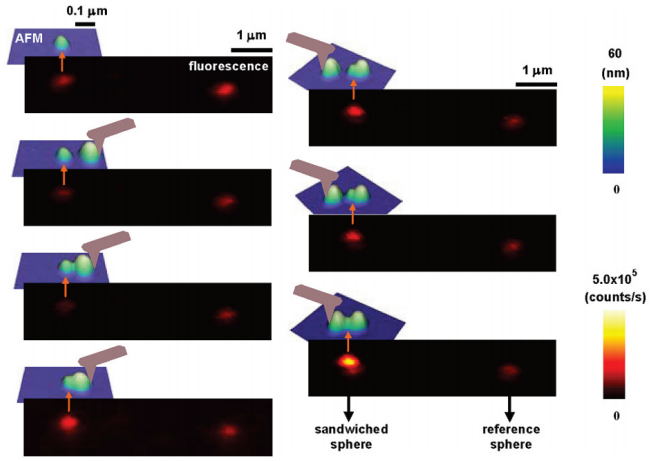

(A)

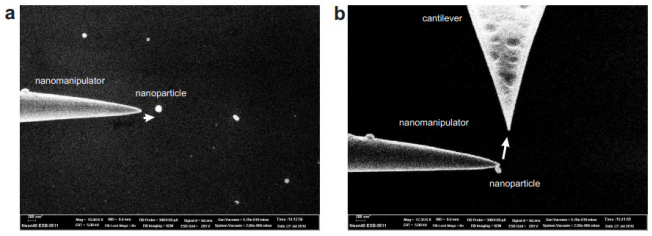

(B)

FIGURE 1.13: **A.** Series of manipulation steps. 3D AFM images of the sandwiched Fluorescent spheres (FS) are displayed above each fluorescence image. In the fluorescence images, the luminescent spot on the right belongs to the reference FS, and the luminescent spot on the left belongs to the approached and sandwiched FS. The left column in the figure shows in top-to-bottom sequence the approach of a first AuNP toward the FS from the right; the right column shows the same FS as a second AuNP is brought toward the FS from the left such that two AuNPs sandwich the FS. When the sandwich is fully formed (in the last manipulation step), the fluorescence of the FS is substantially enhanced as compared to the reference FS. Figure reproduced with permission from [136] **B.** (a) Tip of a nanomanipulator is placed near a nanoparticles. (b) Nanoparticle attached to the nanomanipulator is being placed to a Si cantilever, under SEM. Figure reproduced with permission from [137]

Using AFM probes to push particles around is usually done for relatively large particles, tens of nanometers in size, which mostly excludes emitters, as common quantum emitters like quantum dots and nanodiamonds are in the single nanometer

size range. Most often, relatively large nanoparticles are manipulated to come into contact with the smaller quantum emitters as was done in [138], [139] or [136] (see Figure 1.13a), although direct manipulation of quantum dots, coated in a polymer to increase their size, has also been demonstrated in [140].

Pick-and-place techniques are more common when trying to manipulate quantum emitters themselves. They usually consist of a AFM tip or a micromanipulator in a SEM that is put into contact with the object being manipulated, and hoping for either electrostatic or Van der Waals forces to get the particle to stick to the tip [141, 142, 122, 123]. Once the particle has been moved to the target location, the same procedure is repeated until the particle detaches from the manipulator and sticks to the target surface.

1.3.4 Deterministic Emitter Fabrication

Another method for localizing quantum emitters would be to deterministically fabricate them at the desired location. Several methods to do this have been proposed.

For epitaxially grown quantum dots, many ways of seeding nucleation have been demonstrated — from creating defects in the substrate to nanopatterning the substrate for selective epitaxial growth [143, 144, 145].

For colloidal quantum dots, a method for directly writing structures out of a spin-coated layer of quantum dots using either EUV light or e-Beam exposure has been recently demonstrated [125], fabricating quantum dot cylinders with sizes down to 65nm in diameter (see Figure 1.14).

A similar approach can be realized with Hydrogen silsesquioxane, HSQ, a common EBL resist. HSQ is known to form emitting silicon nanocrystals after thermal annealing [146] or e-beam exposure [147], with emission properties suitable for use with optical nanoantennas [148, 149].

Recent research into 2D materials, namely hexagonal boron nitride, hBN, has shown that hBN can support single photon emitting (SPE) defects [150, 151, 152, 151, 153, 154, 155, 156]. Emitting defects can be induced by thermal annealing, or

a variety of plasma treatments. These defects have also been successfully coupled to plasmonic nanoantennas [157].

More recently, it has been shown that SPE-supporting defects can be deterministically induced by focused ion beam (FIB) milling [124] (see Figure 1.15) or e-Beam irradiation [158].

Another method that could potentially be utilized to localize quantum emitters is based on photopolymerization. Photopolymerization is a group of techniques where high intensity light is used to cure a, usually, liquid precursor via a photochemical reaction [159]. The simplest techniques use UV light, but they struggle to achieve submicron cured volumes. 2-photon polymerization non-linear effect that uses NIR and has been shown to achieve cured volumes below 100nm in size [160, 161, 162, 163]. To achieve the non-linear regime required for 2-photon polymerization highly focused pulses are required. An alternative way of achieving the required intensity, or field concentration, is to utilize nanoantennas that can provide the required field concentrations, as was done in Ref. [164], and is shown on Figure. 1.16.

Because, in this case, the effect only occurs in the hot spot of the nanoantenna, in theory, if one were to embed quantum emitters into the precursor, the polymerization process would fix the emitters exactly in the hot spot of the antenna. The difficulties arising here are the compatibility of the emitters with the precursor used for 2-photon polymerization and the potential deterioration of the emitters under the high field concentrations required for the photochemical reaction.

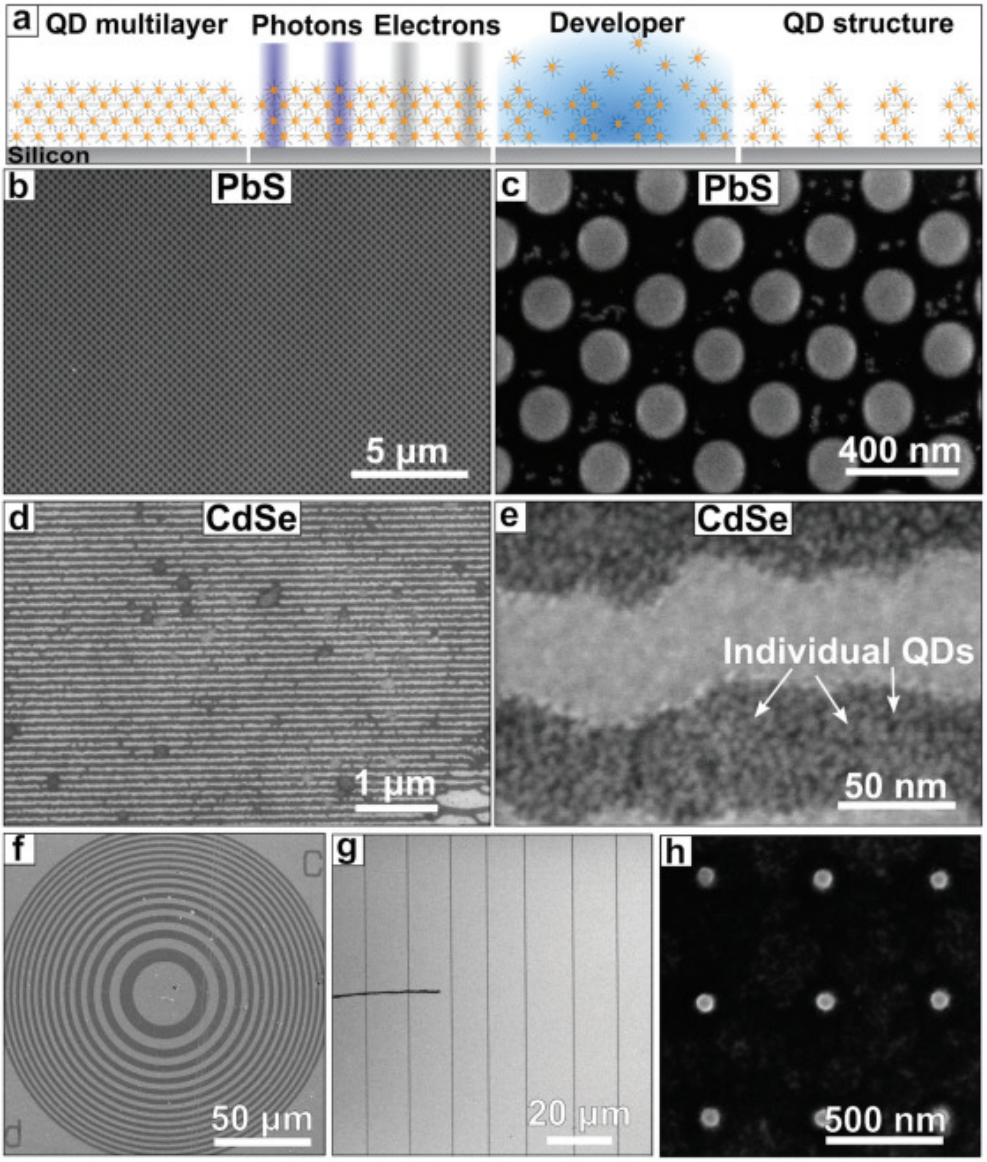

FIGURE 1.14: **a.** Direct quantum dot patterning with different irradiation sources. Colloidal quantum dots are spin coated onto silicon substrates to form thin films. After irradiation with photons or electrons with different energies, the particles cluster together through cross-linking of their organic shells. After submersion in an apolar developer, the irradiated structures remain on the substrates, while non-irradiated quantum dots dissolve. Images **b-h** are SEM images. **b.** Large field of patterned PbS pillars (180 nm diameter, 400 nm pitch) after EUV-exposure (140 mJ cm^{-2}) and development. Very few defects are present. **c.** Close up of patterned PbS pillars. **d.** Large-scale field of EUV-patterned CdSe lines. Exposure dose (55 mJ cm^{-2}). **e.** Close up of CdSe lines. The individual quantum dots can easily be identified. **f.** Larger, circular structure of CdSe QDs written with e-beam lithography (100 μC cm^{-2}). **g.**) Thin (≈100 nm) lines of CdSe written with e-beam (100 μC cm^{-2}). **h.** Pillars of CdSe quantum dots with a diameter around 65nm written with 100μC cm^{-2} e-beam dose.
Reproduced with permission from [125]

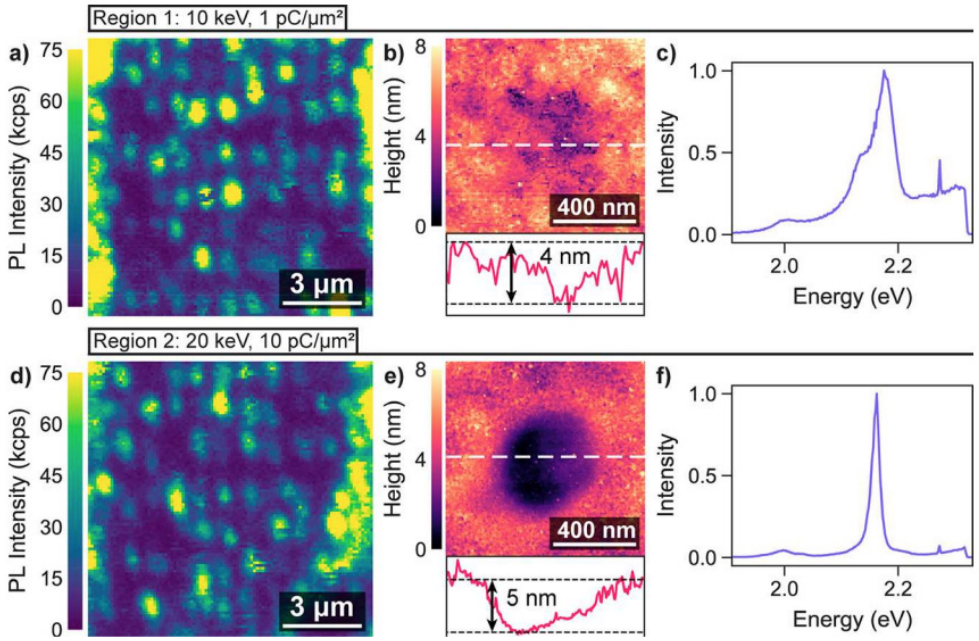

FIGURE 1.15: Confocal, AFM, and representative photoluminescence spectra for QEs made with various FIB parameters. Top row (Region 1): Low dose, low energy. Bottom row (Region 2): High dose, high energy. (a) Confocal scan showing high QE visibility. (b) AFM image showing rough, nonuniform milling. (c) Representative photoluminescence spectrum showing a single emission line with a broad background. (d) Confocal scan showing high QE visibility. (e) AFM scan showing uniform milling and smooth sidewalls. (f) Representative photoluminescence spectrum showing a QE spectrum with low background. Reproduced with permission from [124].

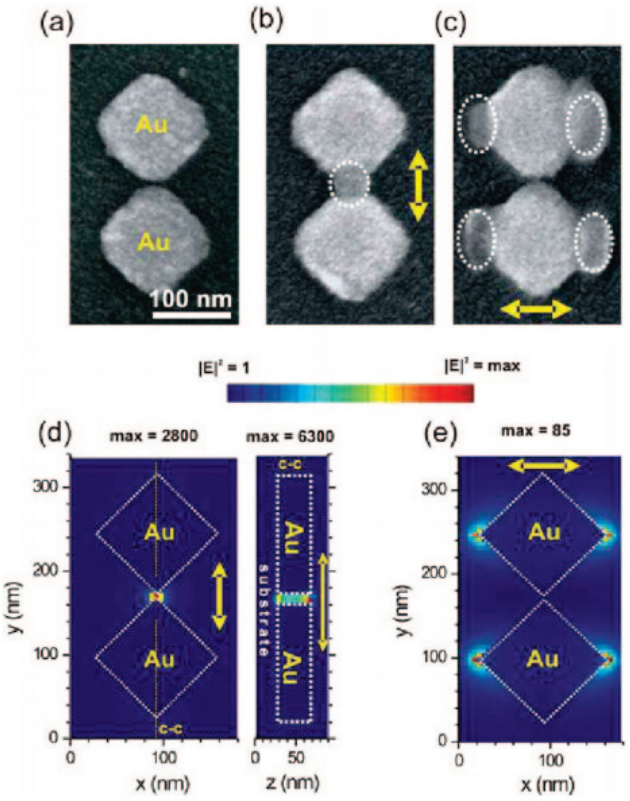

FIGURE 1.16: (a) SEM image of a pair of gold nanoblocks measuring 100 × 100 × 40 nm^3 and separated by a 5.6nm wide nanogap before irradiation by an attenuated femtosecond laser beam. (b) SEM image of other nanoblock pairs after 0.01s exposure to the laser beam polarized linearly along the long axis of the pair. (c) SEM image of another pair after 100s exposure to the laser beam polarized in the perpendicular direction. (d and e) Theoretically calculated near-field patterns at selected planes for the excitation conditions of the samples shown in (b) and (c), respectively. In (d), the field pattern is shown on the x-y plane bisecting the nanoblocks at half of their height (i.e., 20nm above the substrate), and in (e), the field is calculated on the plane coincident with the line c-c shown in (d). The field intensity is normalized to that of the incident wave and therefore represents the intensity enhancement factor. Figure reproduced with permission from [164]

1.4 Thesis Goals

Despite there being many published works on hybrid nanoantennas, actual experimental demonstrations of functioning nanoantennas coupled to quantum emitters are few and far between. This is probably related to the complexity of both fabricating hybrid nanoantennas and of localising quantum emitters, not to mention doing both at the same time. Also, there is virtually no published work on the design and optimization of hybrid nanoantenna structures, as most published work focuses on either dielectric or plasmonic structures.

The goal of this project is to do just that — design, fabricate and characterize a hybrid nanoantenna structure coupled to quantum emitters. This means designing and optimizing a hybrid nanoantenna structure; solving all potential fabrication issues that may arise and fabricating the designed structure; designing a protocol for localizing emitters in the nanoantenna hot spot and coupling the emitters to the fabricated antenna; and finally characterizing the nanoantenna, demonstrating out-of-plane directivity and fluorescence enhancement.

Thus, the thesis can be split into several main parts:

- Chapter 2, where I describe the development of antenna design and optimization techniques and algorithms, taking into account limitations of fabrication processes on the example of a Silicon Ring and Gold Dimer nanoantenna structure
- Chapter 3, where I describe development of quantum emitter localization protocols applicable to concrete antenna designs, e.g. the Ring and Dimer structure from Chapter 2 or a Particle-on-Mirror structure
- Chapter 4, where I combine the developed methods from Chapter 2 and Chapter 3 to produce a functioning nanoantenna coupled to quantum dots for high directional enhancement.

1.5 Major Contributions

The main contribution of my thesis is the experimental demonstration of a hybrid nanoantenna coupled to localized quantum emitters achieving over 650× directional enhancement and over 50× Purcell factor. This, to the best of my knowledge, is the first experimental demonstration of the dielectric particle-on-mirror nanoantenna concept demonstrating fluorescence enhancement and directivity tuning of localized quantum emitters.

Secondary contributions include:

- the development and demonstration of applicability of several techniques for the optimization of complex hybrid nanoantenna structures:
  - gradient descent optimization for systems with few degrees of freedom
  - genetic algorithm optimization for systems with many degrees of freedom
- the development of several techniques for the localization of quantum emitters:
  - printing of colloidal quantum dots using an AFM tip with a microfluidics channel,
  - namely direct writing of emitting defects in HSQ resist by EBL,
  - self-localization of quantum dots from a self-assembled layer via plasma etching
- the optimization of fabrication processes for the fabrication of complex hybrid nanoantennas structures based on electron beam lithography (EBL) with multiple mask alignment;
- the optimization of fabrication processes for the fabrication of hybrid particle-on-mirror nanoantennas structures with simultaneous quantum emitter localization using EBL without the need for mask alignment;

Chapter 2

Silicon Ring and Gold Dimer Nanoantenna

Most modern optical nanoantenna designs are based on a few building blocks, usually analytically solvable, or at least well-studied shapes, i.e. spheres, cylinders [2, 165, 166]. These building blocks are then put together into intuitively understood designs, that are then numerically simulated using methods like the Finite-Difference Time-Domain (FDTD) simulations [167, 168, 169], scanning over all the design parameters of the system, hoping to achieve the desired optimal result.

This works for simple systems, but adding more moving parts to the design makes such parametric sweeps overly time-consuming and difficult to implement.

An example of such a seemingly simple system would be a silicon ring and gold bowtie design. Gold bowtie nanoantennas have proven to provide high, sub-wavelength, localized field enhancement and have demonstrated very efficient localized fluorescence enhancement [16, 170, 171, 172]. Silicon rings, on the other hand, have been shown to have highly tunable radiation patterns with good out-of-plane directivity [173, 174, 175, 176]. Thus combining the two is intuitive to use the advantages of high field enhancement and high directivity.

Both structures on their own are relatively simple and well-studied, but the total system, a gold bowtie located inside a silicon ring has enough degrees of freedom in its design that makes it difficult to optimize with brute force parameter

sweeps. This is exacerbated by the fact that the simulations for this hybrid antenna structures involve nanoscale plasmonic elements, which generate highly localized electromagnetic fields, meaning that to ensure the accuracy of the FDTD simulations, very accurate grids are required, making the simulations very time and memory intensive.

Optimizing such a structure using a brute force parameter sweep would be very inefficient and take an extremely long time, so I needed to explore more sophisticated optimization techniques, which would decrease the number of required simulations to converge on the optimal solution.

Two different, highly developed optimization methods were used — an implementation of the steepest descent method[177, 178, 179, 180, 181, 182], and a genetic optimization algorithm[183, 184, 185, 186]. The steepest descent method allowed for very simple antenna designs to be quickly optimized, at the risk of getting stuck in local maxima, which is increasingly harder to detect for a large number of tunable parameters in the optimization. Therefore, the steepest descent method was limited to only 2 tunable parameters, providing enough flexibility to optimize the antenna geometry, but still simple enough to check for local maxima. Genetic optimization, a more stable method, was used for more complex optimizations, with more tunable parameters. Details on the optimization algorithms and numerical simulations are provided in Section 2.8.1.

As mentioned in Chapter 1 Section 1.2, nanoantennas' two main properties, radiation efficiency and directivity define their performance. Optimizing for maximum radiation efficiency will not necessarily produce optimal directivity, and vice versa. Therefore, a slightly more complex figure-of-merit was necessary for my optimization algorithms. In my simulations, I excited the nanoantennas structure by a single dipole and collected the radiated power, projected onto a sphere. Normalizing by the power radiated by a single dipole without the nanoantenna, I would get the radiative enhancement. By choosing which portion of the sphere I would integrate over, I could get directional enhancement into that solid angle. Therefore, for my optimization, the chosen figure-of-merit was directional enhancement into an out-of-plane solid angle approximating the collection angle of a 0.9 NA objective lens. Schematic showing this configuration is shown on Figure 2.1. This should provide both optimal enhancement and optimal directivity. More details on the enhancement simulations can be found in Section 2.8.1.1.

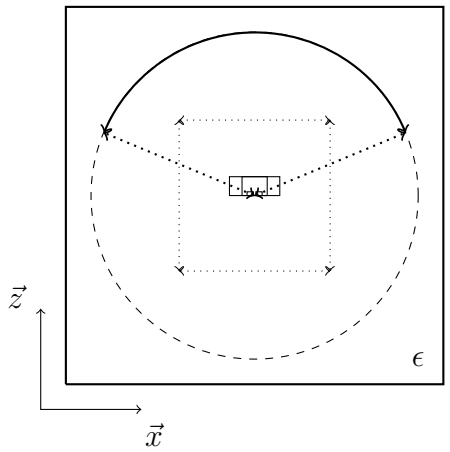

FIGURE 2.1: Schematic of nanoantenna simulation. Antenna is in the center of the schematic, surround by a dotted line representing box of field monitors, capturing near-field radiation. Dashed circle represents sphere onto wish the far-field radiation is projected. Thick line on the the circle shows the solid angle covering a 0.9 NA collection angle.

2.1 Ring and 4-arm Bowtie

2.1.1 Bowtie optimization

The initial design involved a 4-arm gold bowtie surrounded by a silicon ring. The reason to choose a 4-arm bowtie was to provide polarization-independent fluorescence enhancement, while the ring was to shape the directivity pattern of the whole antenna to provide out-of-plane directivity. Since the first goal was to demonstrate the viability of the design, the intrinsic photoluminescence of the gold bowtie [187] was used as the enhanced and shaped fluorescence. A similar approach has been demonstrated in [87], where the intrinsic photoluminescence of a gold bowtie was used to drive a hybrid Yagi-Uda antenna to demonstrate in-plane directivity.

Therefore, the first task to optimize the bowtie to have its main resonance at the wavelength of the intrinsic fluorescence of gold, which is around 650nm.

For the optimization, the three parameters that could be tuned were h, the height of the bowtie, g, the gap between the arms and r, the size parameter, which, for the isosceles triangles that make up the antenna corresponds to the base and height of triangles that form the arms of the antenna. Initial simulations were done assuming a surrounding medium with refractive index $n = 1$.

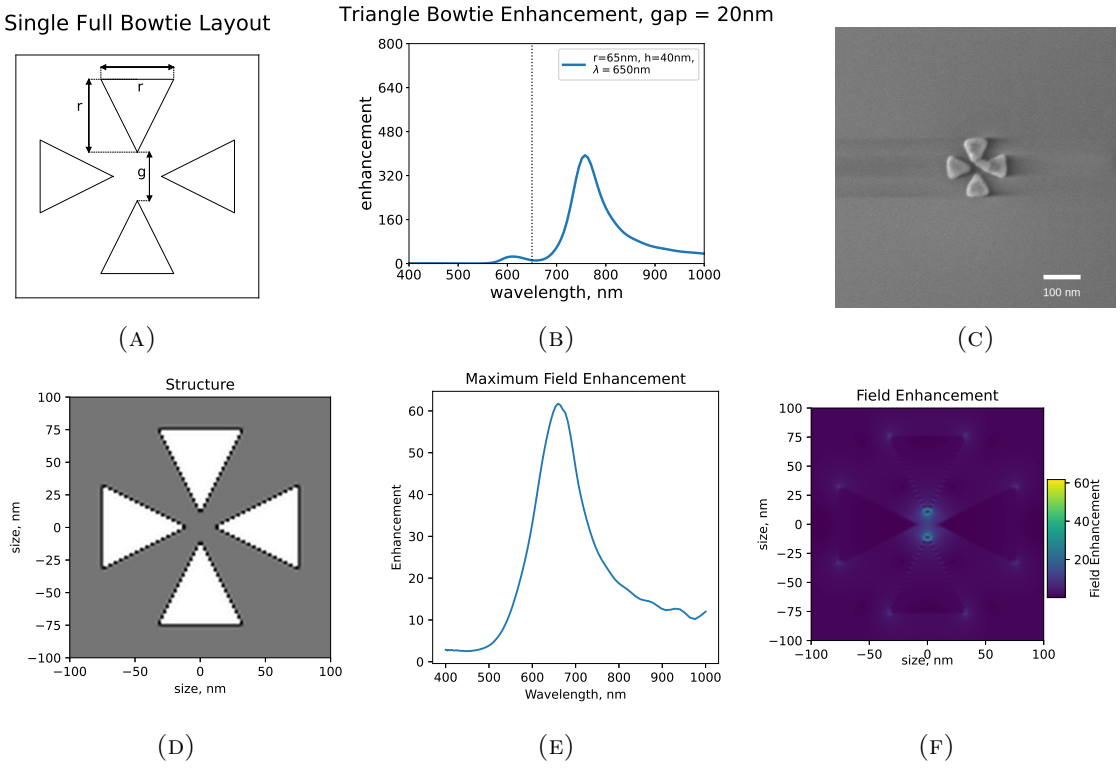

FIGURE 2.2: **a.**, Top view of the 4-arm bowtie antenna design, with r denoting the base and height of the isosceles triangles forming the antenna and g — the gap between the triangles, **b.**, 4-arm bowtie nanoantenna enhancement simulations; Optimization was done for emission at 650nm. **c.** SEM images of the fabricated gold triangle bowties. Scale bar is 100nm. Full fabricated bowtie with all 4 arms. Design specifications were size r = 65nm, gap g = 30nm and height h = 40nm **d.** Schematic of field enhancement simulation. **e.** Maximum field enhancement dependant on wavelength provided by the bowtie nanoantenna. **f.** Field enhancement map at resonant wavelength.

The choice of bowtie design was base on previous work from [87]. Bowtie structures have been widely studied, [188, 189, 190, 191, 192, 170, 193, 194, 195, 196, 189] showing that both the geometry of the triangles and the gap size affect the resonant response of the bowtie, but the triangle geometry predominantly affects the resonance position, while the gap size mainly determines strength of the response.

The schematic of the antenna is shown in Fig. 2.2a. Since the gap of the antenna mostly affects the level of enhancement that the bowtie provides, the two parameters chosen for the gradient descent optimization were height h and size r, while the gap was fixed at 20nm, a realistic gap that could be reliably fabricated. The permittivity model for the gold was chosen to fit the experimental data from Ref. [197]. In the far-field simulations, the bowtie was excited by a single point

dipole to simulate excitation by a single quantum emitter, and the intensity of the emitted field was used as the main figure of merit in the optimization.

Supporting simulations of the field enhancement provided by the bowtie nanoantenna are shown in Fig. 2.2e and f. The simulations were carried out by exciting the the bowtie structure with a normal-incidence plane wave, and measuring the field enhancement provided by the bowtie in the bowtie plane, at mid-height. These simulations show that the highest field enhancement provided by the bowtie is achieved at the same spectral position as the highest far-field emission enhancement, and that the highest field concentration is located in the bowtie gap.

Problems arose during the optimization process — shifting the main resonance to wavelengths shorter than 770nm was difficult within the constraint of designs that could be feasibly fabricated. Electron beam lithography (EBL), which was used for all the fabrication processes is generally limited to structures larger than 10nm in size, and reliably fabricating gaps below 20nm was an issue for the full hybrid structure, as will be shown in Section 2.1.3. Another constraint was that depositing gold layers thinner than about 20nm was not a stable process.

Only a higher order, secondary resonance could be moved to close to the target wavelength. The closest to optimal design ended up with a size $s = 65$nm, height $h = 40$nm and gap $g = 20$nm. The antenna's wavelength dependent enhancement is shown in Fig. 2.2b.

2.1.2 Ring Optimization

Despite having only a sub-optimal bowtie antenna, it was decided to try and optimize the silicon ring to facilitate out-of-plane emission. Using the same gradient descent method, the ring was described by 3 parameters: inner radius, $r_i = 100$nm, outer radius r_o and height h, with the latter two used for optimization (see Fig. 2.3a). The bowtie from the previous step was included into the simulation, so that any interaction between the bowtie and the ring would be accounted for. Simulations of the field enhancement provided by the ring and bowtie nanoantenna are shown in Fig. 2.3e and f, showing that at the main resonance of the bowtie antenna, there is very little field enhancement related to the ring structure, and the field enhancement in the gap of the bowtie nanoantenna is virtually unchanged.

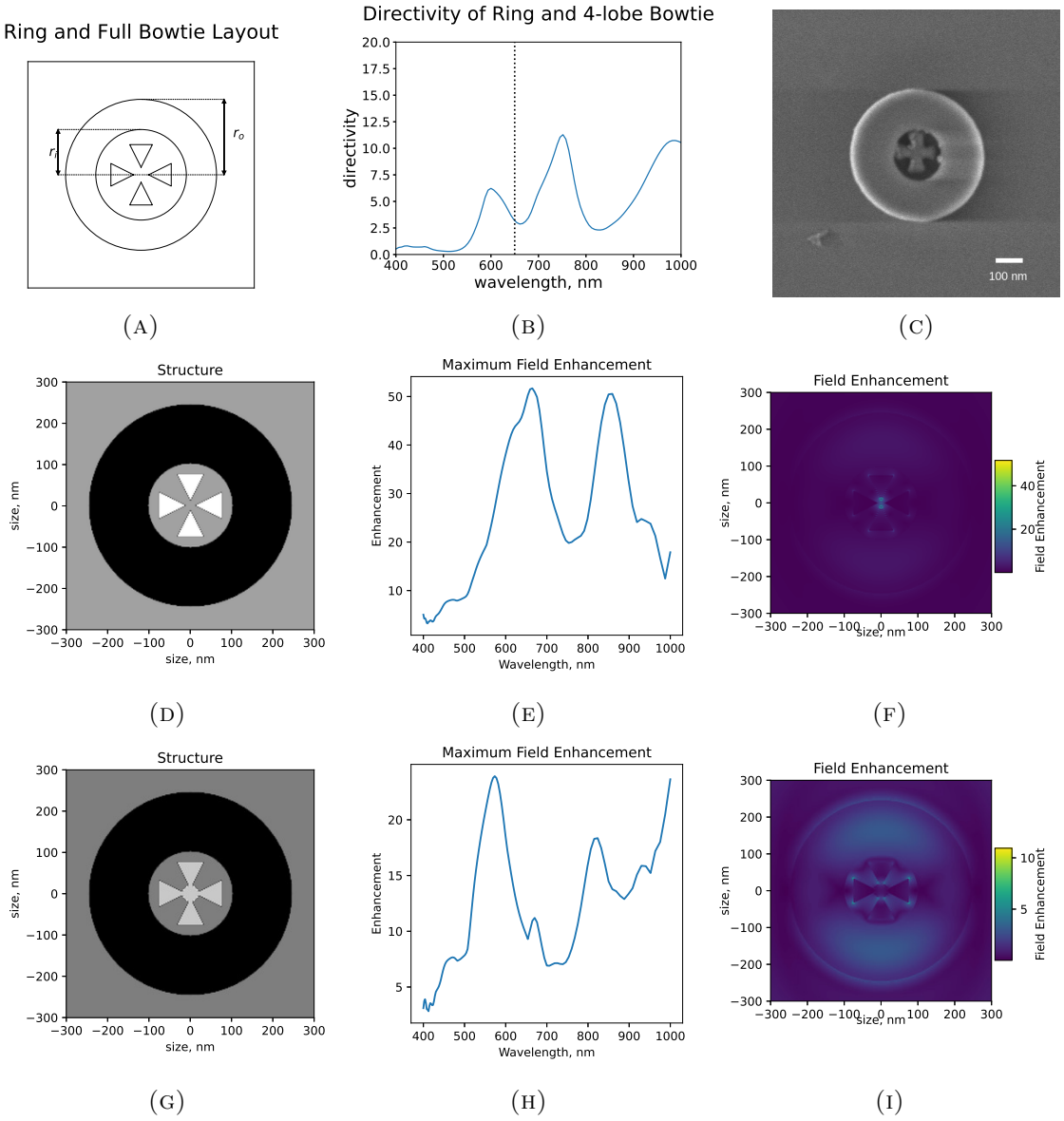

FIGURE 2.3: **a.** Top view of the design for the ring and 4-arm bowtie. r_i and r_o denote the inner and outer radii of the silicon ring. Bowtie parameters are taken from Fig. 2.2 **b.** Simulated directivity of ring and bowtie antenna embedded in medium with $n = 1.46$, **c.** Fabricated bowtie with all 4 arms surrounded by a ring. Presence of the ring caused the bowtie to be over-exposed and merge into a connected cross., **d.** Schematic of ring and 4-arm bowtie field enhancement simulation. **e.** Maximum field enhancement dependant on wavelength provided by the ring and 4-arm bowtie nanoantenna. **f.** Field enhancement map at resonant wavelength of 4-arm bowtie. **g.** Schematic of ring and connected 4-arm bowtie field enhancement simulation. **h.** Maximum field enhancement dependant on wavelength provided by the ring and connected 4-arm bowtie nanoantenna. **i.** Field enhancement map at resonant wavelength of connected 4-arm bowtie.

This resulted in an antenna that, predictably, didn't operate optimally at the desired wavelength of $\lambda = 650$nm, as can be seen in Fig. 2.3b. The directivity

pattern of the whole structure, though, was close to what I was aiming for, as shown in Fig. 2.4. Since this was deemed to be the optimal result that could be achieved with the current bowtie antenna, it was decided to fabricate the design to test the fabrication pipeline.

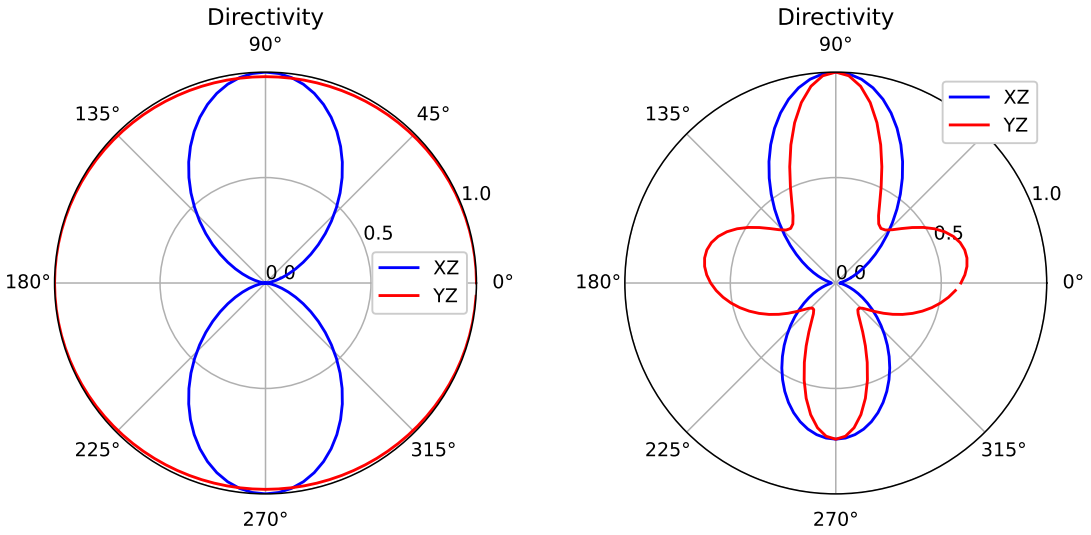

(A) (B)

FIGURE 2.4: **a.** Simulated directivity of 4-arm bowtie. **b.** Simulated directivity of ring and 4-arm bowtie.

2.1.3 Ring and bowtie fabrication

Fabrication of all the structures was done using electron beam lithography (EBL) for mask writing. Silicon structures were fabricated using chemical vapour deposition (CVD) of amorphous silicon, followed by reactive ion etching (RIE) to produce the final structure. Gold structures were fabricated by electron-beam physical vapour deposition of gold and mask lift-off to produce the final structure. Since the Ring and Bowtie structure need to be aligned with each other, alignment markers were first fabricated on the sample to align both the ring and bowtie structures. A detailed description of all the fabrication methods is given in Section 2.8.2.

Fabricating the stand-alone 4-arm bowtie antenna (see Fig. 2.2c) and, separately, the silicon rings was not much of an issue. Unfortunately, attempts to combine the two structures consistently resulted in the bowtie being overexposed — turning into a cross structure, as shown in the SEM image in Fig. 2.3c.

The most likely explanation is that since the bowtie fabrication process was carried out after the silicon ring was fabricated, meaning that the bowties were fabricated inside existing rings, proximity effects of the existing silicon ring were causing the resist to be overexposed [198, 199]. A simple mechanism could be constrained charge draining in the ring region because of the complex topography, or uneven distribution of the charge draining E-Spacer layer could have ended up unevenly spread over the ring structures, decreasing charge draining efficiency. More complex effects including electron scattering on the ring could also be affecting the fabrication process.

Such a connected cross structure no longer functions as the original bowtie — the original bowtie resonance is strongly quenched and a new resonance appears at much longer wavelengths, as can be seen comparing Figure 2.3E and H and for the stand-alone plasmonic structure in Figure 2.5. This quenching of the resonance has been demonstrated experimentally in [170], where bowtie nanoantennas were shown to stop emitting once the gap between the lobes closed. Thus if I were to try and use the cross structure, I would need to redo the whole optimization process for a completely new structure with, potentially, much worse operating characteristics.

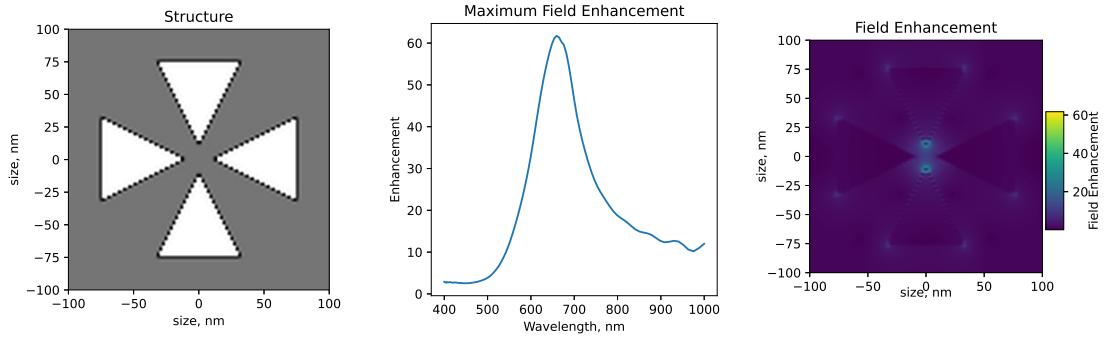

(A) (B) (C)

(D) (E) (F)

FIGURE 2.5: **d.** Schematic of 4-arm bowtie field enhancement simulation. **e.** Maximum field enhancement dependant on wavelength provided by the 4-arm bowtie nanoantenna. **f.** Field enhancement map at resonant wavelength of 4-arm bowtie. **g.** Schematic of connected 4-arm bowtie field enhancement simulation. **h.** Maximum field enhancement dependant on wavelength provided by the connected 4-arm bowtie nanoantenna. **i.** Field enhancement map at resonant wavelength of the 4-arm bowtie.

2.2 Ring and 2-arm Bowtie

To decrease the total required dose, I removed two of the arms of the bowtie(see Fig. 2.6a), and redid the whole optimization procedure. This still did not achieve the required resonance positions as can be seen in Fig. 2.6b. The radiation pattern of the antenna, remained virtually unchanged, as can be seen in Fig. 2.8. Supporting simulations of the field enhancement provided by the 2-arm bowtie nanoantenna are shown in Fig. 2.6e and f, also showing virtually unchanged field enhancement profiles.

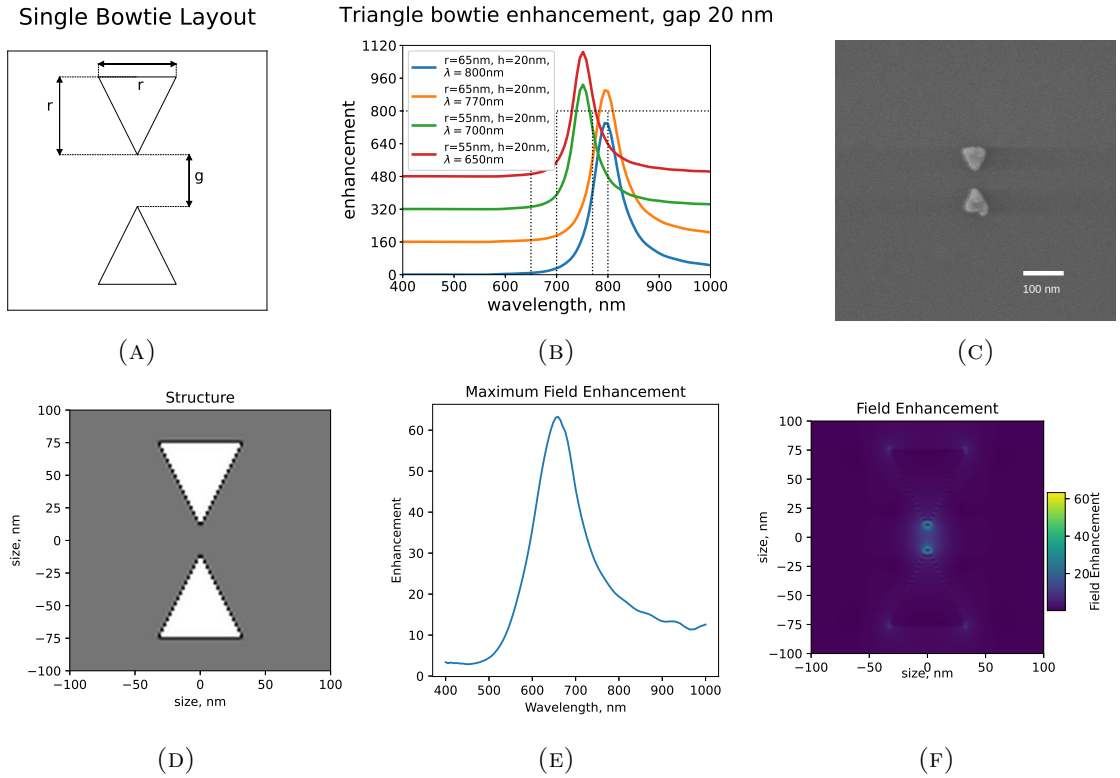

FIGURE 2.6: **a.** Top view of the 2-arm bowtie antenna design, with r denoting the base and height of the isosceles triangles forming the antenna and g — the gap between the triangles, **b.** 2-arm bowtie nanoantenna enhancement simulations; blue - optimized for 800nm, orange - optimized for 770nm, green - optimized for 700nm, red - optimized for 650nm. Size is the length of the base and height of the isosceles triangles the form the bowtie antenna. Gap between the triangles was fixed at 20nm. Plots shift on y axis for clarity. **c.** SEM images of the fabricated gold triangle bowties. Scale bar is 100nm. Fabricated bowtie with 2 arms. Design specifications were size $r = 65$nm, gap $g = 30$nm and height $h = 40$nm. **d.** Schematic of 2-arm bowtie field enhancement simulation. **e.** Maximum field enhancement dependant on wavelength provided by the 2-arm bowtie nanoantenna. **f.** Field enhancement map at resonant wavelength of 2-arm bowtie.

This allowed me to reduce the total required dose for the fabrication process enough to make fabricating the structure possible, Fig. 2.6c and Fig. 2.7c. However, the proximity effects of the ring were still strong enough to strongly distort the final bowtie (compare Fig. 2.6c and Fig. 2.7c), and made fabricating bowties with small gaps virtually impossible.

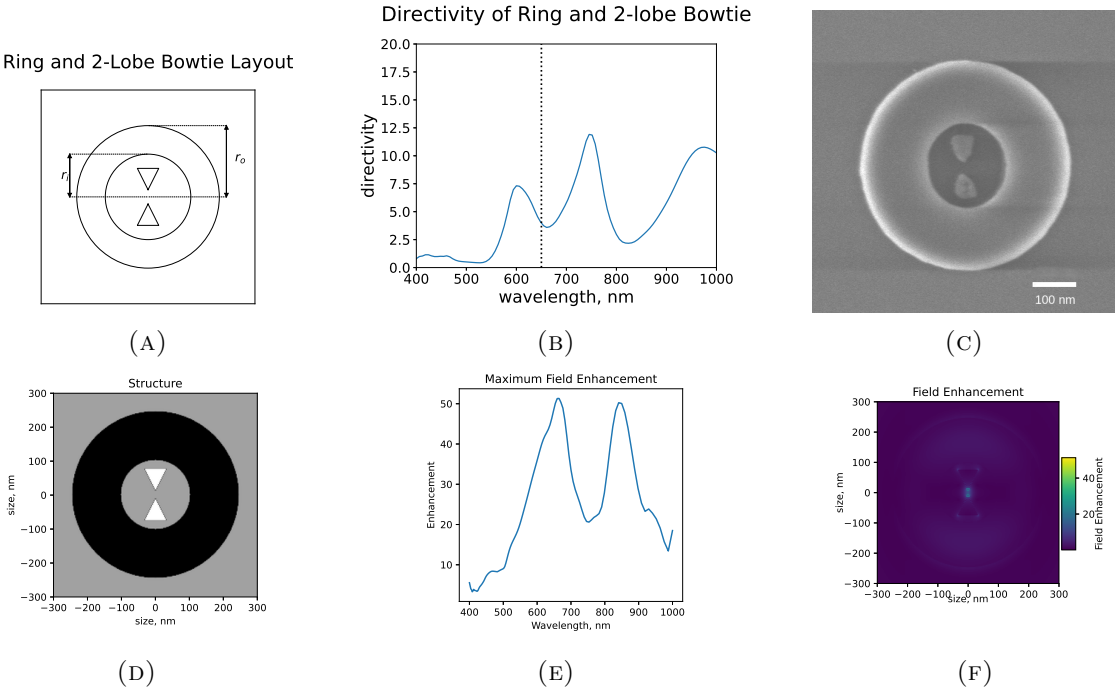

FIGURE 2.7: **a.**, Top view of the design for the ring and 2-arm bowtie. r_i and r_o denote the inner and outer radii of the silicon ring. Bowtie parameters are taken from Fig. 2.6 **b.** Simulated directivity of ring and bowtie antenna embedded in medium with $n = 1.46$, **c.** Fabricated bowtie with 2 arms surrounded by a ring. Design specifications of the ring were $r_i = 100$nm, $r_o = 245$nm and height $h = 130$nm. **d.** Schematic of ring and 2-arm bowtie field enhancement simulation. **e.** Maximum field enhancement dependant on wavelength provided by the ring and 2-arm bowtie nanoantenna. **f.** Field enhancement map at resonant wavelength of 2-arm bowtie.

Therefore I needed a structure with a simpler geometry, that would be more robust to the proximity effects during fabrication, and would have a resonance structure that wasn't as dependant on precise gap engineering.

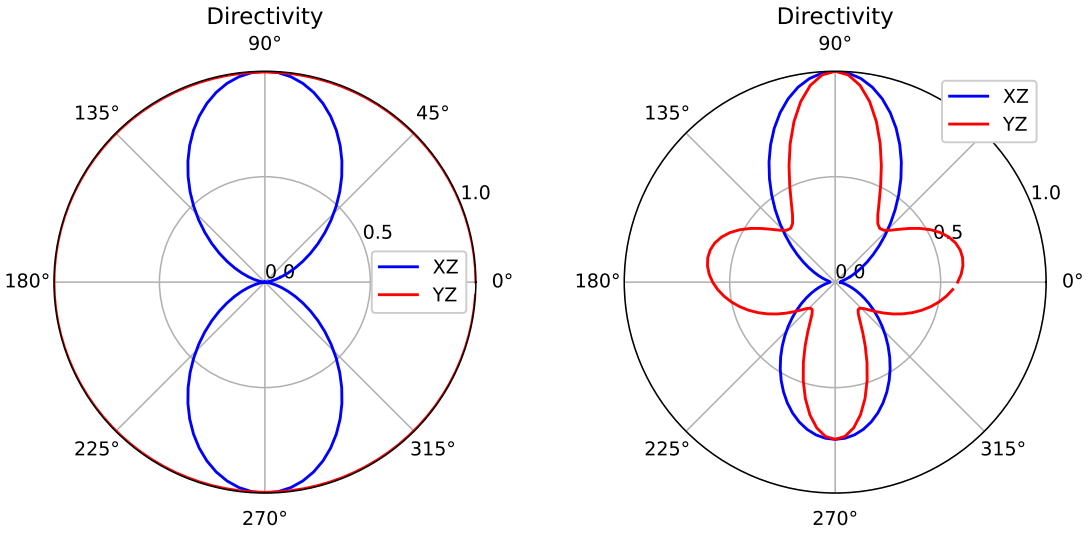

(A) (B)

FIGURE 2.8: **a.** Simulated directivity of 2-arm bowtie. **b.** Simulated directivity of ring and 2-arm bowtie.

2.3 2-arm Bowtie and Cylinder Dimer Comparison

At this point, it had been demonstrated that it was possible to fabricate the ring and bowtie structure, and that achieving an optimal antenna for intrinsic gold fluorescence was not feasible with the current design. One of the explanations for the failure to achieve an optimized triangle bowtie structure is the fact that I was limited in the number of optimization parameters and thus wasn't able to account for all the degrees of freedom present in the system. Such degrees of freedom could include the radius of curvature at the tip of the bowtie, the opening angle of the triangle and even the radius of curvature at the top of the triangles [192, 170, 193, 194, 195, 196, 189]. Adding these degrees of freedom to the optimization routine would exponentially increase to computational requirements. Another limiting factor would be the fabrication of such an optimized structure — I had already found that fabricating the bowtie inside the silicon ring leads to proximity effects that distort the resulting structure, making any fine-tuning of the simulated structure futile.

Therefore, a different design, with a simpler structure that would be easier to tune to the required wavelengths, and which would be more robust to fabrication inaccuracies was needed. A cylinder dimer structure was chosen for this purpose. The geometry of each cylinder can easily be defined by its' radius and height and, while providing lower absolute enhancement factors, can provide field enhancement in a larger volume, which will be advantageous for the future purpose of coupling the antenna to a quantum emitter.

Field enhancement maps and profiles of a bowtie and cylinder dimer nanoantenna with the same resonant wavelength are show on Figure 2.9.

Also, replacing the bowtie structure with the cylinder dimer, didn't strongly affect the radiation pattern of the whole structure, as shown in Fig. 2.10, further supporting the notion, that the ring structure mostly accounts for the directivity pattern, while the dimer is responsible for fluorescence enhancement.

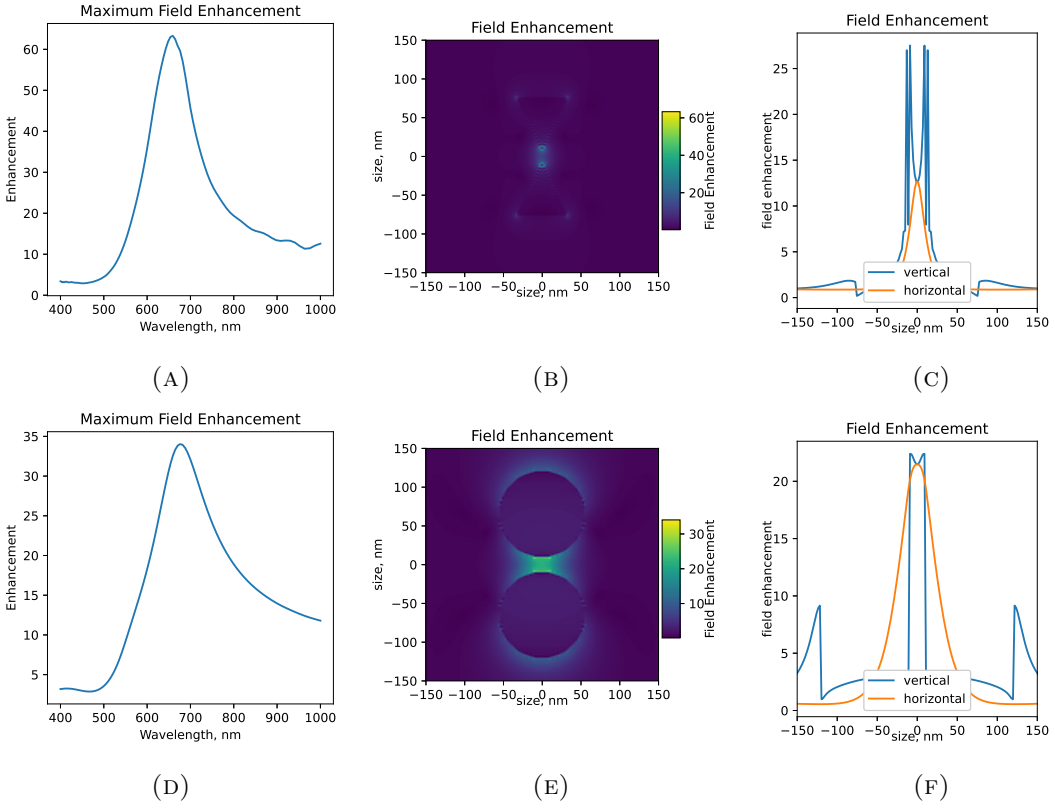

FIGURE 2.9: Comparison of field enhancement by bowtie and cylinder dimer nanoantennas with same gap size and similar resonance peak spectral position. **a.** Bowtie maximum field enhancement. $h = 20$ nm, $g = 20$ nm, $r = 65$ nm. **b.** Bowtie field enhancement map at resonant wavelength. **c.** Bowtie field enhancement slices. **d.** Cylinder dimer maximum field enhancement. $h = 20$ nm, $g = 20$ nm, $r = 55$ nm. **e.** Cylinder dimer field enhancement map at resonant wavelength. **f.** Cylinder dimer field enhancement slices.

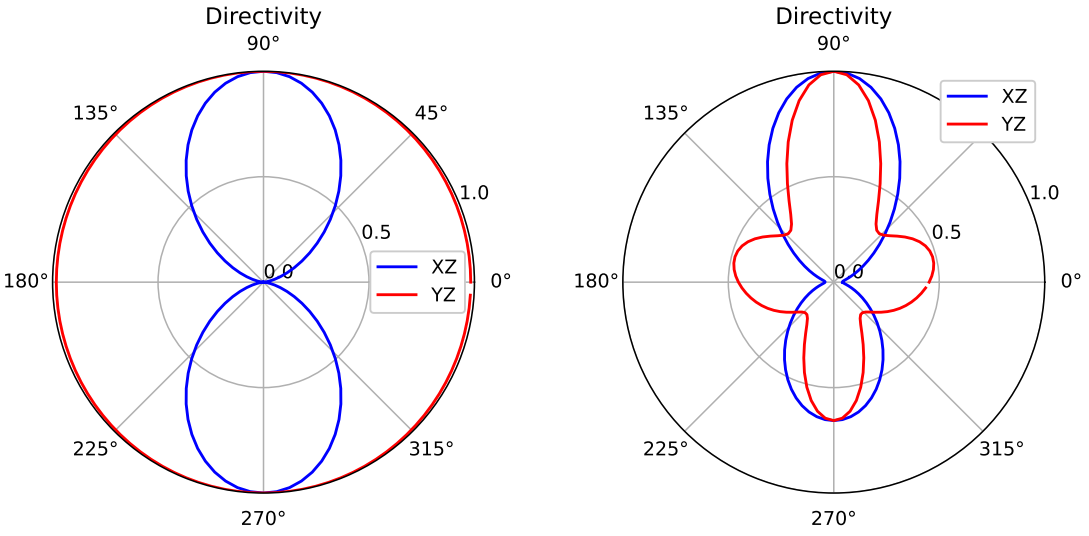

(A) (B)

FIGURE 2.10: **a.** Simulated directivity of cylinder dimer. **b.** Simulated directivity of ring and cylinder dimer.

2.4 Ring and Cylinder Dimer

This cylinder dimer structure, is shown in Fig. 2.11a, where r is the radius of the cylinders, g is the gap between the cylinders and h is the height of the dimer.

It was decided to optimize for an antenna embedded in a medium with a refractive index of $n = 1.46$, which is close to the refractive index of the substrates that would be used for the eventual fabrication of the antennas, and of potential polymers (most notably, poly(methyl methacrylate), PMMA) to be used to embed the fabricated antennas, so as to minimize substrate effects on the operation of the antenna.

The new structure was easy to tune to arbitrary wavelengths, as shown in Fig. 2.11, because the position of the resonance of the cylinder dimer was strongly dependent on the radii of cylinders.

This time, to be able to fully account for the interaction of the gold dimer with the silicon antenna, the whole antenna was optimized in a single run, using a genetic algorithm with 4 parameters: r_d, h_d, size and height of the dimer and r_o and h_r, the outer radius and height of the ring. The gap of the dimer was fixed at 20nm and the inner ring radius was fixed at 100nm. This gave me more freedom in designing the hybrid antenna, with the genetic algorithm producing several families of candidate designs.

The examples of the two main families of designs produced by the genetic algorithm are shown on Figure 2.12 — A narrow ring ($r_o = 140$nm, $r_i = 100$nm, $r_h = 150$nm) and a wide ring ($r_o = 340$nm, $r_i = 100$nm, $r_h = 280$nm).

The narrow ring structure provides 200× total fluorescence enhancement and over 300× directional, out-of-plane, fluorescence enhancement for at a wavelength of 630nm. The radiation pattern achieves slightly over 2× out-of-plane directivity.

The wide ring structure also provides 200× total fluorescence enhancement, but over 1000× directional, out-of-plane, fluorescence enhancement for at wavelengths of 700nm to 750nm. The radiation pattern achieves approximately 10× out-of-plane directivity.

These new designs were then fabricated and prepared for characterization, as seen on Figure 2.13.

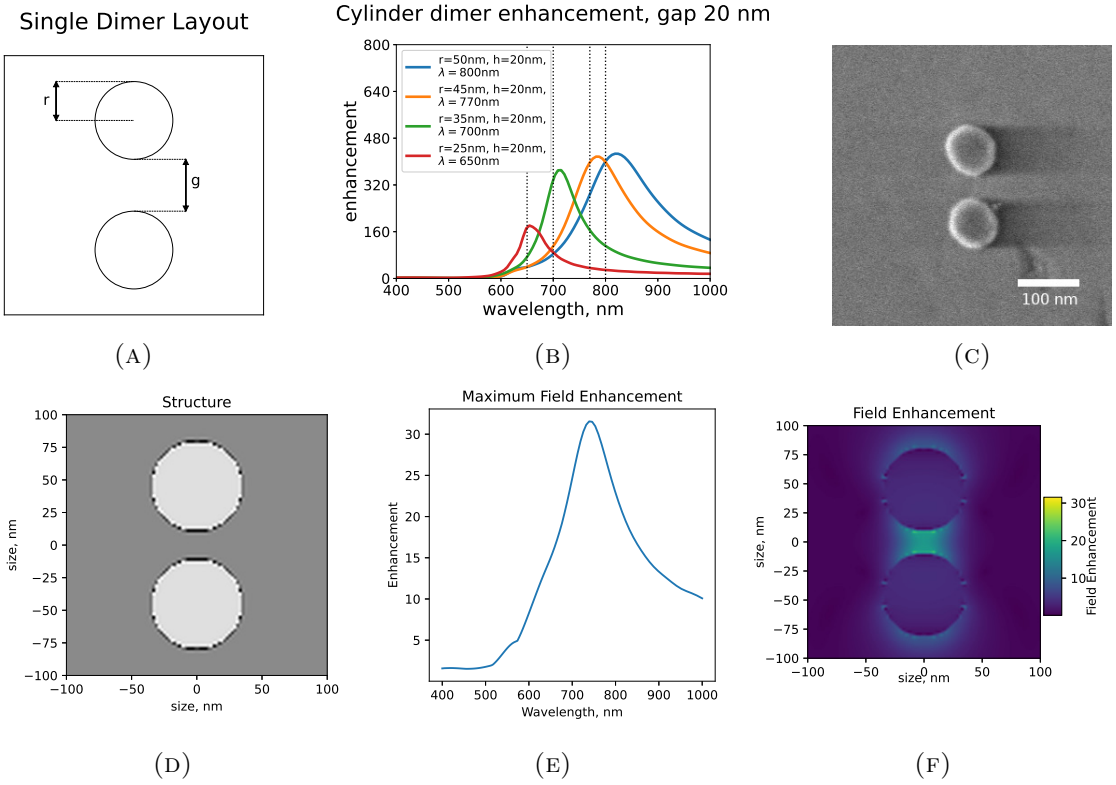

FIGURE 2.11: **a.** Top view for the the dimer antenna design, with r denoting the radius of both cylinders and g — the gap between the cylinders., **b.**, Cylinder dimer nanoantenna enhancement simulations; blue - optimized for 800nm, orange - optimized for 770nm, green - optimized for 700nm, red - optimized for 650nm. Size is the radius of the cylinders that form the dimer antenna. Gap between the cylinders was fixed at 20nm, **c.** SEM images of fabricated gold cylinder dimer. Design specifications were radius $r = 35$nm, gap $g = 40$nm and height $h = 20$nm.

d. Schematic of the cylinder dimer antenna field enhancement simulation. Antenna size used for the simulation was $r = 35$nm, $g = 20nm$ and $h = 20$nm. **e.** Maximum field enhancement dependant on wavelength provided by the dimer antenna. **f.** Field enhancement map at the resonant wavelength of the antenna.

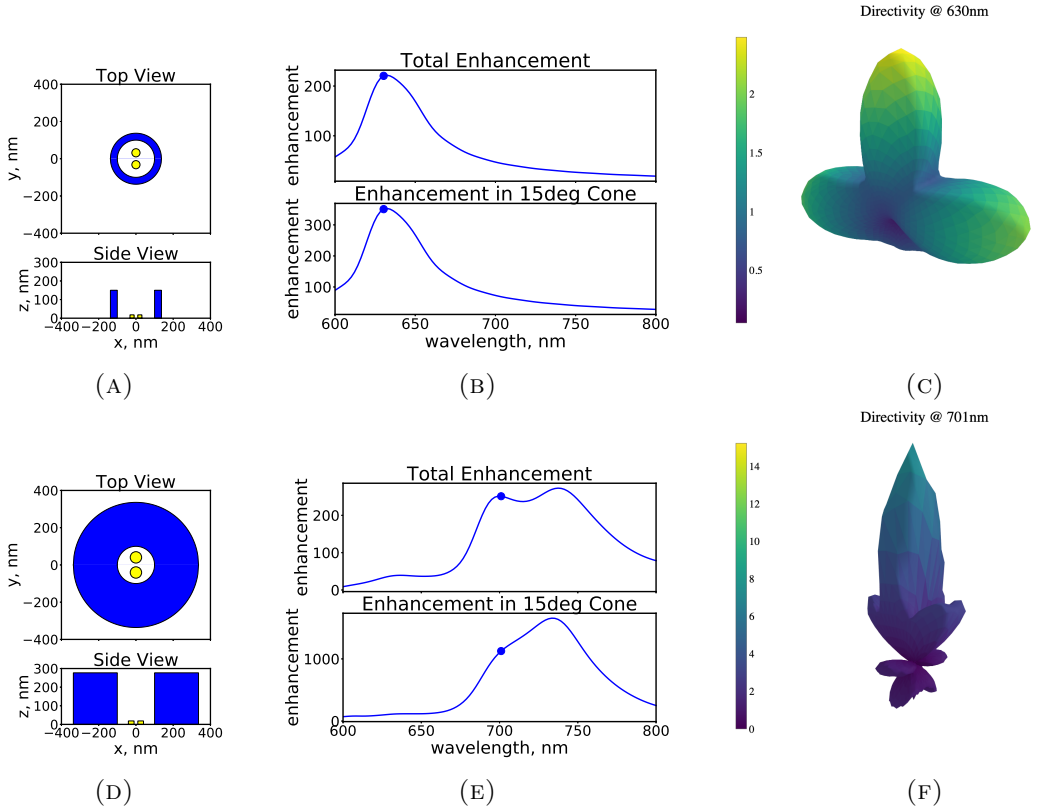

FIGURE 2.12: **A** Schematic of antenna optimized for directional enhancement at 630nm. Antenna parameters: Dimer radius $r = 22$nm, height $h = 18$nm, gap $g = 20$nm, Ring outer radius $r_o = 140$nm, inner radius $r_i = 100$nm, height $r_h = 150$nm. Antenna is embedded in $n = 1.46$ medium **B** Total fluorescence enhancement either integrated over a full sphere, or into a narrow cone perpendicular to the substrate plane. **C** Antenna Directivity at 630nm. **D** Schematic of antenna optimized for directional enhancement at 700nm. Antenna parameters: Dimer radius $r = 31$nm, height $h = 19$nm, gap $g = 20$nm, Ring outer radius $r_o = 340$nm, inner radius $r_i = 100$nm, height $r_h = 277$nm. Antenna is embedded in $n = 1.46$ medium **E** Total fluorescence enhancement either integrated a full sphere, or into a narrow cone perpendicular to the substrate plane. **F** Antenna Directivity at 701nm.

2.5 Design and fabrication summary

As a result of all of the simulations and fabrication done up to this point, I had designs for gold bowtie nanoantennas that should provide a directional enhancement well in excess of 1000 for wavelengths $\lambda = 700 - 750$nm at a gap in the bowtie of $g = 20$nm, which could be reasonably used for enhancement of quantum emitter emission at those wavelengths.

Cylinder dimer designs also exhibited high enhancement factors, though they were smaller than for comparable bowtie antennas, reaching only 350 at a gap $g = 20$nm. The cylinder dimer, though, turned out to be a lot more flexible and stable than the bowtie design — the same size parameters worked for all tested gaps, whereas, for the bowties, adjustments to the geometry were required when changing the gap between the arms of the bowtie.

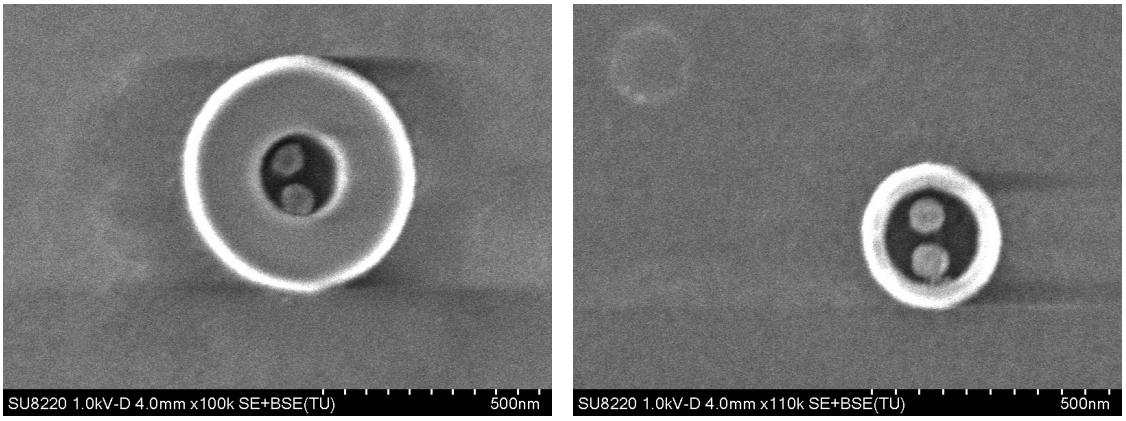

(A) (B)

FIGURE 2.13: SEM Images of fabricated Ring and Dimer nanoantennas. **A** Wide ring nanoantenna. **B** Narrow ring nanoantenna

For the full ring and dimer structure, I have optimized the designs and successfully fabricated nanoantennas that should be able to provide over 300× directional fluorescence enhancement for at a wavelength of 630nm or in excess of 1000× directional enhancement at wavelengths between 700nm and 750nm.

2.6 Characterization

The fluorescence response of gold was experimentally found to be too weak to be able to demonstrate the operating characteristics of the fabricated antennas, i.e. to demonstrate fluorescence enhancement and directivity.

Therefore, to validate the fabricated structures, the scattering spectra of the constituent parts of the hybrid nanoantenna were measured and compared with simulated scattering spectra, showing good correlation. Typical scattering spectra and the corresponding simulations are shown on Figure 2.14. Details on dark field scattering measurements and scattering simulations can be found in Section 2.8.3.1 and Sections 2.8.1.3

For the gold cylinder dimer (Figure 2.14A), experimental polarization-resolved scattering measurements (Figure 2.14D) show two distinct scattering spectra with different resonance positions — red-shifted for incident light polarized parallel to the dimer and blue-shifted for light polarized perpendicular to the dimer. Simulated scattering spectra (Figure 2.14G) show the same trend.

The wide ring structure (Figure 2.14B) exhibits a complex mode structure in experimental scattering measurements (Figure 2.14E), with several strong peaks in the 600nm to 800nm range, which correlate to the positions of the peaks present in the simulated scattering spectra (Figure 2.14H), though direct comparisons between simulated and experimental scattering spectra are difficult to do because of the complexity of simulating dark-field scattering (see Section 2.8.1.3 for more details). Simulated spectra only show one polarization, since, because of the symmetry of the structure, the simulated spectra are identical; Experimental spectra show two polarizations to highlight any features related to asymmetry caused by fabrication imperfections.

The narrow ring structure (Figure 2.14C) exhibits a much simpler mode structure in both experimental scattering measurements (Figure 2.14F) and simulated scattering spectra (Figure 2.14I), with two main peaks at about 550nm and 700nm.

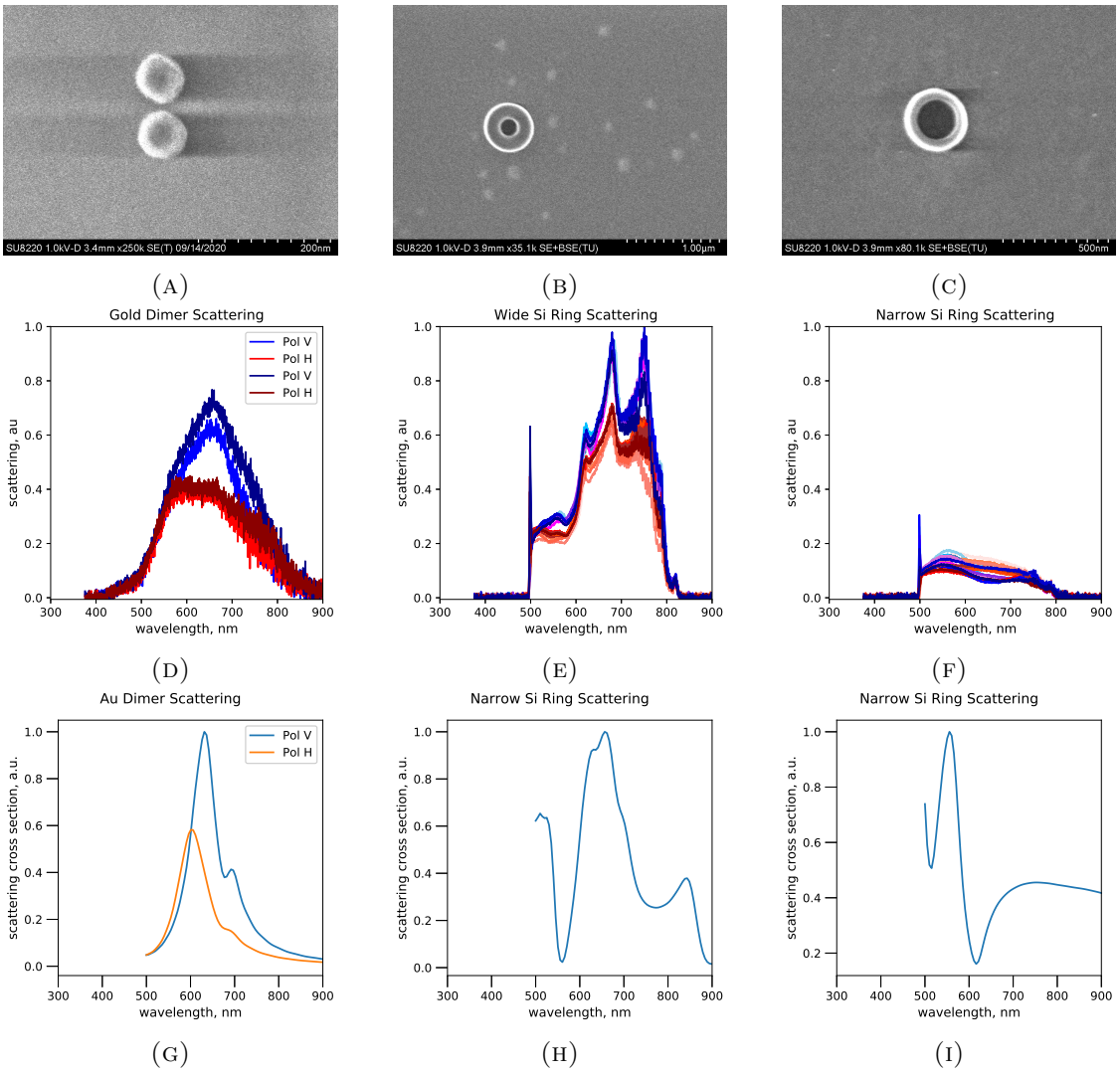

FIGURE 2.14: Au Dimer and Si Ring Scattering measurements and simulated scattering spectra. **A** SEM of Gold Dimer $r = 35$nm, $h = 25$nm, $g = 20$nm. **B** SEM of Wide ring $r_o = 300$nm, $r_i = 100$nm, $h = 150$nm. **C** SEM of Narrow ring $r_o = 150$nm, $r_i = 100$nm, $h = 150$nm. Measured polarization-resolved dark field scattering spectra of **D** the gold dimer, **E** the wide ring and **F** the narrow ring. Cut-off at 500nm in the experimental spectra is caused by a long pass filter in the collection beam path. **G** Simulated scattering spectra for same dimer. **H** Simulated scattering spectra for same wide ring. **I** Simulated scattering spectra for same narrow ring.

2.7 Conclusions

In this Chapter, I have developed two methods applicable to the optimization of hybrid nanoantennas and demonstrated their results on a Ring and Dimer antenna design, with simulations showing the optimized designs demonstrating over 800× directional fluorescence enhancement and over 8× out-of-plane directivity.

A reliable method for fabricating such hybrid nanoantennas has been demonstrated, with complete hybrid nanoantennas fabricated, and all of their constituent components verified by scattering measurements and simulations.

The next step with this design will be, once quantum emitter manipulation and localization is achieved, to fabricate a design optimized for operation with the chosen quantum emitter, and demonstrate enhanced fluorescence and directivity.

2.8 Methods

2.8.1 Numerical Simulations

2.8.1.1 Fluorescence Enhancement and Directivity Simulations

Fluorescence enhancement and directivity simulations were done in Lumerical FDTD, using a method derived from the one described in Ref. [200].

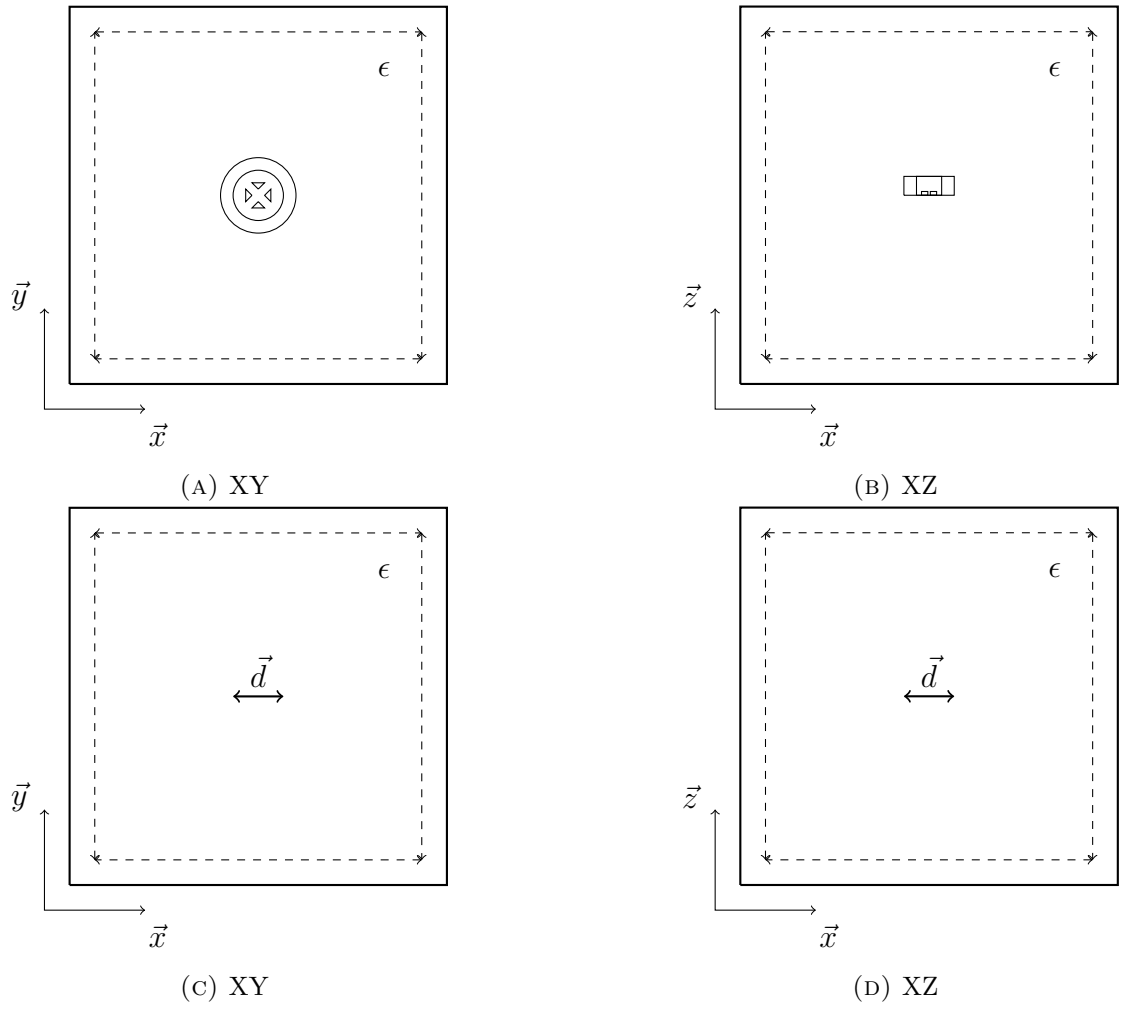

(A) XY (B) XZ

(C) XY (D) XZ

FIGURE 2.15: **A** and **B** Schematic of the ring and bowtie antenna simulation area. Dashed lines represent the box power monitors. ϵ is the permittivity of the medium. Antenna is excited by a single dipole in the center of the bowtie. **C** and **D** Schematic of the normalization simulation. Dashed lines represent the box power monitors. ϵ is the permittivity of the medium. Simulation excited by a single dipole in the center of the bowtie.

A single dipole source was used to excite the whole antenna structure. A box of power and field monitors were used to record radiated power and EM fields — enclosing the whole dipole and antenna system. A second simulation including only the the dipole was done in a similar fashion. Schematics of the simulation are shown on Figure 2.15.

$$\mathrm{EF} = \frac{\gamma_{\mathrm{rad}}}{\gamma_{\mathrm{rad0}}} = \frac{P_{\mathrm{rad}}}{P_0} = \frac{\oint_S < \vec{S} > \cdot d\vec{s}}{\oint_S < \vec{S_0} > \cdot d\vec{s}} \tag{2.1}$$

Where the radiative enhancement if equal to the quotient of radiative decay rates γ_{rad} in the presence on the antenna and γ_{rad0} in a homogeneous environment, which is equal to the quotient of total radiated power P_{rad} in the presence on the antenna and P_0 in a homogeneous environment. Where the total radiated power is the integral of the Poynting vector over the surface of the box monitors.

The same simulation also provide information on the radiation pattern of the antenna — projecting the fields from the box monitors onto a sphere gives us the far-field radiation pattern.

2.8.1.2 Antenna Field Enhancement Simulations

Antenna scattering simulations were done using MEEP [168]. Schematics of the simulation are shown on Figure 2.16.

The antenna structure was excited by a plane wave with normal incidence on the structure, and the field was collected by a single plane monitor. The same simulation was then carried out without the antenna structure. Then, the fields from the the first simulation were normalized by the fields from the second simulation, giving field enhancement caused by the antenna structure.

$$\mathrm{EF}(\vec{x}) = \frac{|\vec{E}_{\mathrm{ant}}(\vec{x})|^2}{|\vec{E}_{\mathrm{norm}}(\vec{x})|^2} \tag{2.2}$$

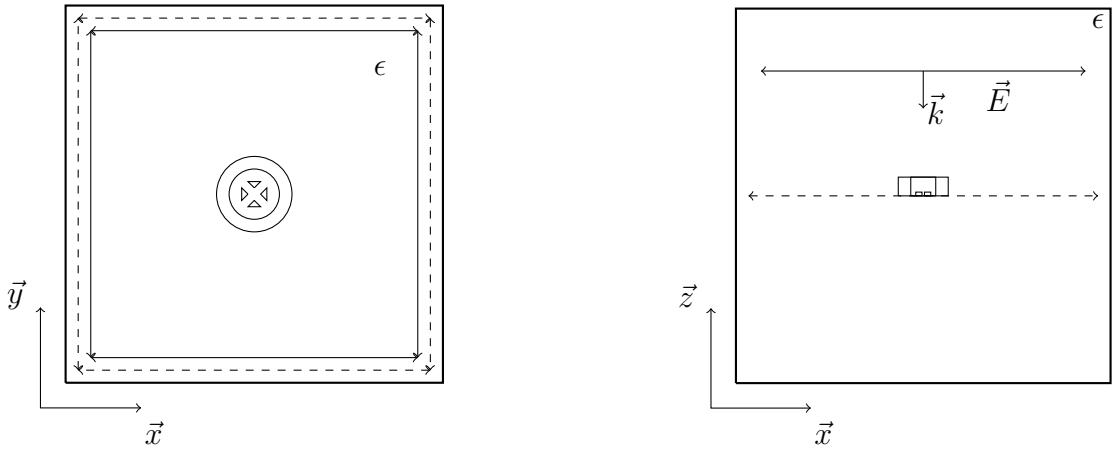

(A) XY (B) XZ

FIGURE 2.16: **A** and **B** schematic of the field enhancement simulation setup. Dashed lines represent plane power monitors. Antenna excited by a plane wave with normal incidence.

2.8.1.3 Antenna Scattering Simulations

Antenna scattering simulations were done in Lumerical FDTD. Dark field scattering experiments are notoriously difficult to accurately simulate [201], so the emphasis on these simulations was simplicity. Schematics of the simulation are shown on Figure 2.17.

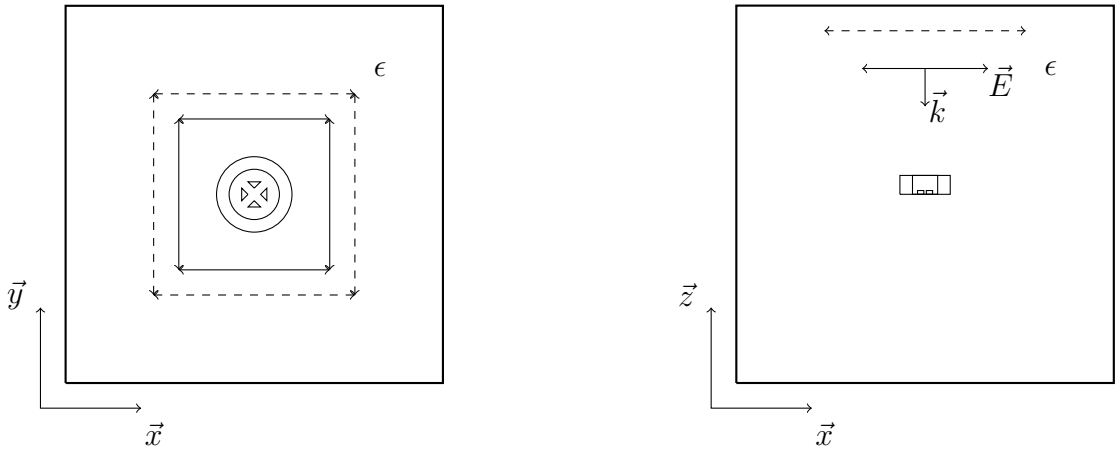

(A) XY (B) XZ

FIGURE 2.17: **A** and **B** schematic of the scattering simulation setup. Dashed lines represent plane power monitors. Antenna excited by a plane wave with normal incidence.

The antenna structure was excited by a plane wave with normal incidence on the structure, and the scattered field was collected by a single plane monitor. The

monitor size simulation area were chosen to collect scattered light up to angles equivalent to the optical setup used for experiments — 0.9NA.

2.8.1.4 Gradient Descent

The gradient descent, or steepest descent method used in my simulations is a simple version of the mathematically rigorous steepest descent method described in Ref. [177].

The original algorithm can be written as follows. For $f(\vec{x})$ defined on $\mathbb{R}^n$ with a defined gradient $\nabla f(\vec{x})$ over the same $\mathbb{R}^n$, to minimize $f(\vec{x})$ from a starting $\vec{x}_0$, for iterations $i = 1, 2...$, at every step choose a direction $\vec{u}_i$ with the maximum gradient and choose a step size giving the minimum value of $f(\vec{x})$ in the direction, thus setting $\vec{x}_i = \vec{x}_{i-1} + \lambda_i * u_i$.

1. $\vec{u}_i = \frac{-\nabla f(\vec{x}_{i-1})}{||\nabla f(\vec{x}_{i-1})||}$
2. $\vec{x}_i = \vec{x}_{i-1} + \lambda_i \vec{u}_i$, where λ_i is chosen such that $f(\vec{x}_{i-1} + \lambda_i \vec{u}_i) = \min_\lambda f(\vec{x}_{i-1} + \lambda_i \vec{u}_i)$

The algorithm is terminated when at least one of the following criteria is met: either the distance between two adjacent steps is less than ϵ_1, the gradient at a evaluation point is less than ϵ_2, or the difference between the value of $\vec{f}(x)$ at two adjacent points is less than ϵ_3.

1. $||\vec{x}_i - \vec{x}_{i-1}|| < \epsilon_1$
2. $||\nabla f(\vec{x}_i)|| < \epsilon_2$
3. $||f(\vec{x}_i) - f(\vec{x}_{i-1})|| < \epsilon_3$

When applied to my problem, where every simulation is computationally intensive, the method was simplified, losing the explicit calculation of the the gradient and following choice of size of step by minimizing (or maximizing) the function along the chosen optimization direction. In my case, which was limited to a 2D, 2 parameter, discretized optimization, the algorithm became, for $f(x, y)$, and $\vec{x}_0 = (x_0, y_0)$, and minimum steps dx, dy:

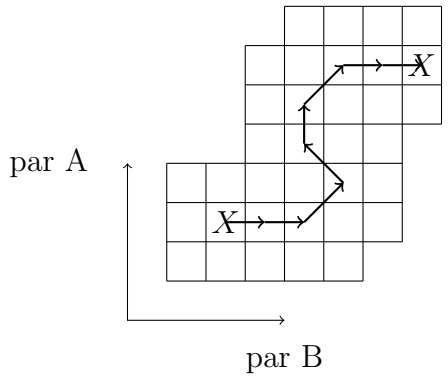

FIGURE 2.18: Schematic representation of walking up the gradient in a 2 parameter optimization, where each arrow indicates a shift to a position with a higher value of the function being optimized.

1. for $i, j = -1, 0, 1$ calculate $f(\vec{x}_{i,j})$, where $\vec{x}_{i,j} = (x_{n-1} + dx * i, y_{n-1} + dy * j)$
2. set $\vec{x}_n$ to $\vec{x}_{i,j}$ for which $f(\vec{x}_{i,j})$ is minimized
3. terminate algorithm if $\vec{x}_n = \vec{x}_{n-1}$

Such a naive approximation of the full steepest descent algorithm is highly prone to getting stuck in local maxima (minima), but is very easy to implement and requires a small number of simulations for every optimization iteration. As was later shown by genetic optimizations, this naive optimization was sufficient to achieve optimal antenna design parameters. A graphical schematic of the algorithm can be seen in Fig. 2.18

2.8.1.5 Evolutionary Optimization

A evolutionary optimization algorithm is an algorithm that mimics natural selection and evolution to optimize a function [202]. A simple genetic algorithm parametrizes the function to be optimized (usually into a fixed-length 2 bit signature). One then generates (usually randomly) a set of candidate solutions to the problem, called a generation. Of the generation, a certain percentage of candidates is selected to continue on to the next generation, based on the performance of each candidate, whereas the remaining candidates are replaced by "offspring" of the selected solutions. Offspring are generated by mixing elements of the parameter signature of pairs of solutions and potentially mutating the signature to generate new solutions. This process can be continued for any number of generations.

After the completion of the evolutionary process, the best candidates can be selected as the final result of the optimization.

A step-by-step description of such a process can look like:

1. Start with a randomly generated population of n candidate solutions to a problem.
2. Calculate the fitness value of each solution in the population.
3. Repeat the following steps until n offspring have been created:
    - Select a pair of "parents" from the current population, the probability of selection being an increasing function of fitness. Selection is done "with replacement", meaning that the same chromosome can be selected more than once to become a parent.
    - With a certain probability, randomly mix the parameters of "parents" to form two offspring. If no crossover takes place, form two offspring that are exact copies of their respective parents.
    - Mutate the parameters of the two offspring with a certain probability, and place the resulting new sets of parameters in the new population.
4. Replace the current population with the new population.
5. Go to step 2.

The implementation used for my purposes is a Python library called DEAP [203], designed for implementation of evolutionary algorithms, from simple ones like described above to highly complex evolutionary schemes outside the scope of this work.

2.8.2 Fabrication

The whole hybrid antenna structure fabrication process is shown on Figure 2.19. Details on each step of the process are written below. To fabricate only gold dimer structures, only steps $9-12$ are required, while fabricating pure silicon structures can be done using steps 1 and $6-8$.

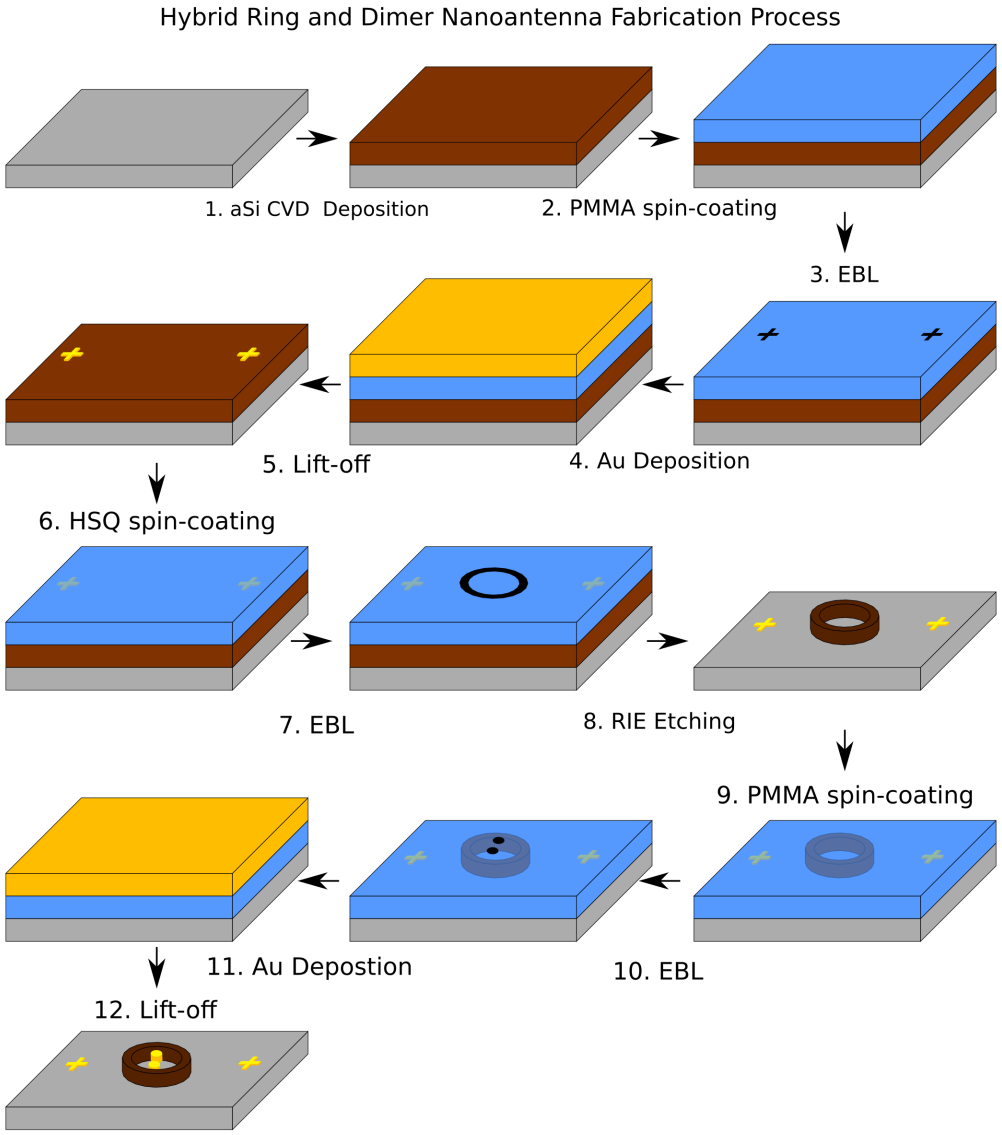

FIGURE 2.19: Schematic detailing fabrication process for hybrid ring-dimer nanoantenna.

1. First, I deposited ≈ 250nm of amorphous silicon by ICP-CVD (Oxford PlasmaPro 100) at 250°C from a SiH_4 precursor (45 sccm SiH_4 and 30 sccm Ar at 8mTorr process pressure, 50watts RF power at 20 DC forward bias and 3000watts ICP RF power) onto a quartz substrate.

2. Poly(methyl methacrylate), PMMA 495K A4, further diluted 1:1 in anisole, spin coated at 3000 rpm for 1 minute and then baked at 180°C for 2 minutes; and a change dissipation layer (Espacer 300AX01), spin coated at 1500 rpm for 1 minute were used for the EBL writing.

3. Alignment markers were written using EBL (Elionix ELS-7000), at an acceleration voltage 100kV and a current of 100pA, with a dose of $\approx 3\text{mC/cm}^2$. After that, the resist was developed in a solution of Methyl isobutyl ketone in isopropyl alcohol (MIBK:IPA 1:3) at $-10°\text{C}$ for 15 seconds and then rinsed by de-ionized water to stop the development.

4. Then I deposited 40nm of gold onto the sample with a 2 nm titanium adhesion layer by EBPVD (Denton Explorer) at a rate of $0.5\mathring{A}/s$.

5. Lift-off of the PMMA resist was done in 1-meythl-2-pyrrolidone at room temperature for 24h.

6. For writing the rings, hydrogen silsesquioxane e-beam resist (Dow Corning XR-1541-06), spin coated at 5000 rpm for 1 minute and a change dissipation layer (Espacer 300AX01), spin coated at 1500 rpm for 1 minute were used.

7. EBL (Elionix ELS-7000) was done at an acceleration voltage 100kV and a current of 500pA, with a dose of $\approx 300\text{mC/cm}^2$. The mask was aligned to the the previously fabricated alignment markers. The sample was then developed by NaOH/NaCl salty solution (1% wt. /4% wt. in de-ionized water) for 60 seconds and then rinsed by de-ionized water to stop the development.

8. The ring structures were created by ICP-RIE etching (Oxford Plasmalab 100) using chlorine gas (22 sccm Cl_2 at 5mTorr process pressure, 100watts RF power and 300watts ICP RF power).

9. For the gold dimer structures, Poly(methyl methacrylate), PMMA 495K A4, further diluted 1:1 in anisole, spin coated at 3000 rpm for 1 minute and then baked at 180°C for 2 minutes; and a change dissipation layer (Espacer 300AX01), spin coated at 1500 rpm for 1 minute were used for the EBL writing.

10. The dimer structure was written using EBL (Elionix ELS-7000), with the mask aligned to the previously fabricated alignment markers, at an acceleration voltage 100kV and a current of 100pA, with a dose of $\approx 3\text{mC/cm}^2$. After that, the resist was developed in a solution of Methyl isobutyl ketone in isopropyl alcohol (MIBK:IPA 1:3) at $-10°\text{C}$ for 15 seconds and then rinsed by de-ionized water to stop the development.

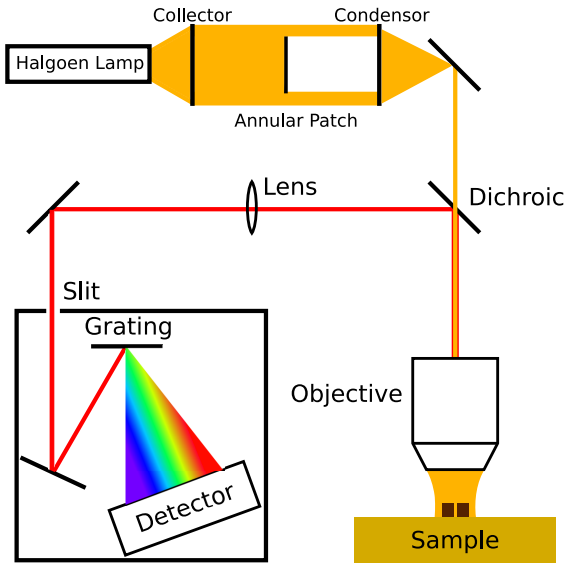

FIGURE 2.20: Schematic representation of dark-field scattering measurement setup

11. Then I deposited 25nm of gold onto the sample with a 2 nm titanium adhesion layer by EBPVD (Denton Explorer) at a rate of $0.5\mathring{A}\ /s$.

12. Lift-off of the PMMA resist was done in 1-meythl-2-pyrrolidone at room temperature for 24h.

2.8.3 Optical Characterization

All optical measurements were performed in a microspectrometer setup, based on an inverted microscope (Nikon Ti-U) and a spectrometer system (Andor SR-303i spectrograph with a 150 lines/mm grating coupled to a 400 × 1600pixel Andor Newton 971 EMCCD). Incident light was focused on the sample by a 100× objective lens with a 0.9NA (Nikon LU Plan Fluor). Signal collected by the same objective lens was then projected onto the spectrograph entrance slit with a width of 250μm.

2.8.3.1 Dark-field scattering

For dark-field scattering, white light from a halogen lamp was used to excite the sample, with the, central, low-$\vec{k}$ portion of the beam blocked from entering the objective lens by a annular patch, meaning only light scattered by the nanoantennas

was collected and sent to the spectrograph. Reflectance of an aluminum mirror was used as a reference.

Chapter 3

Quantum emitter localization

I explored several techniques for the localization and/or manipulation of single quantum emitters. The techniques that I looked at can be loosely separated into two main groups — the precise manipulation of emitters, and controlled creation of emitters.

For the first group, I looked at using AFM pick-and-place methods to position nanodiamonds [141, 142, 122, 123] and using a hollow AFM tip to print quantum dots suspended in liquid [204]. Both methods were ultimately found to be unsuitable for my purposes.

AFM pick-and-place techniques turned out to be unsuitable for the equipment that was readily available to me. AFM printing of quantum dots was successful in precisely delivering quantum dots to the nanoantennas. PL measurements demonstrated spectral modification of the QD signal in the presence of the nanoantennas. Unfortunately, the method was unable to show sufficient control over the printed volume to make quantitative measurements possible.

The second group of techniques included direct writing of emitters using EBL [147] and deterministic creation of emitting defects in 2D materials[150, 151, 152, 154, 155, 124].

Deterministic creation of emitting defect in hexagonal boron nitride, hBN, seemed like a promising method, with a lot of published literature and seemingly straightforward processes, but ended up being unsuccessful. Creating emitters from hydrogen silsesquioxane, HSQ, e-beam resist was the only fully successful method of creating and coupling localized emitters to nanoantennas.

As a final note, I looked at ways of distributing non-localized emitters, either by simple spin-coating or more sophisticated self-assembly [205, 206, 207, 208] of nanoplatelets or quantum dots; or through the mechanical transfer of large areas of epitaxially grown 2D material flakes [209], and the possibility of utilizing them for my antenna.

3.1 Localized emitter manipulation

3.1.1 AFM Manipulation

For AFM manipulation of single emitters, there are two main approaches: using the AFM tip to push the emitter to the desired location, or to get the emitter to stick to the tip, move the tip to the desired location and then detach the emitter. While the second approach makes positioning the emitter a relatively easy task, getting the emitter to detach from the the tip can be a challenge.

The first approach is applicable to relatively large objects like nanoparticles [138, 139] or, rarely, polymer-coated quantum dots [140]. This is one limiting factor, the other being the inability to move an object into a enclosed shape, like my Ring and Bowtie antenna design from Chapter 2.

The second approach requires one to press the AFM tip into the emitter until it sticks to the tip, and then repeat the process at the target location until the emitter is deposited [122, 123].

I attempted to reproduce those results with nanodiamonds. Nanodiamonds were selected as they are very efficient single photon sources when they posses nitrogen vacancy (NV) or silicon vacancy (SiV) color defects [210, 211, 212]. On Figure 3.1 I show a SEM image of a cluster of nanodiamonds stuck to the side of an AFM tip. This was achieved by progressively pressing the AFM tip closer and closer to the surface of the sample until it touched the cluster of nanodiamonds during a scan.

The AFM setup used was an attocube tuning fork-based AFM.

A big drawback of tuning fork AFMs is that they are inherently exclusively tapping-mode AFMs, in that the tip is constantly vibrating and cannot be lowered to be into constant contact with the surface, as conventional laser deflection-based AFMs would be capable of. This means that all contact with the surface or any objects that one is trying to interact with is intermittent — making controlling the force of interaction with objects on the surface quite difficult.

Because of this, I was unable to achieve consistent detachment of nanodiamonds from the AFM tip, in this setup. Another potential issue was getting the attached nanodiamonds to the hot spot of the antenna, which was located deep inside the

antenna structure. Because of this, and the fact that other approaches had started yielding good results, this approach wasn't developed further.

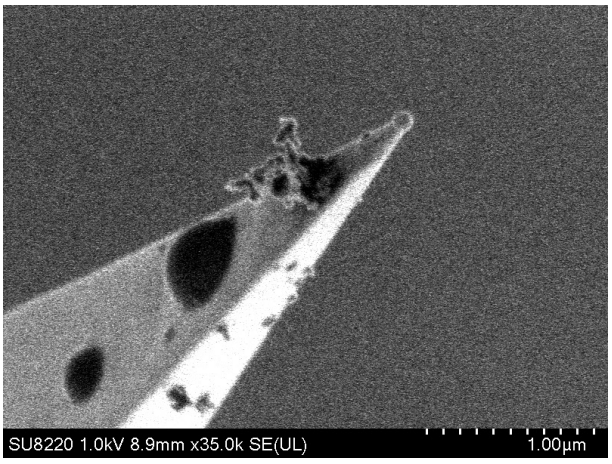

(A)

FIGURE 3.1: SEM image of AFM cantilever with attached clump of nanodiamonds.

3.1.1.1 Emitter Attached to Tip

Another AFM-related option to demonstrate the interaction of a single emitter and an antenna is using an AFM tip with either an embedded, or previously attached emitter [137] to scan over the surface. This could demonstrate the dependence of the antennas operating efficiency on the relative position of the antenna and the emitter as well as perform spatial mapping of the LDOS. For this I looked two different approaches: either attaching emitters to tips myself (e.g. as demonstrated in Fig. 3.1), or using ready-made tips with attached/embedded emitters.

Unfortunately, adapting the AFM setup available to me to perform the fluorescence measurements was not feasible, so the plan was abandoned.

3.1.2 Cytosurge quantum dot printing

In [204] a method for nanoscale delivery of liquids via a hollow AFM probe was presented. The method consists of an AFM probe that has an FIB-milled channel, coupled to a liquid reservoir. By applying positive air pressure to the reservoir, one can dispense the liquid from the reservoir through the AFM probe. It allows, in principle, printing of various liquids with sub-micron linewidths at nanoscale, AFM-level precision.

I attempted to use the same method to print quantum dots suspended in solution onto my Ring and Dimer antennas from Chapter 2.

Results of printing are shown on Figure 3.2. Figure 3.2A shows optical image of sample with antennas covered by drops containing quantum dots, while Figure 3.2B shows wide-field fluorescence imaging of the same area, with the quantum dot-containing drops clearly visible. The printing itself was quite straightforward. The AFM probe was used to scan the sample and locate the precise location of the antennas, then, since the aperture of the probe was almost at the exact location as the tip, aligning the aperture with the antenna was as simple as moving the probe to the antenna location as per the AFM scan. Control of the printing QD volume was discovered to be much more difficult — even on Figure 3.2A it can be clearly seen, that different printed droplets have visibly different sizes. This was later to be shown to be a insurmountable problem for this method — since measuring enhancement of quantum dot emission requires a stable reference, and without good control of QD printing volume, getting a reliable reference isn't possible.

Measuring fluorescence signal from the reference quantum dots and the quantum dots deposited on the antennas showed some spectral modification in the presence of the antennas, as is shown on Figure 3.3A. Unfortunately, the quantum dot printing method did not provide enough control over the deposited volume, meaning that no quantitative measurements were possible. Figure 3.3B shows the reference quantum dots showing over 5× stronger PL signal, than the quantum dots coupled to the antennas, without any reliable way to verify the number of quantum dots in either of the cases. This means even if there is detectable interaction between the quantum dots and the antennas, no enhancement measurements are possible, because it isn't possible to have a stable reference measurement.

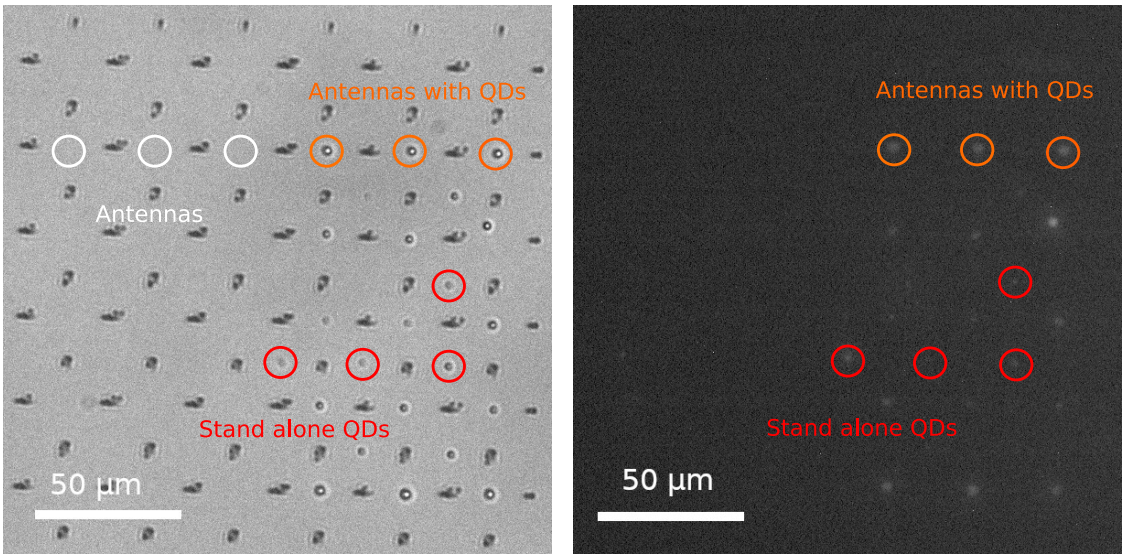

(A) (B)

FIGURE 3.2: **A** Optical image of Ring and Dimer Antennas with printed quantum dots on them. **B** Wide-field fluorescence image showing fluorescence from printed quantum dots. Each antenna is surrounded by marks pointing towards the antenna. The antennas themselves are not discernible in these images. Locations of several antennas are highlighted in white. Orange highlights a few antennas that have had quantum dots deposited on them. Red highlights a few locations without antennas that had quantum dots deposited as a reference.

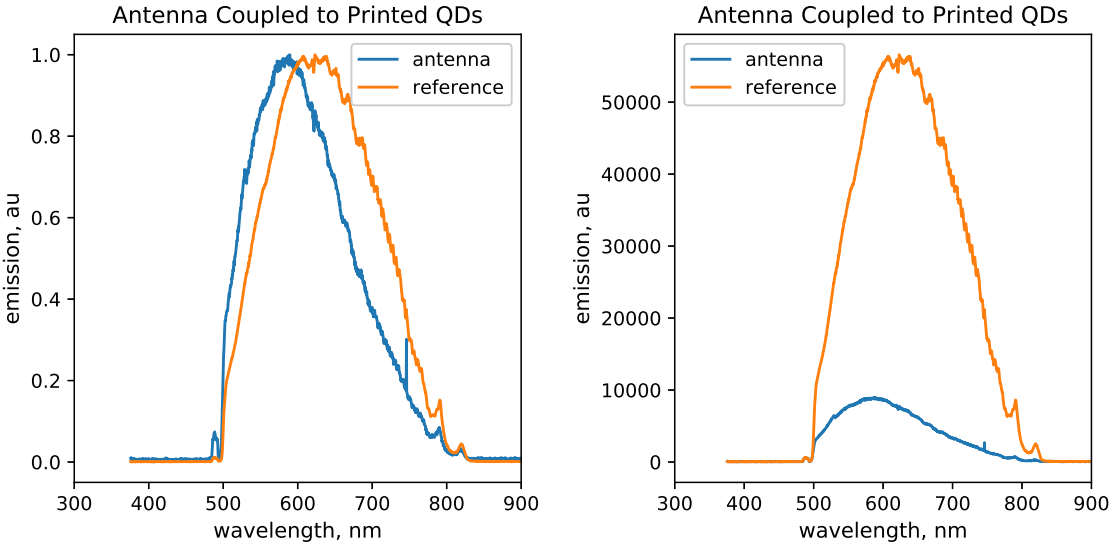

(A) (B)

FIGURE 3.3: **A** Normalized PL spectra of quantum dots (orange) and quantum dots coupled to a nanoantenna, showing spectral modification. **B** Same spectra, but without normalization, showing the impossibility of quantitative measurements of fluorescence enhancement.

3.2 Localized emitter fabrication

3.2.1 Direct writing of emitters — HSQ

HSQ resist is known to form emitting silicon nanocrystals after thermal annealing [146] or e-beam exposure [147]. Depending on fabrication conditions and resulting nanocrystal sizes, photoluminescence spectra with peaks ranging from 650 nm to over 1000 nm [213, 214, 215] and quantum yields of up to 60% [216] have been reported.

Thermal annealing is not a viable method for my purposes, since the plasmonic antennas that I fabricate are made out of gold, which can degrade at temperatures required to produce emitting nanocrystals out of HSQ — this can be seen on Figure 3.4, which shows photos of HSQ- and gold- coated substrate before and after thermal annealing at 1100 deg C, the temperature used nanocrystal growth in HSQ [146]. The gold layer can be seen to have almost completely degraded after the annealing process.

(A) (B)

FIGURE 3.4: **A** Silicon substrate coated with gold and HSQ before annealing. **B** Silicon substrate coated with gold and HSQ after annealing, showing significant degradation of gold layer.

Therefore, e-beam exposure was the chosen technique for emitting nanocrystal fabrication. I used EBL with precise mask alignment to fabricate SiO_2 pillars from HSQ resist, using the same conditions as described in Chapter 2 Section 2.8.2.

Mask alignment to an array of gold dimers allowed me to embed the gold dimers in HSQ pillars.

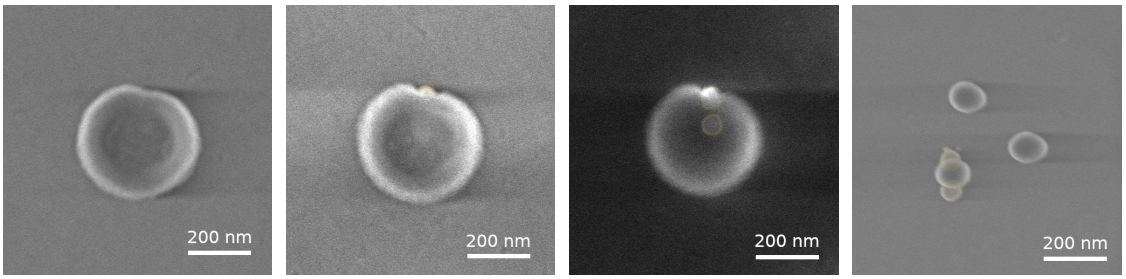

(A) (B) (C) (D)

FIGURE 3.5: **A** SEM of a stand-alone HSQ cylinder. **B** SEM of an HSQ cylinder with Au dimer embedded inside. **C** Same HSQ cylinder, but SEM done at higher acceleration voltage to see Au Dimer through the HSQ. **D** HSQ cylinders misaligned with an Au Dimer. Au dimers false-colored yellow to make it easier to distinguish them.

SEM images of the fabricated structures are shown on Figure 3.5. Figure 3.5A shows a stand-alone HSQ pillar, Figure 3.5B and C show a HSQ pillar with an Au dimer embedded inside. Figure 3.5B was taken at a higher acceleration voltage, so that the embedded dimer could be more clearly seen.

The photoluminescence spectra exhibited by the two fabricated pillars from Fig 3.5A and Fig 3.5B are shown on Figure 3.6A and Figure 3.6B, respectively.

The gold dimer embedded in the HSQ pillar demonstrated photoluminescence enhancement, as can be seen on Figure 3.6B.

The measured enhancement of fluorescence from HSQ cylinders when containing an embedded gold dimer does not exceed 3×, despite the fact that in Chapter 2, Section 2.4, Figure 2.11, the gold dimer is simulated to provide over 300× enhancement. This is caused by the small volume of the dimer hot spot where field enhancement occurs — with many papers estimating the hot spot volume to be approximately equal to the gap volume [192, 193, 170, 217].

Thus, we can estimate the expected enhancement of such a system:

$$V_{\text{dimer}} \approx \frac{4}{3}\pi r_d^3 \tag{3.1}$$

$$V_{\text{cylinder}} \approx \pi r_c^2 h \tag{3.2}$$

Where V_{dimer} is the volume of the dimer hot spot, which has a gap of ≈ 20 nm, meaning that $r_d \approx 10$ nm, and where V_{cylinder} is the volume of the HSQ cylinder, which has a radius $r_c \approx 140$ nm. According to the HSQ spin-coating parameters and the spin-curves of HSQ resist [218], the height of the HSQ cylinder $h \approx 40$ nm.

With these numbers,

$$
\begin{aligned}
V_{\text{dimer}} &\approx \frac{4}{3}\pi r_d^3 && (3.3)\\
&\approx \frac{4}{3}\pi(10)^3 && (3.4)\\
&\approx 4.2e^3 \text{ nm}^3 && (3.5)\\
V_{\text{cylinder}} &\approx \pi r_c^2 h && (3.6)\\
&\approx \pi(140)^2 \times (40) && (3.7)\\
&\approx 2.5e^6 \text{ nm}^3 && (3.8)
\end{aligned}
$$

Assuming an even distribution of emitting nanocrystals over the whole cylinder volume, emission intensity of the HSQ cylinder will be proportional to the cylinder volume, while emission intensity from the cylinder with an embedded dimer will be the sum of the enhanced dimer volume and the rest of the cylinder. Assuming a uniform enhancement factor of $E \approx 320$, as was estimated in Chapter 2, we can get an estimate for the average enhancement:

$$
\begin{aligned}
I_{\text{cylinder}} &\propto V_{\text{cylinder}} && (3.9)\\
I_{\text{dimer}} &\propto V_{\text{cylinder}} + V_{\text{dimer}} * E && (3.10)\\
E_{\text{avg}} &\approx \frac{I_{\text{dimer}}}{I_{\text{cylinder}}} && (3.11)\\
&\approx \frac{2.5e^6 + 4.2e^3 * 320}{2.5e^6} && (3.12)\\
&\approx \frac{3.8e^6}{2.5e^6} && (3.13)\\
&\approx 1.5 && (3.14)
\end{aligned}
$$

As a result of this very simple estimate, we expect an enhancement factor of around $E = 1.5$, which is similar to, but slightly lower than the measured enhancement. The fact that the measured enhancement is higher than the estimate can be explained by the fact that the estimate, among other things, doesn't take into account the volume of the dimer inside the cylinder and assumes a homogeneous distribution of emitting nanocrystals inside the dimer.

To increase the apparent emission enhancement, the simplest thing to do would be to decrease the size of the HSQ cylinder, but this would increase the required EBL mask alignment precision, which already is the main challenge with this technique. Figure 3.5D shows the misalignment from 3 EBL runs in the same conditions, meaning that for good alignment, each fabricated array must include variable shifts to optimize alignment — increasing complexity by an order of magnitude if trying to add HSQ pillars to already fabricated hybrid Ring and Bowtie antennas.

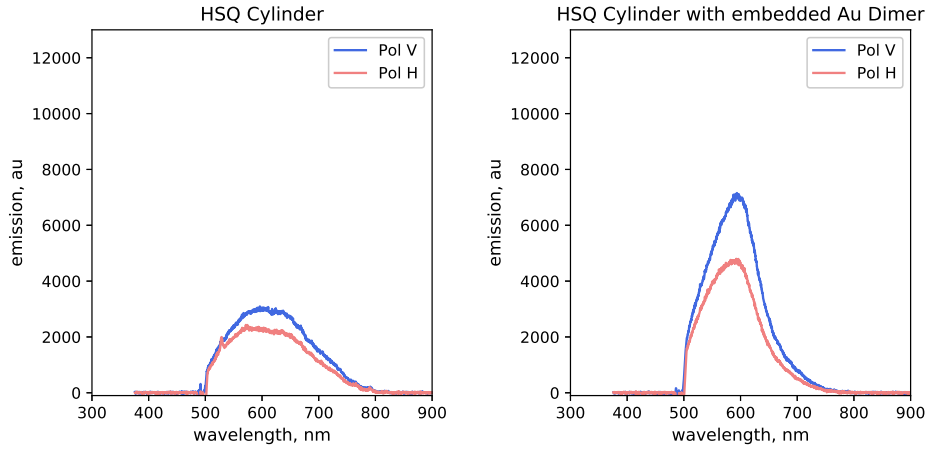

(A) (B)

FIGURE 3.6: Polarization-resolved photoluminescence measurements of **A** Pure HSQ cylinder, **B** HSQ cylinder with embedded Au Dimer. Pol V refers to excitation laser polarized along Au Dimer axis, Pol H - perpendicular to dimer axis.

3.2.2 Direct writing of emitters — hBN

Hexagonal boron nitride, hBN, has been shown to support single photon emitting defects [150, 151, 152, 154, 155]. There is also published work on coupling these SPEs to plasmonic nanoantennas [157].

Most published methods for creating the SPE in the visible spectrum range are based on a combination of annealing and plasma treatment of either bulk hBN or thin hBN flakes. Methods published by different groups vary widely and are often contradictory — some require annealing in oxygen, while others make a point of stating that annealing must be done in an inert, often argon, atmosphere.

More recently, in [124] a method for deterministic creation of these defects by FIB milling of hole in thin hBN flakes has been demonstrated. A similar method described in [158], using e-Beam irradiation yielded similar results, but in the UV spectral range.

While most papers agree that SPE defects appear at grain boundaries, flake edges and other hBN crystal defects [154, 151], some insist on the presence of SPEs in continuous areas of hBN, away from the grain boundaries [219, 220]. In the case of FIB milling, the milled holes create new edges and defects in the crystalline structure that can then host the emitting defects, which should appear after annealing or plasma treatment. The nature of these defects is also debated, with some papers showing a defining role of carbon in defect creation [156, 221], while others show oxygen as having the defining role [154, 222] and others show nitrogen-vacancy style defects as the emitting defects [223].

I made numerous attempts at reproducing results of these published studies, using exfoliated hBN flakes from various sources, with thicknesses varied from over 100nm to below 10nm. Annealing conditions were varied with temperatures from 750 degrees to over 1100 degrees, done in vacuum and in ambient atmosphere, following recipes from papers cited above.

For plasma treatment I explored oxygen and argon plasma, also mimicking published recipes.

For samples where I was attempting to repeat FIB milling experiments from [124], FIB milling was done using Ga ions on a Zeiss Crossbeam 540 FIB-SEM, again, mimicking conditions from the paper.

Figure 3.7 show typical results of my SPE creation experiments in hBN flakes. Fig. 3.7A shows an optical image of an exfoliated hBN flakes after FIB milling, showing the milled holes; Fig. 3.7B shows the same flake in SEM during the FIB

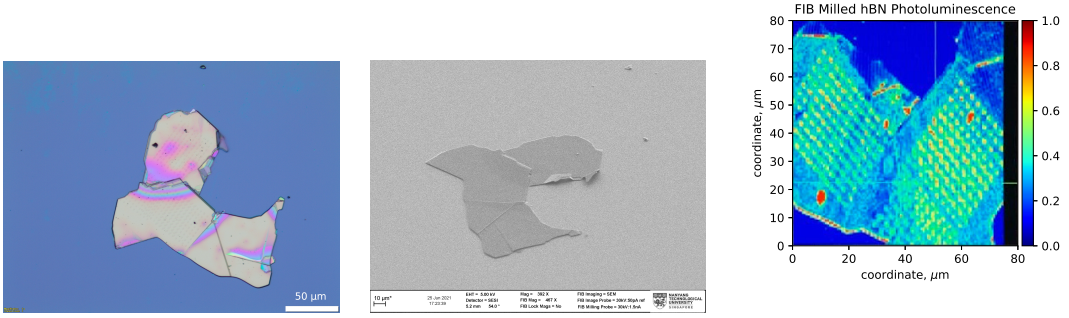

(A) (B) (C)

FIGURE 3.7: Three images of same hBN flake: **A** Optical image with milled holes visible. **B** SEM image of flake during FIB milling. **C** Photoluminescence map of hBN flake, showing some slight increase in photoluminescence intensity near milled holes.

milling experiments, Fig. 3.7C shows a PL map of the flake after milling (532nm excitation wavelength), where the milled holes are clearly visible with slightly higher PL intensities, and several holes seem to demonstrate much stronger PL, relative to the background. Unfortunately, attempts at measuring the spectrum of the bright points on the flakes invariably led to the bleaching of the emitters, preventing me from quantifying the type of emitters produced by FIB milling and subsequent annealing or plasma treatment. This rapid bleaching emitters has also been noted in published literature and is usually attributed to interaction of oxygen with the emitting defects under laser illumination [224, 223, 225, 226].

As a result I have been unable to reproduce reported stable hBN-based SPEs.

All of this seems to indicate that there is a lack of understanding as to the nature of the hBN-based SPEs — How they are created and what their chemical composition is, meaning that in all of the above works, the researchers stumbled upon a method that works, but didn't identify the crucial element of the process.

3.3 Non-localized emitters

All the previous methods I discussed attempt to precisely position emitters to later couple them to antennas.

Most published work on coupling antennas to quantum emitters attempt to homogeneously, randomly, distribute emitters and then demonstrate that antennas make the signal from the emitters brighter than the background, e.g. [10] or [79]. This is much simpler, and in many cases sufficient to demonstrate the desired effect, but makes it difficult to distinguish pure nanoantenna-enhanced signal from background fluorescence.

A recent paper, though, [132], started with the same premise of coupling non-localized emitters to a resonator located above the emitting material, MoS_2, but later exposed the substrate to Ar plasma, etching away the MoS_2 everywhere, except directly under the resonator, effectively localizing the emitting material under the resonator.

This method wouldn't work for the existing Ring and Bowtie design from Chapter 2, because the antenna hot spot is located inside the antenna structure, between the two gold dimer cylinders.

But a different class of nanoantenna designs, particle-on-mirror nanoantennas, as shown in [10, 12, 93] have the hot spot located between a metal substrate and antenna structure. For these types of antennas, the method of quantum emitter localization described above is perfectly suitable. Fabrication of such a hybrid system with quantum emitters will be shown in Chapter 4.

3.3.1 2D materials

Building on experience from working with hBN and attempts at creating single photon emitters, 2D material-based emitters were an obvious choice for antennas sandwiching emitters between the antenna and the substrate. WS_2 is a good choice of material because of strong and relatively uniform room-temperature photoluminescence from monolayer triangles as was shown in [127] and also by our measurements, as seen on Figure 3.8a. Also there have been a number of published

works on coupling WS_2 to resonators, proving that this is a viable concept [128, 129, 130, 131].

CVD-grown or MBE-grown WS_2 monolayer triangles are relatively easy to transfer from their substrate to the target substrate, by sticking them to a PMMA support layer and then using HF to etch the substrate, leaving the WS_2 triangles attached to the PMMA film, which can then be deposited on any target substrate [209] (example on Figure 3.8b, Gold-coated substrate).

The main difficulty encountered during my experiments with WS_2 was the degradation of the triangles during further nanofabrication processing steps — ALD of Al2O3, CVD of aSi all degraded the triangles, making them unusable to for photoluminescence measurements. This meant that the flakes needed to be mechanically covered by a protective layer to prevent chemical interaction during subsequent processing. This could be done by mechanically transferring hBN flakes, but would defeat the purpose of having a large area of non-localized emitting material — without the hBN flakes any subsequent processes would not require any precise alignment, while added the hBN protection flakes would again require me to align my EBL mask for antenna writing.

Another consideration for 2D material-based emitters and coupling them to nanoantennas, is their effective dipole orientation, which, for such monolayer emitters, has been shown to be mostly in-plane [227], as will be discussed in more detail in Chapter 4, Section 4.6.6, would be very inefficient for coupling to my antenna design.

3.3.2 Quantum dot and nanoplatelet self-assembly

Another common method for creating a uniform luminescent layer is depositing a monolayer of colloidal quantum dots [228] or nanoplatelets [229]. The simplest way to deposit quantum dots or nanoplatelets is spin-coating, but experimentally I found that nanoplatelets tend to clump and don't form good uniform layers. Therefore, for nanoplatelets a slightly more complicated self-assembly procedure was used, while spin-coating of quantum dots delivered good results.

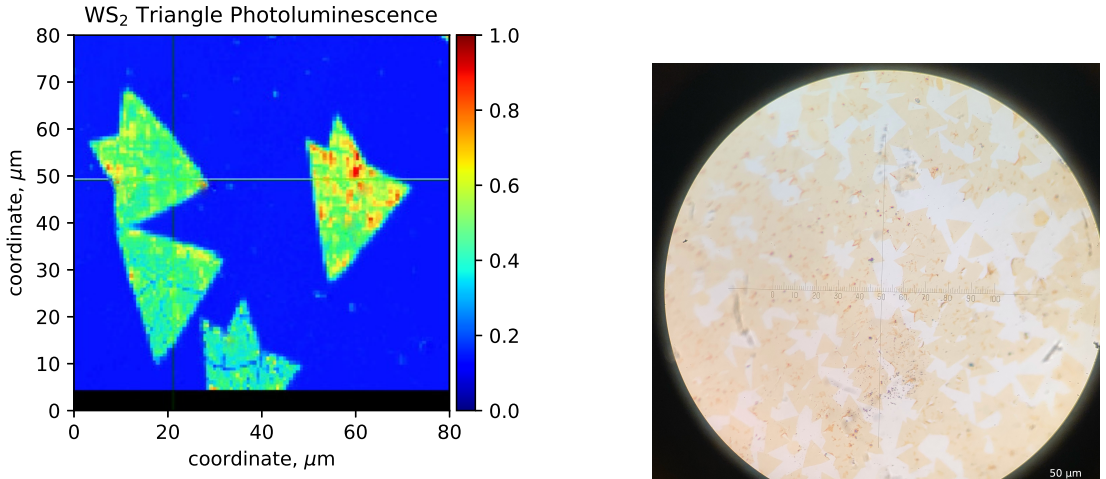

(A) (B)

FIGURE 3.8: **A** Photoluminescence map of WS_2 triangles, showing relative uniformity of PL in undamaged triangles. **B** Optical image of WS_2 triangle after transfer from sapphire substrate to Gold-coated substrate.

3.3.2.1 Nanoplatelet self-assembly

To produce uniform nanoplatelet monolayers, simple spin coating was found to be unsuitable, because the nanoplatlets had a tendency to form tendril-like clumps on the substrate, as can be seen on Figure 3.9.

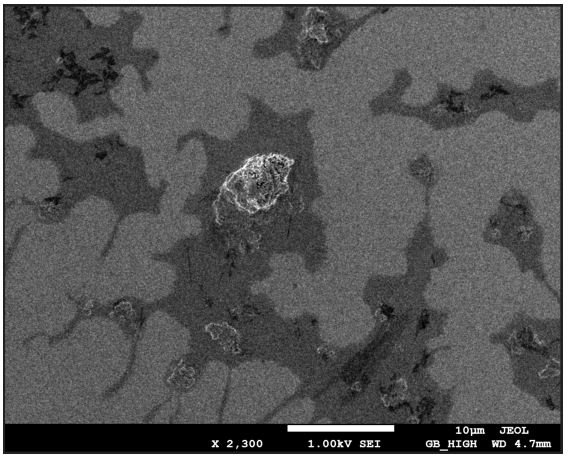

FIGURE 3.9: SEM image of spin-coated nanoplatelets, showing distinct tendril-like structures.

Since nanoplatelets typically have a thin (thickness usually single-digit nanometers), rectangular shape (tens of nanometers long and wide) [229], therefore arranging them in a uniform layer on a substrate can be done in two different ways: all

of the nanoplatelets lying face down (See Figure 3.10b), or all of the nanoplatelets arranged edge-up (See Figure 3.10b). This kind of orientation control, along with near-total uniform surface coverage is possible using self assembly procedures based on floating the nanoparticles on a surfactant. This has been demonstrated on various types of nanocrystals [207, 208, 230, 231], and, more recently, on nanoplatelets [232, 205, 206, 229].

Of particular interest is the procedure described in [206], where choice of subphase, either ethylene glycol (EG) or acetonitrile (ACN) determines the orientation of the resulting layer of nanoplatelets. The procedure is shown on Figure 3.10a, and resulting monolayers of NPLs are shown on Figure 3.10b and c.

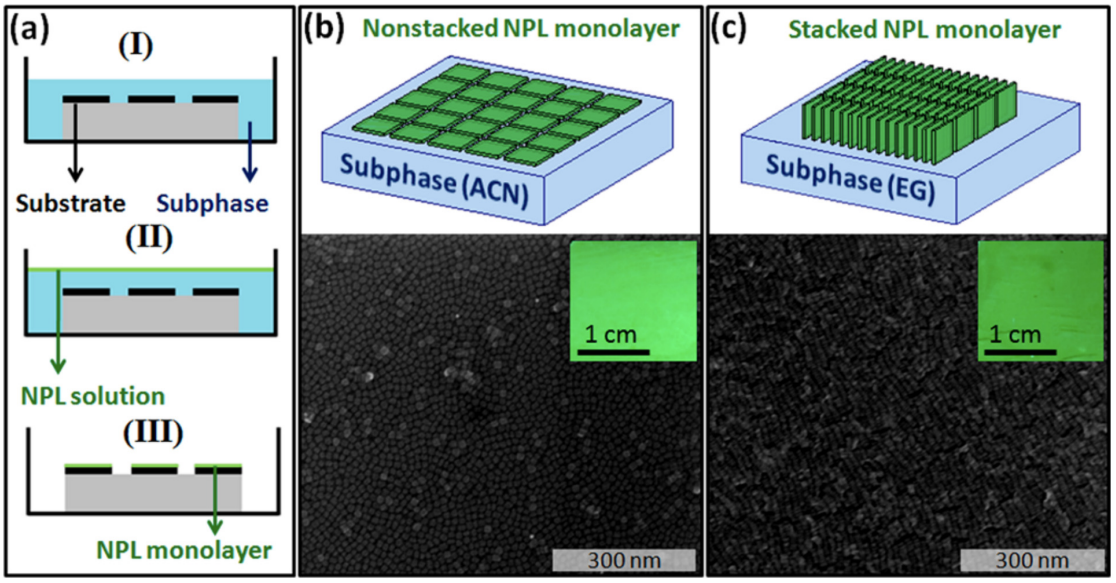

FIGURE 3.10: (a) Liquid-air interface self-assembly procedure: (I) Blank substrates are placed inside the subphase. (II) NPL solution is poured onto the subphase and is then allowed to dry. (III) The subphase is subsequently drained after the evaporation of the NPL solution. Finally, the residual subphase on the substrates is evaporated. NPL orientation on the liquid-air interface depends on the subphase. Schematic representation of NPL monolayers (b) on acetonitrile (ACN) and (c) on ethylene glycol (EG), along with SEM images of these films after being transferred to a solid substrate. The scale bars of the SEM images are 300 nm. ACN results in nonstacked selfassembly, whereas EG results in stack formation. Insets in the SEM images show real-color fluorescence images of the resulting monolayer assemblies on wafers of thermal oxide with scale bars of 1 cm. Reproduced with permission from [206]

Replicating the procedure was vary straightforward and produced comparable and repeatable results, and is shown on Figure 3.11.

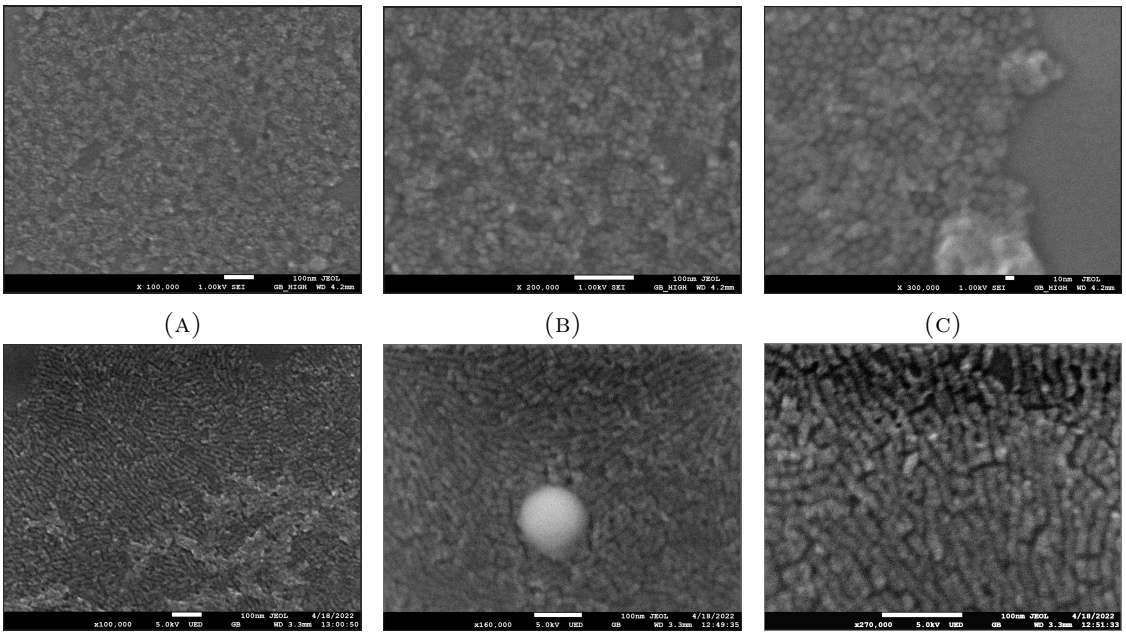

(A) (B) (C)

(D) (E) (F)

FIGURE 3.11: **A**, **B** and **C** SEM images of self-assembled CdSe NPLs assembled with ACN as the subphase, resulting in face down monolayers of NPLs. **D**, **E** and **F** SEM images of self-assembled CdSe NPLs assembled with EG as the subphase, resulting in edge-up monolayers of NPLs.

Unfortunately, as will be discussed in more detail in Chapter 4, Section 4.6.6, my antenna designs, compatible with such self-assembled monolayers on NPLs, selectively couple to emitters with effective dipole orientations perpendicular to the plane of the substrate ("out-of-plane"). Since NPLs effective dipole orientation is "in-plane" [205, 233, 234, 235], the face down self-assembled NPLs would have very weak coupling to the nanoantenna structure. This leaves only the edge-up NPL layers as possible candidates for coupling to the nanoantennas. This also has several issues: edge-up or "stacked" NPLs tend to have lower photoluminescence because of nonradiative decay [236]; also, since the lateral dimensions of the NPLs are on the order of tens of nanometers, edge-up NPLs would increase the distance between the antenna and the substrate, which, as shown in [93] and further discussed in Chapter 4 will decrease the maximum achievable fluorescence enhancement factor.

3.3.2.2 Quantum dot spin-coating

Figures from this section are published in [1].

Quantum dots are another common type of emitter that can be easily homogeneously distributed on a substrate. Because of their roughly spherical shape (i.e. no pronounced anisotropy as present in NPLs, usually only a single characteristic size parameter, "radius") [237, 238, 228], issues present in the NPL films, like orientation control for film quality and coupling to antennas, aren't present in quantum dot films. One can assume an almost homogeneous distribution of dipole orientations for a quantum dot film. Thus, a much simpler coating procedure, spin-coating, should be adequate to achieve a homogeneous film.

By varying quantum dot concentration in the solvent and spin-coating speed, I was able to achieve near-perfect monolayer coverage of a flat Silicon substrate. No special functionalization of either QDs or substrate for improved adhesion was required.

Near optimal spin-coating conditions were determined to be approximately 5 mg of QDs per ml in toluene, spin-coated at 2000 rpm for 1 minute. SEM images of resulting layer of QDs on glass and on a gold-coated substrate are shown on Figure 3.12a. and b., respectively. The quantum dots I used were CdSe/ZnS alloyed quantum dots synthesized following the protocols described in [239], for a emission peak centered at 650 nm.

For the purposes of coupling the quantum dot layer to my nanoantennas, as will be discussed in Chapter 4, the substrate that I needed to coat with quantum dots needed to be changed from a Silicon substrate, to a substrate covered with a thin Gold film. Because the growth of gold results in a relatively rough film consisting of gold nanoislands [240], spin-coating quantum dots on such a film results in a less than perfect layer, but, as will be shown later, sufficient to demonstrate coupling of quantum dots to nanoantennas and demonstrate strong fluorescence enhancement.

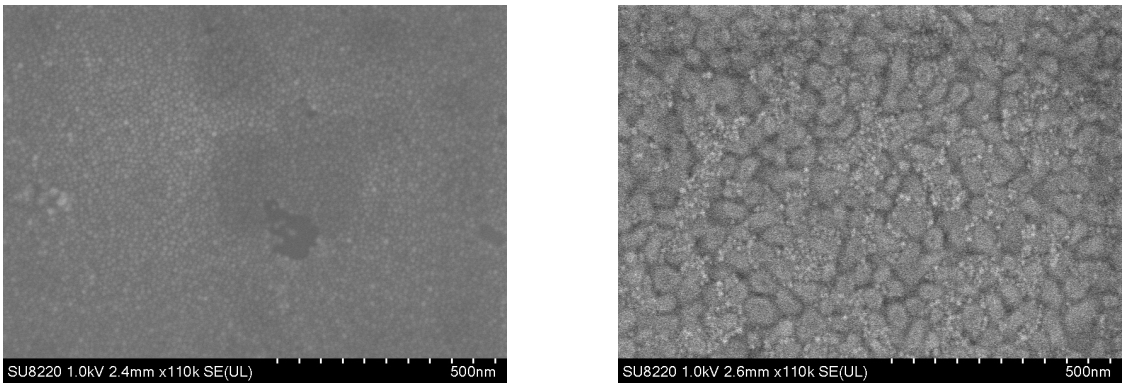

(A) (B)

FIGURE 3.12: **A** SEM image of near-monolayer of spin-coated quantum dots. **B** SEM image of quantum dots spin-coated with same conditions onto a gold-coated substrate.

3.4 Conclusions

Several methods of quantum emitter localization were explored: AFM manipulation of nanodiamonds with NV-centers, direct writing of emitters using EBL, printing of emitters using cytosurge AFM probes and creation of single photon emitters in hBN using FIB or E-beam.

The most successful method proved to be direct writing of emitters using EBL from HSQ resist, demonstrating good control of emitter position and demonstrating successful coupling of the written emitters to gold dimer antennas (see Fig. 3.6). Further development of the method could yield an effective technique for direct writing of quantum emitters. This would require quantification of the dependence of emitter density on e-beam dosage, repeatability of emitter fabrication, as well as a more detailed characterization of the emitters' optical characteristics.

The limiting factor of the method is the mask alignment accuracy — as was shown on Figure 3.5c, several alignment attempts were sometimes required to successfully align the HSQ cylinder with already existing antennas. The antenna structure from Chapter 2 already required two EBL alignment steps, and this method using EBL with another alignment step further increases complexity and exacerbates any misalignment errors. Thus this method of aligning emitters would have a very low yield of successful antennas with the equipment available to me, so I continued exploring alternative techniques.

Printing of quantum dots using a hollow AFM tip was successful in delivering quantum dots to nanoantennas, but did not display enough control over the deposited liquid volume to allow for any quantitative measurements — different droplets would have over a 10× difference in intensity.

Creation of emitting defects in hBN was unsuccessful in creating stable emitters that could be quantified, potentially because of a lack of understanding of the exact method of emitting defect formation.

AFM manipulation of nanodiamonds was discarded because of lack of suitable equipment and potential future issues with depositing the nanodiamonds deep in the nanoantenna structure.

The problem with all the explored methods of localizing quantum emitters is complexity — complex manipulations using AFM, EBL or FIB, which, on top of already complex fabrication procedures for hybrid nanoantennas, make the overall process to make a hybrid antenna and emitter system very laborious and low-yield. Ideally, one would want to minimize complexity as much as possible. In [132] the authors demonstrated an interesting concept — using the antenna structure itself as a mask to protect the emitting 2D-material below the antenna from the following etching process, leaving the final structure with emitting material only directly below the antenna, effectively localizing emitters without any precise alignment. This kind of self-localization would eliminate most of the complexity related to emitter localization, but required the development of a method for the distribution of quantum emitters in a homogeneous layer on a substrate for further antenna fabrication. Several methods were attempted — transfer of flakes of 2D materials with homogeneous emission onto target substrates, which was successful, but required the deposition of an additional protective layer before any other antenna fabrication could be carried out; and distribution of either NPLs or QDs via self-assembly methods onto target substrates. Both methods showed promise, but require a change in antenna design, since the original design discussed in Chapter 2, has its hot spot for emitter coupling inside the antenna structure, while the emitters would be located beneath the antenna.

In the next chapter, self-assembled QDs coupled to a hybrid nanoantenna design will be presented.

3.5 Methods

3.5.1 Fabrication

HSQ Cylinders were fabricated using the same methods described in Chapter 2, Section 2.8.2.

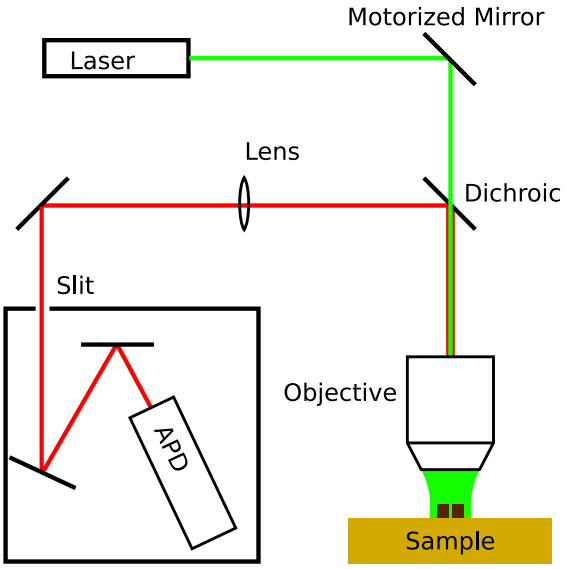

FIGURE 3.13: Schematic of photoluminescence mapping setup.

3.5.2 Characterization

3.5.2.1 Photoluminescence Mapping

For photoluminescence mapping measurements, a 532nm CW laser was used to excite PL. The pump laser was focused onto the sample substrate by a 100x 0.8NA objective lens, A 650nm band pass filter with a 50nm FWHM was used to cut off any pump laser light in the collection beam path. A motorized mirror before the objective was used to deflect the laser beam and scan the sample. Collected light was sent to an APD. Setup shown on Figure 3.13.

Chapter 4

Silicon Ring on Au Mirror

The material in this chapter is published as [1].

4.1 Introduction

In this chapter I propose and demonstrate single subwavelength hybrid dielectric-plasmonic optical nanoantennas coupled to localized quantum dot emitters that constitute efficient and bright unidirectional photon sources under optical pumping. To achieve this, I devised a silicon nanoring sitting on a metallic (gold) mirror with a 10 nm gap in between, where an assembly of quantum dots is embedded. Such a structure supports both gap mode and (radiative) antenna mode resonances. It is experimentally shown that the assembly of quantum dots localized within the nanogap can efficiently couple to these two kind of modes, the resonant gap modes and the antenna modes, for the dual purpose of enhancing the absorption of the optical pump by the emitters, and for out-coupling the light into the far-field with high directionality. Moreover, almost independent control of the resonance spectral positions is achieved by simple tuning of geometrical parameters such as the ring outer and inner diameters, which is not possible with other, simpler, particle-on-mirror nanoantennas. Using the proposed architecture, I obtain average fluorescence enhancement factors of the assembly of emitters up to 654× folds together with a high radiation efficiency, and a directional emission of the photoluminescence into a cone of ±17° in the direction normal to the sample plane.

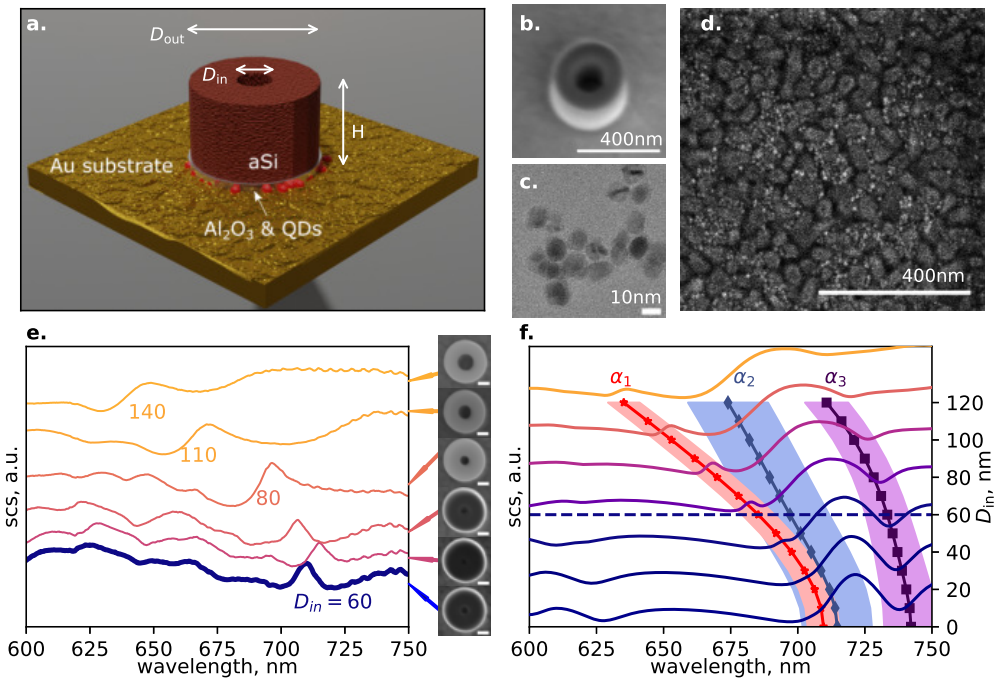

FIGURE 4.1: *Design and fabrication of hybrid dielectric-plasmonic nanoantennas.* **a.** Artist's impression of the aSi nanoring placed on a Au substrate, with a Al_2O_3 spacer layer containing the embedded QDs (represented by the red dots). **b.** Tilted SEM image of a typical fabricated sample. The scale bar represents 400 nm. **c.** TEM image of the CdSe/ZnS quantum dots. The scale bar represents 10 nm. **d.** SEM image of the Au substrate coated by a first layer of Al_2O_3 itself covered with spin-coated QDs. The scale bar represents 400 nm. **e.** Experimental scattering measurements for different nanoantennas with same $D_{\text{out}} = 380$ nm and $H = 230$ nm, but increasing D_{in} (from bottom to top). The insets show SEM images of the corresponding fabricated nanoantennas. The scattering for the case $D_{\text{in}} = 60$ nm (chosen to be discussed in the rest of this work and called "Antenna A"), is highlighted by a thicker line. The scale bars represent 100 nm. **f.** Simulated scattering cross-sections (lines, left axis) and calculated eigenwavelengths (real part λ'_α) of three resonant modes labelled α_1, α_2, α_3 (points, right axis) for different nanoantennas with same $D_{\text{out}} = 380$ nm and $H = 230$ nm, but increasing D_{in} from $D_i = 0$ to $D_i = 120$ nm (by steps of 20 nm for the former case, and by steps of 10 nm for the latter case, from bottom to top). The mode widths (determined as two times the imaginary part $2\lambda''_\alpha$) are also shown by the shaded areas. The lines joining the points are guide-to-the-eye, and the horizontal dashed line shows the case $D_i = 60$ nm (Antenna A).

4.2 Design and fabrication

The nanoantenna design, as shown schematically in Figure 4.1a, consists of an amorphous silicon (aSi) nanoring on a gold (Au) mirror substrate, with an alumina (Al_2O_3) spacer in between where the quantum emitters are embedded. Scanning

electron microscopy (SEM) images of our fabricated samples are shown in Figure 4.1b and as insets on Figure 4.1e. On one hand, this design is inspired by a hybrid dielectric-metal resonator proposed in [93], that supports "gap mode resonances" which are created by surface plasmon polaritons bouncing back and forth at the dielectric particle termination [241, 93]. Thus, the resonance wavelengths have a geometric origin and are essentially related to the diameter of the particle with a similar condition as for Fabry-Perot resonances [241, 93]. Moreover, since these gap modes are strongly confined inside the nanogap, they can be exploited to enhance the absorption of the quantum emitters, which is what we do in this work. On the other hand, silicon nanorings can present strong scattering properties, with geometrically tunable "antenna resonances" (also called "Mie resonances") that provide control over the scattering directionality, and potential ability to tailor the emission of electric or magnetic dipole emitters [173, 174, 176, 175]. In this work, we focus on the emission enhancement of electric dipole emitters by such antenna resonances.

We use CdSe/ZnS quantum dots (QDs) as quantum emitter model system. Transmission electron microscope image of the QDs is shown in Figure 4.1c, and we obtained a rather good homogeneous distribution of QDs obtained after spin-coating, as shown in Figure 4.1d. The QDs are chosen to have an emission peak centered around 650 nm [239]. Their emission and absorption spectra on top of a glass substrate are given in Section 4.6.2.

In order to separate the QDs from Au and to prevent quenching [65], a ≈ 3 nm layer of Al_2O_3 was first deposited, and after spin-coating the QDs, a second Al_2O_3 layer of same thickness was deposited to protect the QDs from the following CVD deposition of aSi (see Methods section). All the QDs which were not precisely located between the Au mirror and aSi nanoantenna were etched out; hence, we managed to create spatially self-aligned and localized QDs in a nanogap of $g \approx 10$ nm, without requiring any complex emitter manipulation or characterization, similar to what was previously reported [132]. Comparison of antenna and background photoluminescence is shown in Section 4.6.1. A fabrication process flow schematics can be found in Section 4.7.1.

Since the fabrication process exerts thermal and chemical stress that can potentially degrade the QDs [242], we characterized optically the QD layer at all steps of the fabrication process to quantify the changes in photoluminescence (PL) and

fluorescence lifetimes. We observed that the intensity of the QD PL is reduced by almost 98% after depositing the second layer of Al_2O_3, that is in the configuration $Au/Al_2O_3/QDs/Al_2O_3$ (under the same excitation power). Moreover, time-resolved PL experiment (see Methods section) revealed that this drop in PL is correlated with a reduction of the QDs lifetime from $\tau_0 = 5.00\,\text{ns}$ to $\tau_0 = 0.65\,\text{ns}$ (see Section 4.6.3). From these observations, we concluded that the QDs are degrading because of thermal stress during the ALD process [242] (see Methods section), which makes the quantum yield drop from $\text{QY}^0 = 0.2$ (that we take according to [239], and which matches our measured lifetime of $\tau_0 = 5.00\,\text{ns}$) to $\text{QY}^0 = 2.6 \times 10^{-3}$. Therefore, in the rest of this article, we choose to compare any PL enhancements when the aSi nanoantenna is present to the configuration $Au/Al_2O_3/QDs/Al_2O_3$ in which the QDs quantum yield is decreased to $\text{QY}^0 = 2.6 \times 10^{-3}$, and that we will call the "Reference" hereafter.

We designed and fabricated the aSi nanorings to have a fixed outer diameter of $D_{\text{out}} \approx 380\,\text{nm}$, chosen to support a gap mode resonance at around $\lambda_{\text{exc}} \approx 570\,\text{nm}$ (see Section 4.6.4), in order to enhance locally the laser (pump) intensity at that excitation wavelength. The height of the nanoring was fixed to $H \approx 230\,\text{nm}$, chosen to support an antenna mode resonance around the emission wavelength of the QDs $\lambda_{\text{em}} \approx 650\,\text{nm}$ that strongly radiates in the upward direction (for out-of-plane emission). We fabricated different samples with approximately same outer diameter and height, but with different inner diameters D_{in} (ring hole) varying between $\approx 60\,\text{nm}$ to $\approx 140\,\text{nm}$, in order to tune (shift) the antenna mode resonance (SEM images of the antennas are shown as insets on Figure 4.1e). As we will see, because of the presence of these two classes of modes — the gap modes, which are mostly sensitive to D_{out} of the ring, and the antenna modes that are strongly sensitive to D_{in} — we are able to almost independently control the spectral positions of both types of resonances, allowing us to adapt the design to match the excitation and emission wavelengths of the pump and QDs, respectively.

The fabricated nanoantennas were first characterized with dark-field scattering measurements (see Methods section). Experimental scattering spectra are shown in Figure 4.1e and reveal that the scattering features are blue-shifted , with increasing D_{in}. This is in fair agreement with the scattering cross-section simulations spectra (see Methods section) shown in Figure 4.1f. On the other hand, when increasing

D_{out} and fixing all other quantities, one observes a red-shift of the resonances (Section 4.6.5).

We next computed the resonant optical modes $\mathbf{E}_\alpha$ of the system as well as their complex eigenwavelengths $\lambda_\alpha = \lambda'_\alpha + \mathrm{i}\,\lambda''_\alpha$, with α labelling the mode, using quasi-normal mode (QNM) calculations [243] (see Methods section). We identified that the main features appearing in the scattering spectra are associated to the excitation of three particular antenna modes, labelled α_1, α_2 and α_3 in Figure 4.1f.

The mode α_1 has a Q-factors of about $Q \sim 30$, which is higher than for α_2 and α_3 (with $Q \sim 10$ and $Q \sim 20$, respectively), as can be seen from the sharper features in the scattering spectra. Moreover, its spectral position is more sensitive to D_{in} than the two other QNMs, allowing for a higher degree of tunability. For these reasons, we choose the antenna mode α_1 for the purpose of enhancing the emission of the QDs. The field profile of the mode α_1, shown in Section 4.6.7, reveals that most of the electric field is located inside the hole of the nanoring, which explains why this mode is highly sensitive to the parameter D_{in}.

Moreover, a comparison with the case of a standalone nanoring shows that the presence of the metallic mirror contributes to more than doubling the Q-factor of the mode α_1, in addition to slightly blue-shifting its spectral position (see Section 4.6.6, Figure 4.11). Even more importantly, we found that, while for the standalone nanoring it is mostly the *in-plane* dipoles that couple to this mode, and only within a small area (located below the hole of the nanoring), the presence of the mirror makes the *out-of-plane* dipoles to mostly couple to this mode, within a much larger area (that forms a circular "band" surrounding the hole of the nanoring), and with much higher coupling strength (see Section 4.6.6, Figure 4.12). In practice, since it is very challenging to control the position and orientation of the emitters precisely, the PL signal coming from the assembly of emitters is averaged out over emitters spatially distributed over the nanoantenna area with random dipole orientations. Therefore, a nanoring on top of a metallic mirror is expected to give a significantly higher PL enhancement compared to the case of a standalone nanoantenna, due to higher coupling strength and the more spatially "extended" coupling.

4.3 Experimental Characterization

In the following, we present the results obtained for the selected nanoantenna case having $D_{\text{in}} = 60\,\text{nm}$, which we call "Antenna A" hereafter, for which we obtained the highest total fluorescence enhancement. To characterize the total fluorescence enhancement of the QDs with the nanoantenna compared to the Reference situation (in the absence of nanoantenna, denoted by the superscript "0" hereafter), we use the well established fact that, in the low excitation regime, the fluorescence enhancement per emitter (located at $\mathbf{r}$) is proportional to the gains in excitation rate, collection efficiency and quantum yield [14, 10, 41]:

$$\text{EF}_{\text{th}}(\mathbf{r}) = \frac{\gamma_{\text{exc}}(\mathbf{r})}{\gamma_{\text{exc}}^0} \frac{\text{D}_{\text{em}}(\mathbf{r})}{\text{D}_{\text{em}}^0} \frac{\text{QY}(\mathbf{r})}{\text{QY}^0} \tag{4.1}$$

The first ratio represents the excitation enhancement of the QDs, which corresponds to the excitation rate γ_{exc}, and is directly proportional to the local enhancement of the pump intensity at the position of the emitter $\mathbf{r}$. This quantity depends therefore on the wavelength used for the pump laser λ_{exc}. The second ratio represents the collection efficiency enhancement, which corresponds to enhancement of the collected signal into a given numerical aperture (NA). It thus depends on the collection NA, denoted by NA_{col}, and also on the wavelength of fluorescent emission λ_{em}. Finally, the last ratio represents the enhancement of the emitter quantum yield (QY), the QY quantifying the radiation efficiency (i.e. the probability that the excitation of the emitter actually results in the emission of a photon in the far field), which also depends on the emission wavelength λ_{em}. More specifically, in the Reference situation, QY^0 reads $\text{QY}^0 = \gamma_{\text{r}}^0/(\gamma_{\text{r}}^0 + \gamma_{\text{nr}}^0)$, with γ_{r}^0 and γ_{nr}^0 being the radiative and non-radiative decay rates of the QDs, respectively. With the introduction of the nanoantenna, the QY is modified as $\text{QY}(\mathbf{r}) = \gamma_{\text{r}}(\mathbf{r})/[\gamma_{\text{r}}(\mathbf{r}) + \gamma_{\text{nr}}^0 + \gamma_{\text{abs}}(\mathbf{r})]$, with $\gamma_{\text{r}}(\mathbf{r})$ is the new radiative decay rate modified in the presence of the nanoantenna, $\gamma_{\text{abs}}(\mathbf{r})$ is a new nonradiative decay channel that takes into account the absorption by the nanoantenna, and γ_{nr}^0 is assumed to remain unaffected by the introduction of the nanoantenna [244].

Note that all of these quantities are defined for a single electric dipole emitter with a given position $\mathbf{r}$ and also having a fixed orientation of its dipole moment along the unit vector $\mathbf{u}$, but for the sake of readability, we omit the dependence on the parameter $\mathbf{u}$ in the above quantities. Also, it is interesting to note from

Equation (4.1) that the total fluorescence enhancement $\mathrm{EF_{th}}$ depends on the type of emitter used in the Reference situation through QY^0, and is thus not an absolute figure-of-merit to characterize the performance of a given antenna.

After introducing the above quantities, we now use the fact that $\mathrm{QY}/\mathrm{QY}^0 = [\gamma_\mathrm{r}(\mathbf{r})/\gamma_\mathrm{r}^0][\tau(\mathbf{r})/\tau^0]$, where we further introduce the fluorescence lifetimes defined as $\tau(\mathbf{r}) \equiv 1/[\gamma_\mathrm{r}(\mathbf{r}) + \gamma_\mathrm{nr}^0 + \gamma_\mathrm{abs}(\mathbf{r})]$ and $\tau^0 \equiv 1/(\gamma_\mathrm{r}^0 + \gamma_\mathrm{nr}^0)$ in the nanoantenna and Reference situations, respectively, to recast Equation (4.1) into the following form, which will be more convenient for our purpose of characterizing the underlying mechanisms at play in our nanoantenna [14]:

$$\mathrm{EF_{th}}(\mathbf{r}) = \frac{\eta_\mathrm{exc}(\mathbf{r}, \lambda_\mathrm{exc})\, \eta_\mathrm{em}(\mathbf{r}, \lambda_\mathrm{em}, \mathrm{NA_{col}})}{\eta_\mathrm{tot}(\mathbf{r}, \lambda_\mathrm{em})} \tag{4.2}$$

In Equation (4.2), we defined the quantities $\eta_\mathrm{exc} \equiv \gamma_\mathrm{exc}/\gamma_\mathrm{exc}^0$ and $\eta_\mathrm{em} \equiv (\mathrm{D_{em}}/\mathrm{D_{em}^0})(\gamma_\mathrm{r}/\gamma_\mathrm{r}^0)$, which quantify the enhancements in excitation and emission, respectively, and also the quantity $\eta_\mathrm{tot} \equiv \tau_0/\tau$, which quantifies the fluorescence lifetime modification (or equivalently the total decay rate enhancement $\eta_\mathrm{tot} = \gamma_\mathrm{tot}/\gamma_\mathrm{tot}^0$ with $\gamma_\mathrm{tot} = \tau^{-1}$ and $\gamma_\mathrm{tot}^0 = (\tau^0)^{-1}$ — also known as the "Purcell factor"), and we made the dependence in terms of λ_exc, λ_em and $\mathrm{NA_{col}}$ of the terms η_exc, η_em and η_tot explicit. We emphasize that, through Equation (4.2), the total fluorescent enhancement is related to but different from the Purcell factor.

4.3.1 Excitation enhancement and gap resonance

Experimentally, we first optimized the excitation wavelength λ_exc to maximize the excitation enhancement η_exc. For that, we recorded the PL signal as we varied the pump wavelength λ_exc from 488 to 588 nm, while maintaining a constant pump power, by collecting the light radiated into air using an objective lens with $\mathrm{NA_{col}} = 0.9$. Even though the QDs absorb shorter wavelength light more efficiently (as shown in Section 4.7), optimal pumping conditions for PL enhancement in the case of the nanoantenna were found to be at approximately $\lambda_\mathrm{exc} = 570$ nm, as shown in Figs 4.2a. In all the subsequent measurements, we therefore fix the pump wavelength at $\lambda_\mathrm{exc} = 570$ nm.

We confirmed by numerical simulations (see Methods section) the presence of a local maximum for the excitation enhancement around 583 nm, shown in Figs 4.2b.

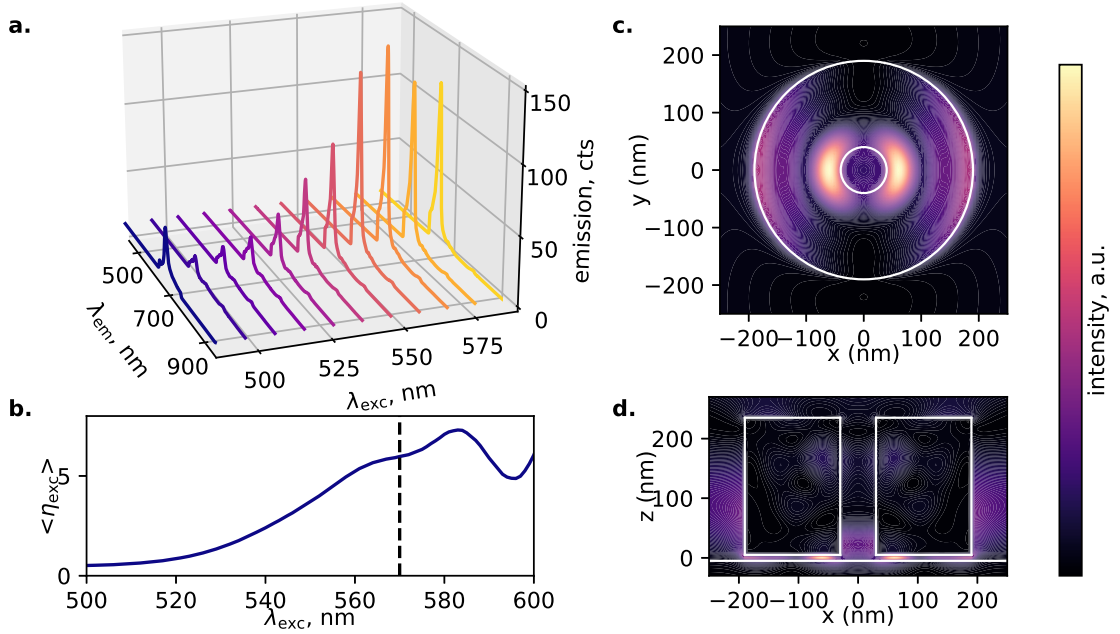

FIGURE 4.2: *Excitation enhancement for Antenna A and comparison with simulations.* **a.** Experimental PL intensity spectra in counts (cts) from Antenna A, showing their dependence on the pump excitation wavelength λ_{exc} having a linear polarization and normal incidence. The maximum emission peak is obtained for $\lambda_{\text{exc}} = 570\,\text{nm}$. **b.** Simulated average excitation enhancement $\langle\eta_{\text{exc}}\rangle$ for Antenna A as a function of the excitation wavelength λ_{exc}, calculated as the intensity enhancement of the pump electric field in the nanogap, according to Equation (4.11) (see Methods section). The maximum intensity enhancement is obtained for $\lambda_{\text{exc}} = 583\,\text{nm}$ in the simulation. The vertical dashed line denotes the excitation wavelength at $\lambda_{\text{exc}} = 570\,\text{nm}$. **c.** and **d.** Simulated electric field intensity distribution at $\lambda_{\text{exc}} = 570\,\text{nm}$ in the horizontal cross-section passing through the middle of the nanogap and in the vertical cross-section passing through the middle of the nanoantenna, respectively. In the simulations, the excitation source has its electric field linearly polarized along the x-axis, and comes at normal incidence, like in the experiment.

We obtain that the theoretical excitation enhancement factor $\langle\eta_{\text{exc}}\rangle$ — the bracket denoting position and orientation averaging of the QDs — is $\langle\eta_{\text{exc}}\rangle = 7.3$ at the pump wavelength $\lambda_{\text{exc}} = 583\,\text{nm}$. We also show the field intensity in the horizontal cross-section located in the middle of the gap, and in vertical cross-section passing through the center of the nanoantenna, in Figs 4.2c, d, respectively, which reveal that most of the intensity is located in "hot spots" formed within the nanogap. We also checked in simulations that the field profile of this gap mode matches the one expected in theory for the gap mode resonance of symmetry $(n = 3, m = 1)$ (see Section 4.6.4 and Section 4.6.7), for which the nanoantenna was designed, as mentioned earlier.

Finally, note that the intensity distribution of this gap mode (exploited for *absorption* enhancement), is mostly located around the hole of the nanoring, and thus presents a rather good spatial overlap with the area within which the mostly coupled emitters to the antenna mode (exploited for *emission* enhancement) are located, as discussed earlier.

4.3.2 Emission enhancement and antenna resonance

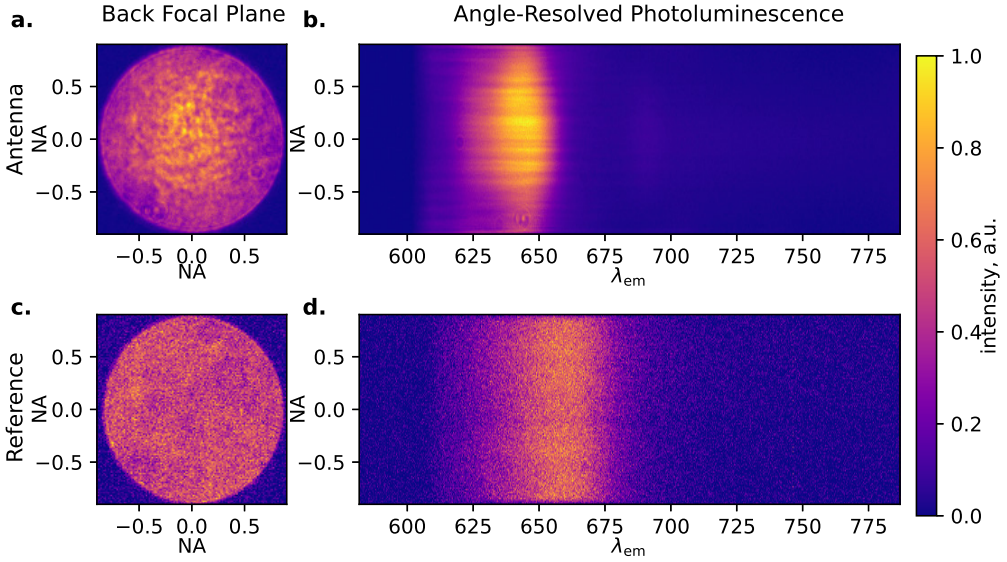

FIGURE 4.3: *Brightness enhancement for Antenna A and comparison with Reference.* **a.** Back focal plane image of the emission PL of Antenna A taken with a bandpass filter centered around $\lambda_{em} = 650\,\text{nm}$ with a FWHM of 30 nm and using a high-NA collection objective lens of $NA_{col} = 0.9$. **b.** Angle-resolved PL spectra of Antenna A using the same collection objective lens and projecting the image onto a spectrometer. **c.** and **d.** Back focal plane image and angle-resolved PL spectra of the Reference situation (absence of nanoantenna), respectively.

We next measured the angle-resolved PL spectra of the nanoantennas, using back focal plane imaging technique (see Methods section), using the same objective lens with $NA_{col} = 0.9$. We show in Figure 4.3a and b the back-focal-plane and angle-resolved PL of Antenna A, respectively. The corresponding images in Reference situation are shown in Figure 4.3c and d. One can see that the nanoantenna situation looks brighter and present more directivity than the Reference situation.

Since our nanoantennas are designed for emission in the upward direction (out-of-plane), and in order to quantify the emission enhancement in the upward direction, we choose to integrate the angle-resolved PL of Figure 4.3 over a collection $NA_{col} =$

0.3, which corresponds approximately to ±17°. The corresponding PL spectra is shown in Figure 4.4a (blue line), together with the Reference PL (red line). In order to deduce the experimental total fluorescence enhancement from these PL spectra, we deconvoluted the PL signal of the nanoantenna with the Reference PL, according to the formula:

$$\langle \mathrm{EF}_{\mathrm{exp}} \rangle = \frac{I}{I_0} \frac{\mathcal{A}_0}{\mathcal{A}} \tag{4.3}$$

where I (resp. I_0) is the PL intensity collected in the nanoantenna situation (resp. in the Reference situation) — as shown in Figure 4.4a — and $\mathcal{A}$ (resp. $\mathcal{A}_0$) is the area corresponding to the ring horizontal cross-section that reads $\mathcal{A} = \pi(D_{\mathrm{out}}/2)^2$ with $D_{\mathrm{out}} = 380\,\mathrm{nm}$ where the QDs are located (resp. the area of the excitation spot $\mathcal{A}_0 = \pi(D_{\mathrm{spot}}/2)^2$ which is estimated to $D_{\mathrm{spot}} \simeq 1.37\,\mu\mathrm{m}$; Section 4.6.8).

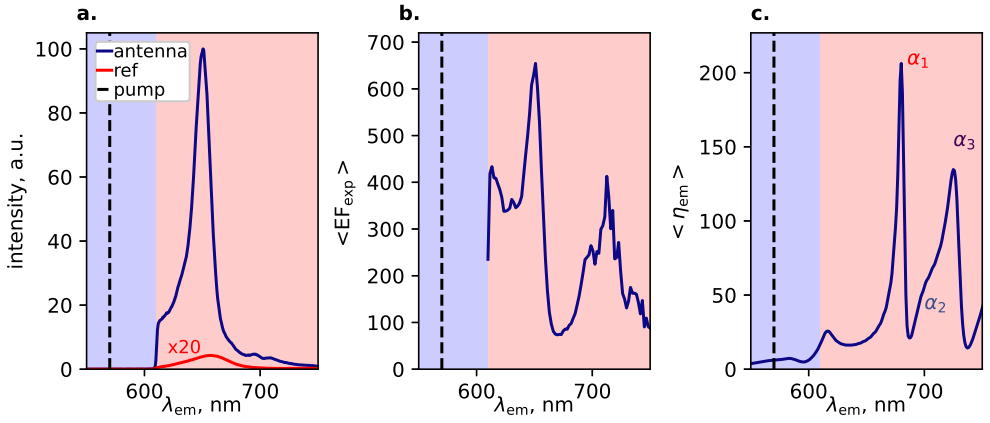

FIGURE 4.4: *Emission enhancement for Antenna A and comparison with simulations.* **a.** Experimental emission PL spectra for Antenna A (blue curve) and Reference (red curve), integrated over $\mathrm{NA}_{\mathrm{col}} = 0.9$. **b.** Emission PL enhancement $\langle \mathrm{EF}_{\mathrm{exp}} \rangle$ spectra obtained after deconvoluting the PL from Antenna A from the Reference PL, according to Equation (4.3), and restricting the integration over $\mathrm{NA}_{\mathrm{col}} = 0.3$ to capture the directional emission only. A 610 nm long pass filter was used to cut off any pump laser light in the collection beam path (denoted by the blue area in the plots which are filtered in the collection channel while the red area reaches the spectrometer). **c.** Simulated emission enhancement $\langle \eta_{\mathrm{em}} \rangle$ for Antenna A in the upward direction (see Methods section). In all plots, the vertical dashed line indicates the pump excitation wavelength $\lambda_{\mathrm{exc}} = 570\,\mathrm{nm}$.

The obtained experimental total fluorescence enhancement spectra is plotted in Figure 4.4b. One can see one main peak around the emission wavelength of the QDs $\lambda_{\mathrm{em}} = 652\,\mathrm{nm}$, for which we get a maximum total fluorescence enhancement factor of $\langle \mathrm{EF}_{\mathrm{exp}} \rangle = 654$ and also a secondary peak at 717 nm.

We corroborated these experimental total fluorescence enhancement spectra with numerical simulations (see Methods section). We computed in Figure 4.4c the emission enhancement $< \eta_{em} >$ in the upward direction (corresponding to $NA_{col} = 0$), because it corresponds to the direction of maximum directivity, and the bracket denotes once again position and orientation averaging of the QDs. One can see a good qualitative agreement with the experiment, with also the presence of two main peaks at $\lambda_{em} = 680\,nm$ and $\lambda_{em} = 725\,nm$. The shift of the resonances in experiment compared to simulation can be attributed to size variations in the height and outer diameter of the ring (even though we tried to fabricate all samples with these parameters being fixed, slight variations are unavoidable). The maximum emission enhancement at the main peak at $\lambda_{em} = 680\,nm$ is $\langle \eta_{em} \rangle = 206.2$.

Moreover, from the previous mode analysis shown in Figure 4.1f, we identify the two resonances at 680 nm and 725 nm with the antenna modes α_1 and α_3, respectively, as highlighted in Figure 4.4c. One can even see a weaker third resonance around 700 nm, which we identify with the antenna mode α_2 from Figure 4.1f, as highlighted in Figure 4.4c.

Finally, we obtained the experimental radiation patterns of the nanoantenna from the angle-resolved PL of Figure 4.3, at the emission wavelengths $\lambda_{em} = 652\,nm$ and $\lambda_{em} = 717\,nm$. Their radiation patterns are presented in Figure 4.5a and b, respectively (dark lines). The radiation pattern of the Reference situation is also shown (light blue lines). One can clearly see that each antenna resonance reshapes the emission into a main lobe oriented in the upward direction. The collection efficiency enhancement at $\lambda_{em} = 652\,nm$ is estimated to be $< D_{em}/D^0_{em} >= 1.43$ in the collection NA $NA_{col} = 0.3$ (see Equation (4.12) in Methods section for the formula used).

We also computed the theoretical radiation patterns (see Methods section) at the two main resonances exhibited in the simulated emission enhancement spectrum. Figure 4.5c and d display the simulated radiation patterns at the resonances 680 nm and 725 nm, respectively (dark lines). The simulated reference situation is also shown (light blue lines). One can see a good qualitative agreement between experiment and simulation, showing strong out-of-plane directivity. We calculated from these simulation results a collection efficiency enhancement at $\lambda_{em} = 680\,nm$ of $< D_{em}/D^0_{em} >= 1.31$ in the normal direction (see Methods section), from which together with the previously calculated maximum emission enhancement, we deduced

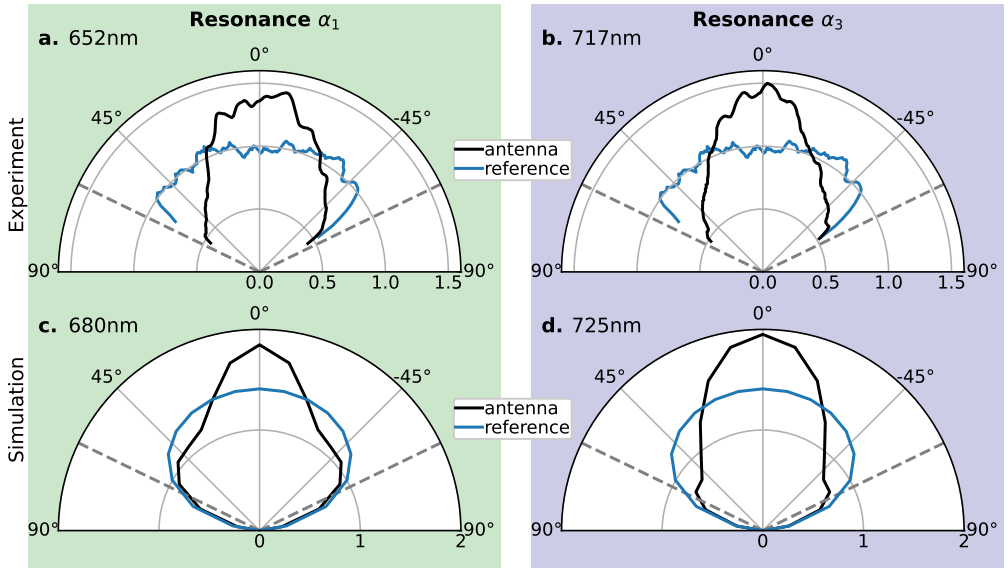

FIGURE 4.5: *Directional enhancement for Antenna A and comparison with simulations.* **a.** and **b.** Experimental radiation angular patterns for Antenna A (dark curves) at the two peaks of the PL enhancement $\langle \mathrm{EF}_{\mathrm{exp}} \rangle$ of Figure 4.4b, located at $\lambda_{\mathrm{em}} = 652\,\mathrm{nm}$ and $\lambda_{\mathrm{em}} = 717\,\mathrm{nm}$, respectively. The Reference case at $\lambda_{\mathrm{em}} = 650\,\mathrm{nm}$ is also shown (light blue curves). Grey dashed lines show the maximum collection angle corresponding to $\theta = 64.2°$. **c.** and **d.** Simulated radiation angular patterns for Antenna A (dark curves) at the two peaks of the PL enhancement $\langle \eta_{\mathrm{em}} \rangle$ of Figure 4.4c, located at $\lambda_{\mathrm{em}} = 680\,\mathrm{nm}$ and $\lambda_{\mathrm{em}} = 725\,\mathrm{nm}$, respectively. The Reference case at $\lambda_{\mathrm{em}} = 650\,\mathrm{nm}$ is also shown (light blue curves).

from Equation (4.2) the radiative decay rate enhancement to be $\langle \gamma_{\mathrm{r}}/\gamma_{\mathrm{r}}^{0} \rangle = 156.2$ at $\lambda_{\mathrm{em}} = 680\,\mathrm{nm}$.

4.4 Results and Discussion

In order to account more quantitatively for the experimental total fluorescence enhancement, and to interpret the main physical mechanisms involved based on Equation (4.2), it remains to determine the average lifetime reduction term $\langle \eta_{\mathrm{tot}} \rangle = \tau^{0}/\tau$. Since it is usually tricky to obtain this quantity theoretically [245], as it also depends on experimental input parameters such as the intrinsic non-radiative decay rate of the emitters γ_{nr}^{0}, we choose to use the experimentally obtained value from the measured lifetimes with a time-resolved PL setup (see Methods section). After fitting the experimental data (Section 4.6.9, Figure 4.17), we found a total decay rate enhancement or lifetime reduction of $\langle \eta_{\mathrm{tot}} \rangle = 1.79$, which is a very modest

value of Purcell factor, but is due to a certain extend to the very small value of the quantum yield of our emitters $QY^0 = 2.6 \times 10^{-3}$, and hence is not entirely characteristic of the nanoantenna. Note that all other terms in Equation (4.2) calculated theoretically are entirely characteristic of the nanoantenna and do not depend on the type of emitter, which is *not* the case for the term $\langle \eta_{\text{tot}} \rangle$.

By then applying Equation (4.2), and only using the experimentally measured lifetime reduction $\langle \eta_{\text{tot}} \rangle = 1.79$ to feed the theoretical formula, the other gains $< \eta_{\text{exc}} >= 7.3$ and $< \eta_{\text{em}} >= 206.2$ being all computed independently with full-wave simulations, we obtain a theoretical total fluorescence enhancement factor of $\langle \text{EF} \rangle_{\text{th}} = 841$ (corresponding to a collection in the upward direction), which is slightly higher than the experimentally measured one $\langle \text{EF} \rangle_{\text{exp}} = 654$ (for a collection NA of $\text{NA}_{\text{col}} = 0.3$ in the upward direction), but in good qualitative agreement. One can infer from this analysis that the emission enhancement $< \eta_{\text{em}} >$ — which we recall is the product of the collection efficiency and radiative decay rate enhancements — is the main mechanism responsible for the total fluorescence enhancement observed here, with also a smaller but non-negligible contribution of the absorption enhancement.

We also analyze in Section 4.6.9 the results obtained for two other nanoantennas, called Antenna B and C, having identical outer diameters and heights as Antenna A whose results were presented here, but larger inner diameters, $D_{\text{in}} = 80\,\text{nm}$ and $D_{\text{in}} = 110\,\text{nm}$, respectively. We found similarly good qualitative agreements between experiment and theory, by again only feeding the theoretical formula of Equation (4.2) with the experimentally measured lifetime reduction for $\langle \eta_{\text{tot}} \rangle$. Moreover, this comparative study between Antennas A, B and C highlights that one can tune (blue-shift) the resonance exploited for emission by varying (increasing) D_{in} with respect to the resonance exploited for absorption, as already anticipated from the mode study in Figure 4.1f.

4.5 Conclusion

In this work, we experimentally demonstrated an efficient and multi-resonance silicon nanoring on gold mirror nanoantenna coupled to localized quantum dots in a nanogap of $\sim 10\,\text{nm}$, which transformed very poor emitters into bright and

directional sources. A total fluorescence enhancement factor of 654× was measured, coming from different mechanisms that contributed to increase the brightness of our Antenna. Firstly, the nanoring antenna support several resonances designed to have strong scattering properties, that increase the radiative rates of emitters and improve the directionality in the upward direction. Moreover, the resonance wavelengths can be tuned using the ring *inner diameter* to match with the emission wavelength of the emitters. This is not the case for most other particle-on-mirror studies[10, 47, 12, 48, 88], where the particle has mainly one degree of freedom (the nanoparticle size), giving very limited capability to tune the resonant responses of the whole system.

Secondly, the metallic mirror creates a nanogap that supports "gap" modes[241, 93], whose resonance wavelength mostly depends on the ring *outer diameter* and therefore can be easily tuned using this parameter, in an almost independent way from the resonances exploited for the emission enhancement. These were used to create intensity "hot spots" in the nanogap, leading to an overall gain in the excitation efficiency of the QDs.

Among the improvements that can be carried out on these types of nanoantennas, we would like to mention a few here. First of all, there is a need to pay attention to ensure that the QDs are protected and not degraded by the fabrication process, as reported in this work and in Ref. [246], in order to guarantee higher quantum efficiencies. Secondly, by exploiting lower order gap mode resonances, one could increase the excitation enhancement (by a factor 4 for the second harmonics according to our simulations — not shown here), to potentially bring the total fluorescence to 3 orders of magnitude enhancement, figures reported so far in all-plasmonics nanopatch antennas. It was not possible in this work because the second harmonics was too near to be well separated spectrally from the emission of the QDs, and this is why we exploited the third harmonics, which provided more modest excitation enhancement.

The experimental demonstration provided in this paper confirms the relevance of nanorings in hybrid dielectric-plasmonic nanostructures as highly tunable nanoantennas with subwavelength size, to create efficient, bright and directional photon sources in the visible spectral range, that can be of foremost importance for the next-generation of light-emitting devices.

4.6 Supporting Data

4.6.1 Photoluminescence of antenna compared to background photoluminescence

Figure 4.6 shows the photoluminescence spectrum of an Antenna compared the photoluminescence spectrum of the plain substrate after all fabrication steps, showing that quantum dots were etched away everywhere except directly beneath the antennas.

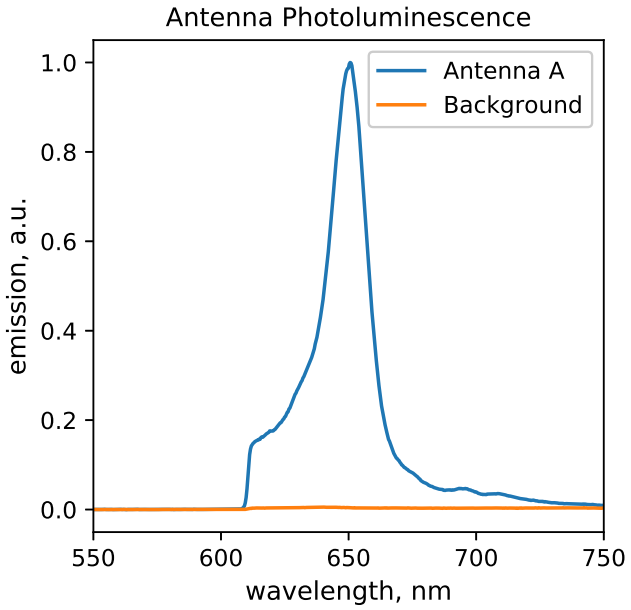

FIGURE 4.6: Antenna A PL spectrum compared to the background PL spectrum of the sample substrate, showing very strong emission of QDs coupled to the antenna above them. Very low background PL from areas not protected by antennas, confirming that all the QDs not protected by antennas were etched away.

4.6.2 Quantum dot emission and absorption spectra

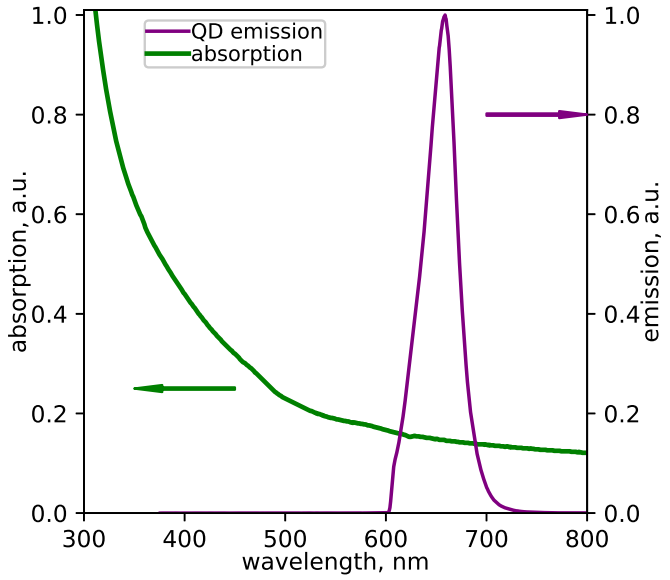

FIGURE 4.7: **e.** Absorption (green) and emission (purple) spectra of the CdSe/ZnS quantum dots used. Pump laser wavelength was 568 nm and a 610 nm long pass filter was used to cut off any pump laser light in the collection beam path.

4.6.3 Lifetime and PL measurements during fabrication process

Time-resolved PL decay shown in Figure 4.8 was fit by a bi-exponential function using reconvolution [247]. Fitting parameters are shown in Table 4.1. For all measured samples, the time-resolved decay showed two characteristic decay rates. For the case of quantum dots on a substrate, this is commonly interpreted as quantum dots with different orientations exhibiting different decay rates because of the substrate interactions [48].

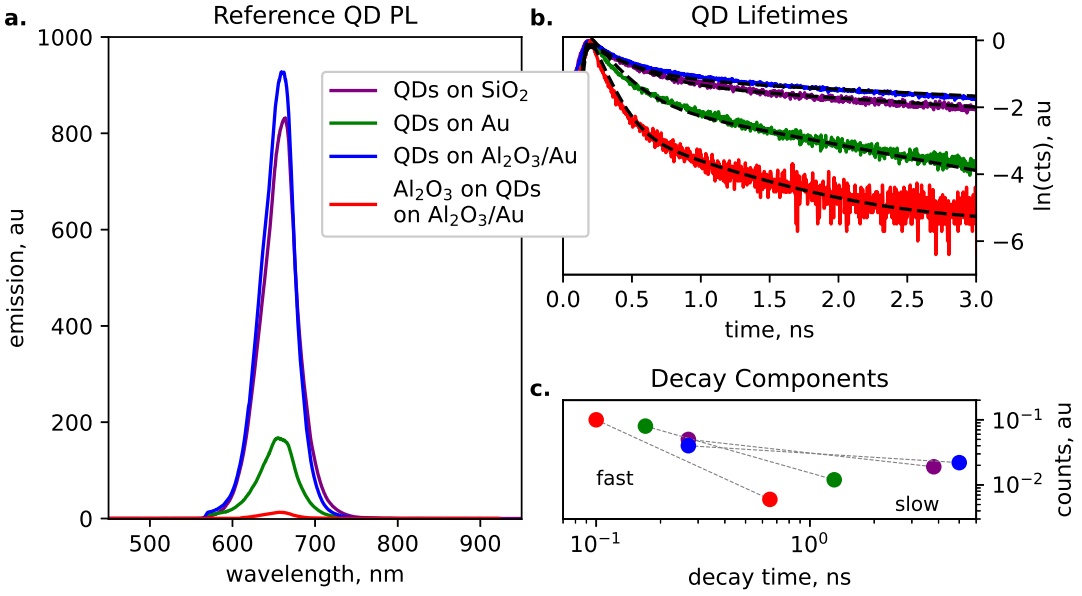

FIGURE 4.8: Photoluminescence (**a.**), lifetimes (**b.**) and fit decay components (**c.**) of reference quantum dots. Purple lines - quantum dots on SiO_2. Green lines - quantum dots directly on Au mirror, with noticeable quenching. Blue lines - quantum dots on Au mirror but with Al_2O_3 spacer separating them from the gold, which completely stops quenching. Red lines - damaged quantum dots after second Al_2O_3 deposition.

TABLE 4.1: Amplitude (a_1, a_2) and decay (τ_1, τ_2) components of the bi-exponential fitting used to the experimental lifetime measurements.

	a_1, a.u.	τ_1, ns	a_2, a.u.	τ_2, ns
QDs on SiO_2	0.05	0.27	0.019	3.80
QDs on Au	0.08	0.17	0.012	1.30
QDs on Al_2O_3/Au	0.04	0.27	0.022	5.00
Al_2O_3 on QDs on Al_2O_3/Au	0.10	0.10	0.006	0.65

4.6.4 Gap mode resonance

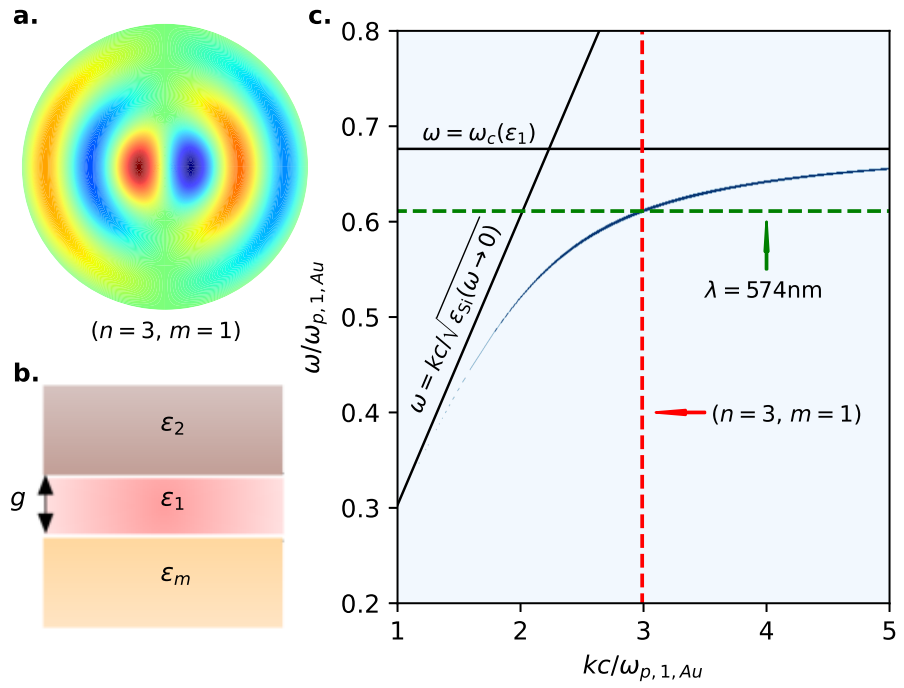

FIGURE 4.9: **a.** Spatial distribution of the mode of a circular resonator of symmetry $(n = 3, m = 1)$, calculated from Equation (4.4). Redder colors denote positive values, and bluer color negative ones. **b.** Schematic of the metal/dielectric 1/dielectric 2 configuration. **c.** Multilayer dispersion relation given by Equation (4.5) for a nanogap of thickness $g = 10\,\text{nm}$ and permittivity $\varepsilon_1 = 1.77^2$ sandwiched between an aSi semi-infinite covering layer of permittivity $\varepsilon_2 = \varepsilon_{\text{Si}}(\omega)$ given below without losses (i.e. $\gamma_{\text{Si}} = 0$) and a semi-infinite gold mirror whose dispersive permittivity ε_m is the one given below without losses (i.e. $\gamma_{1,\text{Au}} = 0$ and $\gamma_{2,\text{Au}} = 0$). The oblique dark line corresponds to the light cone in a homogeneous aSi medium $\omega = kc/\sqrt{\varepsilon_{\text{Si}}(\omega \to 0)}$ with $\sqrt{\varepsilon_{\text{Si}}(\omega \to 0)} = 3.3$. The horizontal black line corresponds to the cutoff frequency $\omega_c(\varepsilon_1)$ obtained as the zero of the standard dispersion relation $k = \omega/c\sqrt{\varepsilon_1\varepsilon_m/(\varepsilon_1 + \varepsilon_m)}$, that is by solving: $\varepsilon_1 + \varepsilon_m(\omega_c) = 0$.

It is not very convenient to identify the gap modes using the QNM formalism because in this spectral region (around and below 600 nm), the number of modes is very large and they are not spectrally well separated, which makes their analysis quite tedious. Instead, we use a more intuitive analytical approach to find the modes, based on geometrical considerations only [241, 93].

As mentioned in [93], the gap resonances of our system can be understood as "the surface plasmon of a planar multilayer metal-dielectric system restricted to specific quantized wavevectors". The cylindrical symmetry of our system implies that

resonances can be labeled with indices (n, m), enumerating field variations in the radial and azimuthal directions, respectively. The wavevectors k_{nm} are "quantized" due to the geometry of the above nanoantenna, which reflects the surface plasmon at its boundary, similarly to the modes of a Fabry-Perot cavity.

The gap modes can be modelled as the modes of a two dimensional circular resonator, which are found by solving the wave equation in polar coordinates (r, ϕ) — which becomes a Bessel's equation — with Dirichlet boundary conditions [248]. The solutions of this wave equation take the form [248]:

$$E(r, \phi, t) = A \cdot J_m(kr) \cdot \cos(m\phi) \cdot \mathrm{e}^{-\mathrm{i}\omega t} \tag{4.4}$$

where A is the amplitude of the mode, k is the wavevector, and m is the azimuthal number. Due to the Dirichlet boundary conditions, the wavevector is quantized according to: $k_{nm} R_{\text{out}} = J_{nm}$, where J_{nm} is the n^{th} zero of the Bessel's function of the first kind of order m (note that in reality, the solutions for a ring are a combination of Bessel functions of the first and second kind, and the discrete wave-vectors k_{nm} must be found numerically [248], but as a first approximation, we consider the ring inner diameter negligibly small compared to the outer diameter $D_{\text{in}} \ll D_{\text{out}}$, which allows us to solve these equations to the first order and to obtain the same results as for a circular resonator, i.e. a plain disk).

Next, the resonance frequency associated to these quantized wavevectors is found by "sampling" the multilayer dispersion relation of surface plasmons in the configuration metal/ dielectric 1/ dielectric 2 according to [93], where in our case the metal is gold, dielectric 1 is alumina and dielectric 2 is silicon (configuration shown on Figure 4.9a, assuming the thickness of Si semi-infinite, which is justified if we are looking at the surface plasmon polariton in the gap). We thus calculate the multilayer dispersion relation given by solving the following transcendental equation [249]:

$$\tanh(k_1 g) = -\frac{1 + \varepsilon_2 k_m / (\varepsilon_m k_2)}{\varepsilon_2 k_1 / (\varepsilon_1 k_2) + \varepsilon_1 k_m / (\varepsilon_m k_1)} \tag{4.5}$$

where "tanh" is the hyperbolic tangent function, $k_i = \sqrt{k^2 - \omega^2 / c^2 \varepsilon_i}$, with $i = 1, 2$ for dielectrics 1 or 2 and $i = m$ for the metal substrate, and g is the thickness of the dielectric 1 (the metal and dielectric 2 are considered semi-infinite). This dispersion is plotted in Figure 4.9c, corresponding in our case to $g = 10\,\text{nm}$, $\varepsilon_1 = 1.77^2$ (permittivity of Al_2O_3), $\varepsilon_2 = \varepsilon_{\text{Si}}(\omega)$ (dispersive permittivity of aSi given

below), and the metal permittivity $\varepsilon_m = \varepsilon_{\mathrm{Au}}(\omega)$ (dispersive permittivity of Au given below).

We then apply the above theory to our nanoantenna geometry. In our case, since we are looking at a gap mode which is excited by the pump laser, which has a linear polarization in our experiment, only modes with $m = 1$ can be excited due to symmetry compatibility. We find that the discrete wavevector k_{31} (which corresponds to the third zero of the Bessel function of order $m = 1$) for a radius $R_{\mathrm{out}} = 190\,\mathrm{nm}$ (vertical dashed red line in Figure 4.9c), intersects with the dispersion curve (blue curve in Figure 4.9c), at the resonance frequency 574 nm, which is in quantitative agreement with the observed resonance wavelength of the pump around $\lambda_{\mathrm{exc}} \approx 570\,\mathrm{nm}$. The spatial profile of this mode with symmetry $(n = 3, m = 1)$, calculated from Equation (4.4) with $t = 0$, is shown in Figure 4.9a.

4.6.5 Scattering cross-sections with outer radius increase

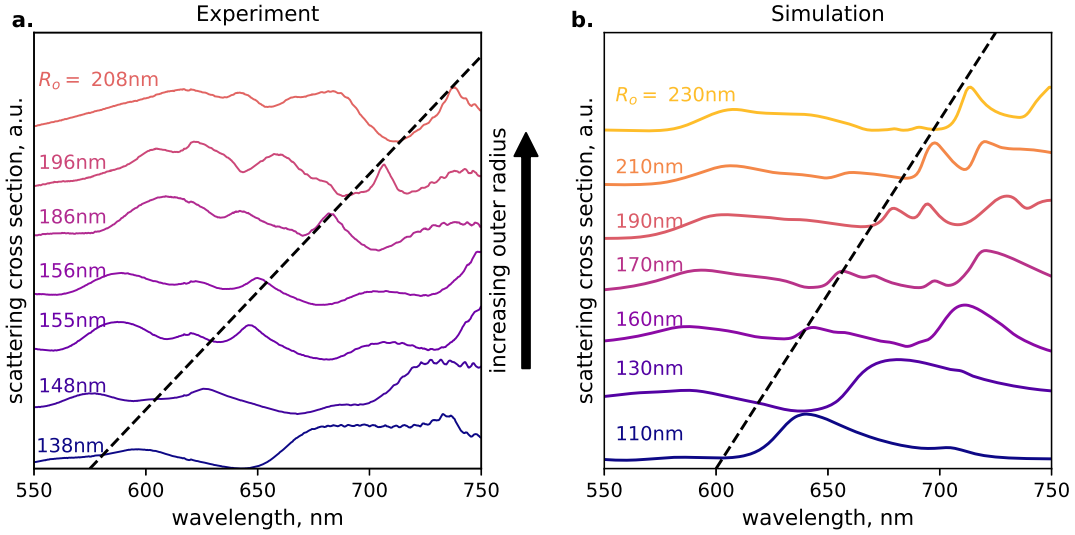

FIGURE 4.10: **a.** Experimental scattering spectra from antennas with an inner radius of about 40 nm and height of about 230 nm while increasing the outer radius. **b.** FDTD-simulated scattering spectra of antennas with a inner radius of 40 nm, height of 230 nm while increasing the outer radius.

4.6.6 Comparison between "antenna" mode of the nanoring in free space and on gold mirror cases

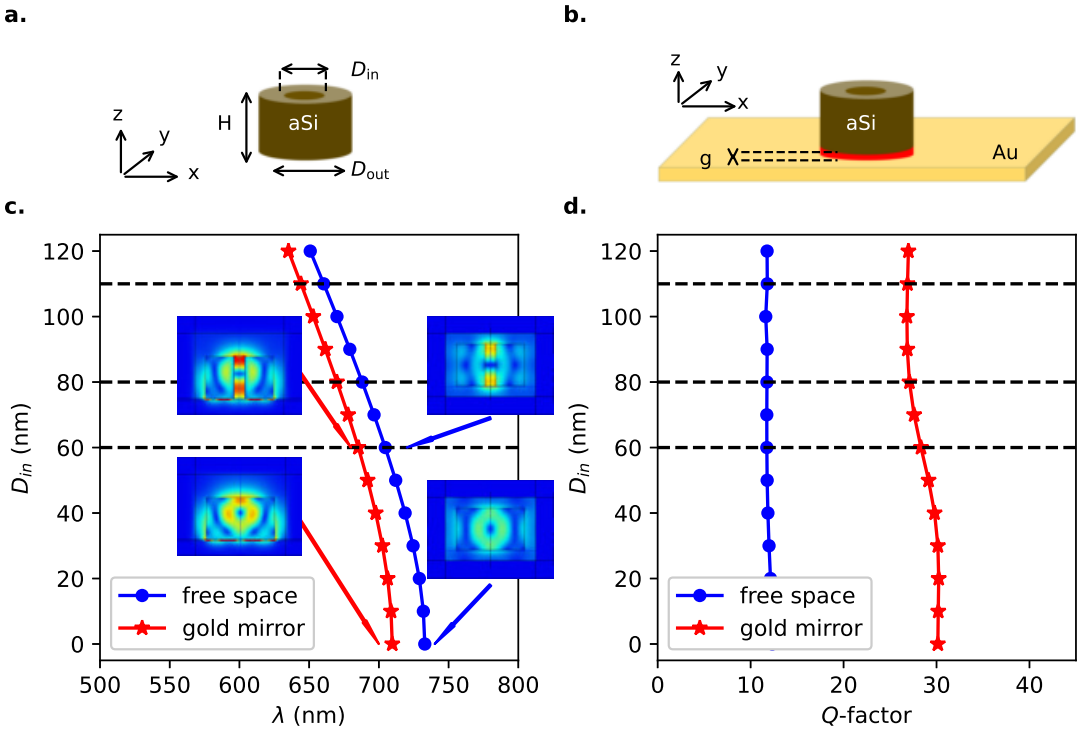

FIGURE 4.11: Comparison between the Quasi-Normal Mode (called "antenna mode") of the ring (outer diameter $D_{out} = 380\,nm$ and height $H = 230\,nm$) standing in free space (blue dots) and on top of a gold substrate (red stars). **a.** Inner (hole) diameter D_{in} *vs.* eigenwavelength (real part) of the mode. **b.** Inner diameter D_{in} *vs.* quality factor Q of the mode. The cases of $D_{in} = 60$, 80 and 110 nm, (corresponding to what we call Antenna A, B and C later on, respectively) are also highlighted (horizontal black dashed lines). The insets represent the norm of the QNM mode $|\mathbf{E}_\alpha|$ for the disk (lower inset) and the ring with $D_{in} = 60\,nm$ (upper inset) in the plane perpendicular to the substrate, passing through the center of the nanoantenna.

To understand how the presence of the metallic (gold) mirror affects the antenna mode (labelled α_1), we calculate the eigenfrequency and Q-factor of this mode when the nanoring is standing in free space, see Figure 4.11a and b, respectively. The field profiles of this mode $\mathbf{E}_\alpha$ are also shown as insets.

Now, in order to understand how quantum emitters might couple to this antenna mode, we compute the mode volume $V_\alpha(\mathbf{r})$ associated with this QNM, which is

given by the relation [250, 243]:

$$V_\alpha(\mathbf{r}) = \frac{1}{2\epsilon_0 \left(\mathbf{E}_\alpha(\mathbf{r}) \cdot \mathbf{u}\right)^2} \tag{4.6}$$

with ϵ_0 being the vacuum permittivity. One can see from Equation (4.6) that the volume quantifies the interaction between electric dipole emitters with dipole orientation along unit vector $\mathbf{u}$ and the QNM field $\mathbf{E}_\alpha(\mathbf{r})$ at the position of the emitter $\mathbf{r} = (x, y, z)$. The smaller the mode volume, the stronger the interaction.

We calculate the spatial distribution of the mode volume associated with the antenna mode, across the xy plane located 5 nm underneath the ring, in the case of a disk (lower panel) and a ring with $D_{\text{in}} = 60$ nm (upper panel), related to dipoles oriented out-of-plane (i.e. perpendicular to the plane, denoted by the symbol $\perp$) and dipoles oriented in-plane (i.e. parallel to the plane, denoted by the symbol $\parallel$).

For the standalone nanoring/nanodisk, shown in Figure 4.12a, in both cases of the disk and the ring, dipole emitters whose dipole moment orientation is in-plane are more efficiently coupled to the nanostructure in the central area, compared to emitters with out-of-plane orientation.

In stark contrast, for the nanoantenna on top of gold mirror, shown in Figure 4.12b, one can see that the coupling of in-plane dipoles, is extremely small, while the coupling of out-of-plane dipoles is substantial within a circular "band" surrounding the central area (corresponding to the hole area). This behavior can be understood partially by the fact that the presence of the metallic substrate forces the tangential component of the electric field to be near zero at the interface.

We therefore expect to induce a larger enhancement of the PL of quantum emitters distributed in the nanogap between the nanoantenna and gold mirror even after averaging over random orientations and spatial distribution, compared to the antenna alone situation, owing to a stronger coupling and also "delocalized" coupling over a larger area beneath the ring, where the emitters are localized.

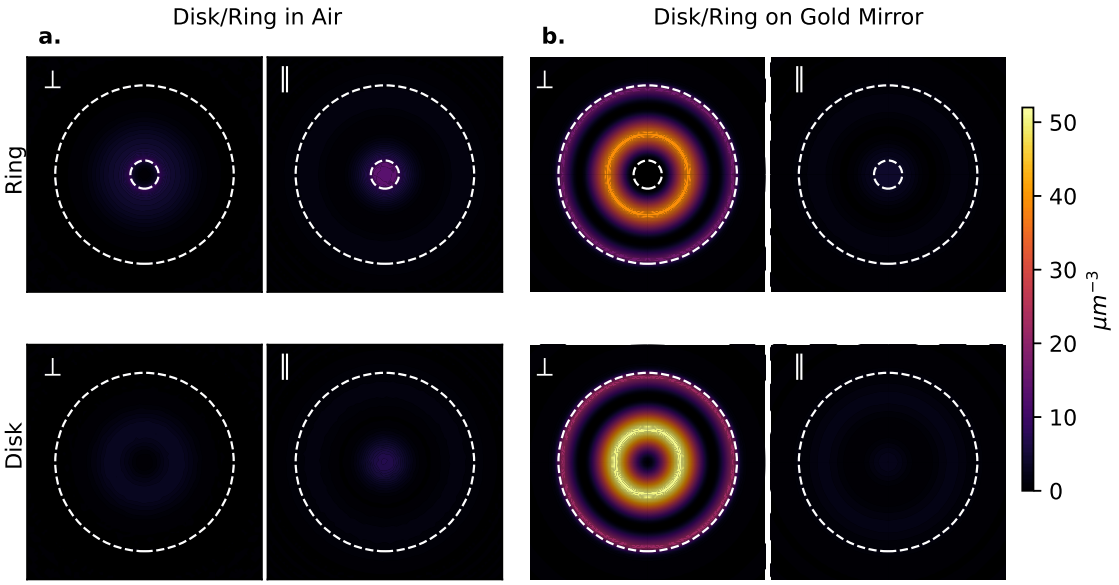

FIGURE 4.12: Spatial distribution of the real part of the inverse mode volume $\mathrm{Re}(1/V_\alpha)$ associated with the chimney mode, calculated in a plane located 5 nm below the nanoantenna, in the two cases of a disk and a ring with $D_{\mathrm{in}} = 60\,\mathrm{nm}$, both having an outer diameter $D_{\mathrm{out}} = 380\,\mathrm{nm}$ and height $H = 230\,\mathrm{nm}$ in free space. We discriminate between the out-of-plane oriented dipoles (symbol $\perp$) and the in-plane oriented dipoles (symbol $\parallel$, where in this case we averaged over x and y-orientations). The dotted white lines represents the projection onto the plane of the outer and inner diameters of the ring.

4.6.7 Field profile at the pump excitation wavelength

The local field enhancement shown in Figure 4.2 is mostly due to the z-component of the electric field, which we show in Figure 4.13. One can note the same symmetry as the mode profile of a circular resonator shown in Figure 4.9a.

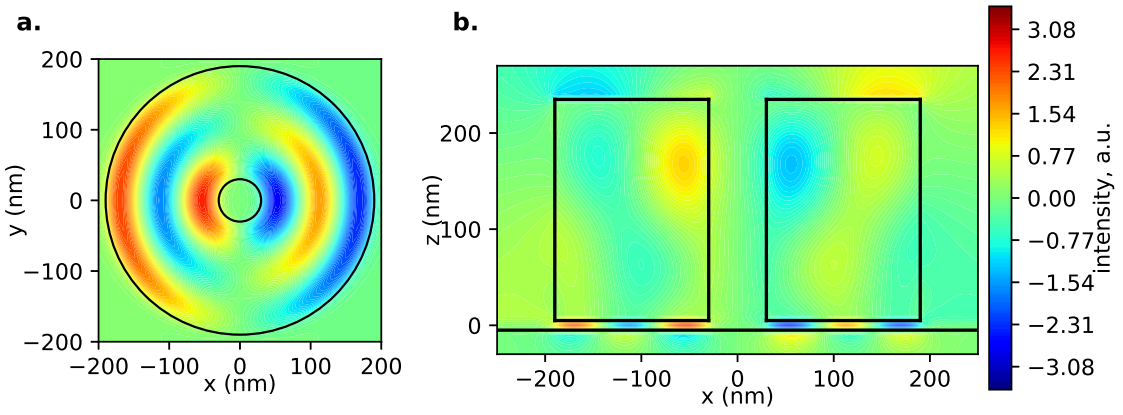

FIGURE 4.13: Component E_z of the electric field at excitation wavelength $\lambda_{\text{exc}} = 570\,\text{nm}$ in (a) the horizontal cross-section 5 nm underneath the nanoring and (b) in the vertical cross-section passing through the middle of the nanoring.

4.6.8 Laser spot size estimation

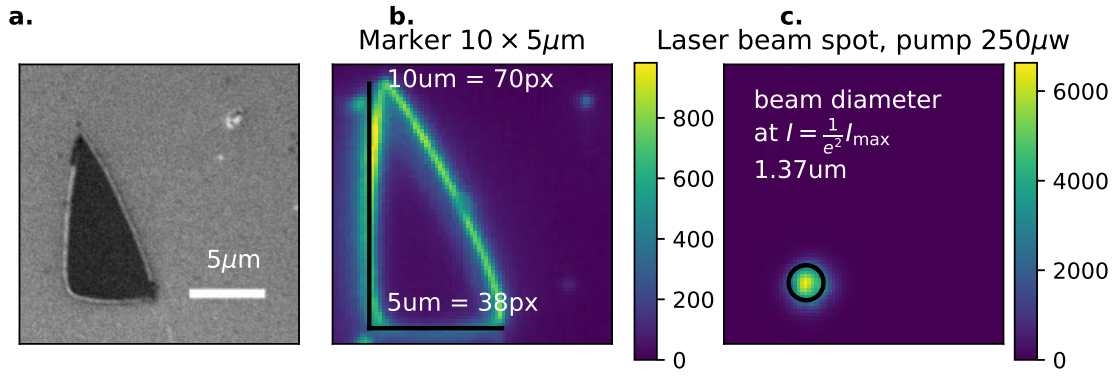

FIGURE 4.14: **a.** SEM of a marker on the sample, $10 \times 5\mu\text{m}^2$. **b.** Image of the same marker through 100× 0.9NA objective lens used to focus laser. Image scale is approximately 7 pixels per micron. **c.** Image of the laser spot using the same optical setup. Measured spot diameter at intensity $I = \frac{1}{e^2} I_{max}$ is 1.37μm.

4.6.9 Comparison between antennas A, B and C

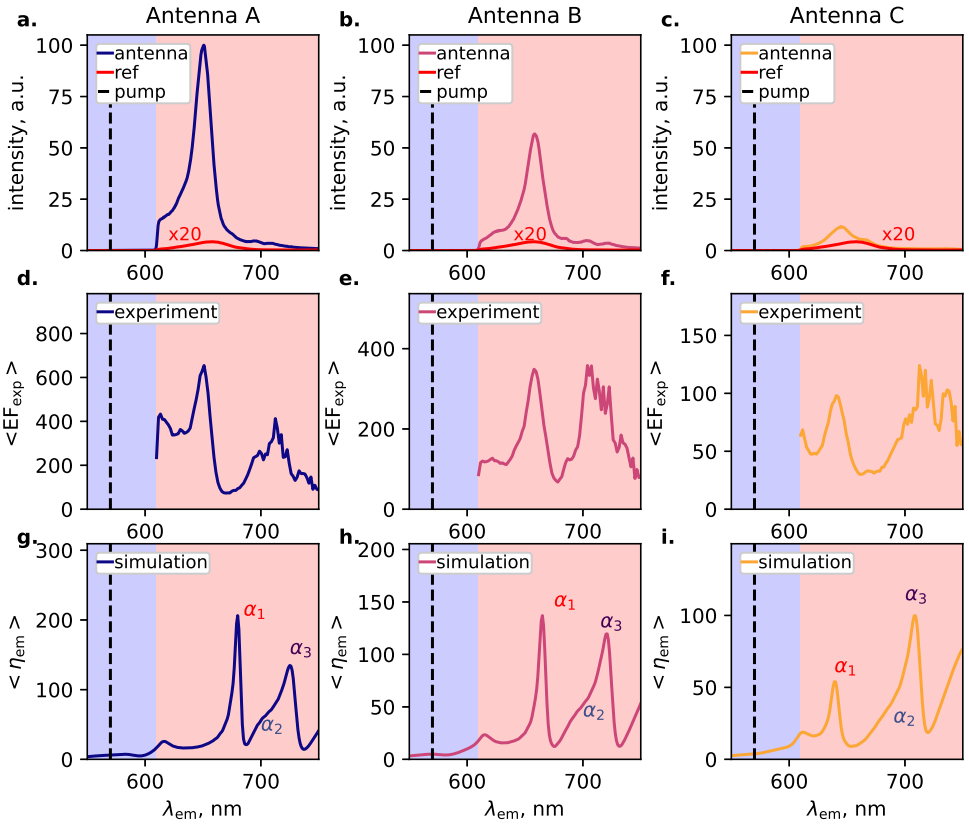

FIGURE 4.15: **a, b, c** Experimental PL signal for the nanoantennas (red) compared to Reference quantum dots (blue), **d, e, f** PL enhancement factor estimated from dividing nanoantenna PL by Reference PL. **g, h, i** Simulated enhancement factor for the nanoantennas. Dashed line in the plots indicates the pump wavelength. Blue area in the plots is filtered in the collection channel; only signal from the red area reaches the spectrometer.

In this Section, we compare three cases experimentally and in simulations of nanoantenna on top of gold mirror with same height $H = 230\,\text{nm}$, outer diameter $D_{\text{out}} = 380\,\text{nm}$, but different inner diameters: $D_{\text{in}} = 0\,, 60\,, 80\,, 110\,\text{nm}$, which we will call hereafter "Antenna A", "Antenna B" and "Antenna C", respectively.

Their experimental total enhancement spectra are shown in Figure 4.15 for a collection $\text{NA}_{\text{col}} = 0.3$ and compared with simulations of the emission enhancement in the normal direction in Figure 4.15. Experimentally, around the 650 nm, we have enhancement factors of 654, 349 and 98 for Antenna A, B and C, respectively. One can note that the positions of the peaks are slightly blue-shifted as one moves from Antenna B to Antenna C in experiment. Antenna A does not follow this trend, but

this is attributed to slight variations in the height and outer diameter compared to the nominal values.

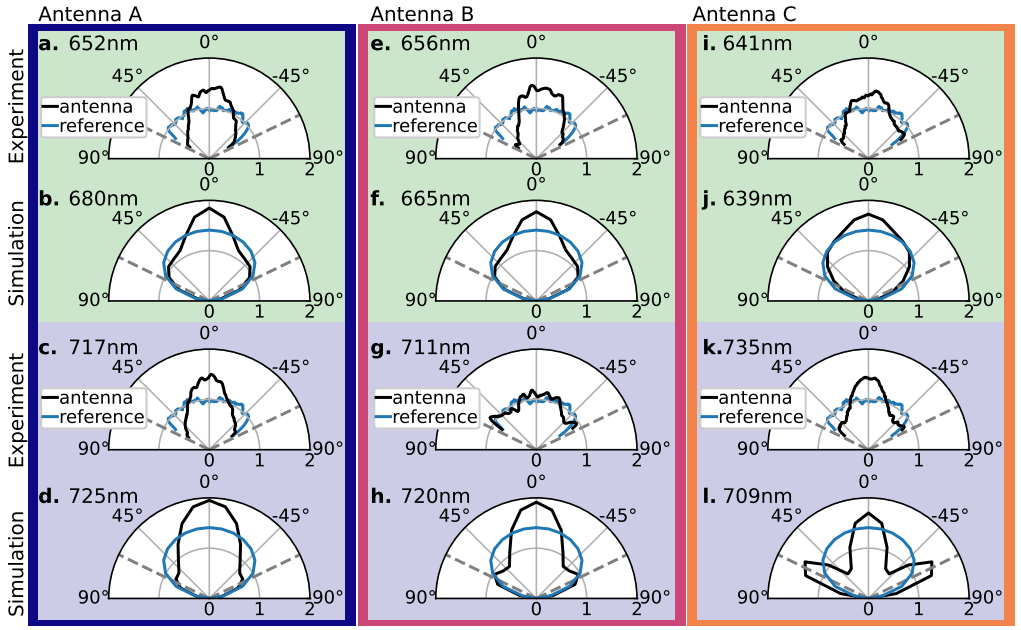

FIGURE 4.16: Experimental and simulated radiation patterns for the nanoantennas at resonant modes with the highest enhancement. Grey dashed lines show the maximum collection angle.

In simulations, the peaks are blue-shifted as on goes from Antenna A to C as expected, and the emission wavelengths corresponding to the maximum of the first resonance are at at 680 , 665 and 639 nm, respectively. The calculated emission enhancements $\langle \eta_{\text{em}} \rangle$ in the normal direction are about 206, 136 and 54, respectively.

We also show the measured and calculated radiation patterns in Figure 4.16, that reveal directivity in the out-of-plane direction in all cases.

In order to account for the different values of enhancement, we compute the Purcell factor $F_\alpha(\mathbf{r})$ associated to the antenna mode responsible for the peak around 650 nm (labelled α_1), according to the formula:

$$F_\alpha(\mathbf{r}) = \frac{6\pi c^3}{\omega_\alpha'^3} Q_\alpha \text{Re}\left(\frac{1}{V_\alpha(\mathbf{r})}\right) \tag{4.7}$$

The Purcell factor quantifies the decay rate enhancement due to the coupling with QNM α compared to free space, for an emitter located at position $\mathbf{r}$, and for a perfect matching of the emission frequency of the emitter with the real part of

the QNM eigenfrequency. We found that the maximum Purcell factor $F_\alpha^\perp(\mathbf{r}^{\max})$, corresponding to a dipole emitter with an out-of-plane orientation ($\perp$) and located at the position $\mathbf{r}^{\max}$ where $\mathrm{Re}(1/V_\alpha(\mathbf{r}^{\max}))$ is maximum (that is in the regions corresponding to the yellow/orange bands in Figure 4.12), increases as the hole diameter decreases — and is maximized for the disk case; see Table 4.2. This indicates a stronger coupling of quantum emitters with the QNM as the hole diameter decreases. We also calculated the averaged Purcell factor denoted $\langle F_\alpha \rangle$ for emitters spreading over the entire area below the ring (corresponding to the geometric cross-section of the ring $\sigma_{\mathrm{geo}} = \pi R_{\mathrm{out}}^2$ with $R_{\mathrm{out}} = D_{\mathrm{out}}/2 = 190\,\mathrm{nm}$) and with random orientations; these values are displayed in Table 4.2 together with the quality factors, Q_α. One can see that the averaged Purcell factor associated to this antenna mode decreases as the inner diameter increases, in agreement with the measured and simulated enhancement factors.

TABLE 4.2: Quasi-normal modes related quantities for four antennas configurations on gold mirror: Disk, Antenna A, Antenna B and Antenna C. Shown in the table are: the real and imaginary parts of the complex eigenfrequencies ω_α, the Q-factors associated with each mode calculated as $Q_\alpha = -\omega'_\alpha/(2\omega''_\alpha)$, the maximum Purcell factor associated to each mode calculated for a dipole with out-of-plane orientation and located in the positions where the coupling is maximum, and the averaged Purcell factor associated to each mode calculated after averaging over dipole orientations and emitter positions in the plane located below the antenna and in the middle of the gap.

	ω'_α [rad/s]	ω''_α [rad/s]	Q_α	$F_\alpha^\perp(\mathbf{r}^{\max})$	$\langle F_\alpha \rangle$
Disk	2.654×10^{15}	-4.402×10^{13}	30.1	41.6	6.5
Antenna A	2.748×10^{15}	-4.849×10^{13}	28.3	27.4	4.4
Antenna B	2.811×10^{15}	-5.188×10^{13}	27.1	22.0	3.4
Antenna C	2.923×10^{15}	-5.438×10^{13}	26.9	14.1	2.2

We also measure the lifetime for the nanoantennas A, B and C, which is shown in Figure 4.17, with the fitting parameters being displayed in Table 4.3. The "fast" decay rate enhancement is about 1.43, 1.11 and 1.43 for Antennas A, B and C, respectively and the "slow" decay rate enhancement is 1.86, 1.18 and 1.3 for A, B and C, respectively. Assuming an homogeneous distribution of QD orientations, the average decay rate enhancement is just the average of the "fast" and "slow" enhancements, giving 1.65, 1.15 and 1.37 average decay rate enhancements for Antennas A, B and C, which corresponds to the averaged Purcell factor discussed in the earlier. Note that this is the "total" Purcell factor, which is different from the

"modal" Purcell factor calculated in Table 4.2 which is calculated for the antenna mode only.

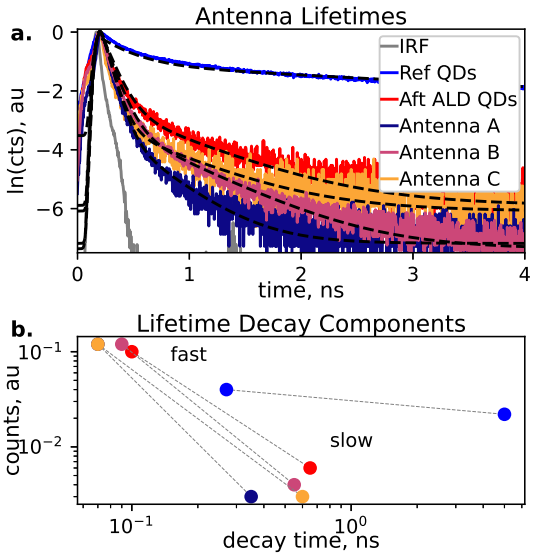

FIGURE 4.17: **a.** Measured and fit lifetime signal from nanoantennas and reference quantum dots. Grey curve is the instrument response function. Blue curve is freshly spin-coated quantum dots lifetime. Red curve is the same quantum dots after ALD. Dark blue, violet and orange curves are the lifetime signals from Antennas A, B and C, respectively. Grey curve is the instrument response function. PL decay was measured for a narrow spectral band, centered at 650 nm.

TABLE 4.3: Amplitude (a_1, a_2) and decay (τ_1, τ_2) components of the bi-exponential fitting used to the the experimental lifetime measurements.

	a_1, a.u.	τ_1, ns	a_2, a.u.	τ_2, ns
Antenna A	0.12	0.07	0.004	0.35
Antenna B	0.12	0.09	0.004	0.55
Antenna C	0.12	0.07	0.003	0.60

We summarized the different calculated and measured enhancement factors in Table 4.4, and found very good qualitative agreement between experiment and calculations.

TABLE 4.4: Comparison between calculated and measured averaged fluorescence enhancement factors. The "theoretical" enhancement factor $\langle \mathrm{EF_{th}} \rangle$ is calculated based on Equation (4.2), where all the contributing ratios are computed theoretically, except the ratio between the lifetimes τ_0/τ, which is taken from the experimental measured values. The "experimental" enhancement factor $\langle \mathrm{EF_{exp}} \rangle$ is extracted from the measured photoluminescence based on Equation (4.3). All the quantities that depend on the excitation wavelength and emission wavelength are taken at $\lambda_{\mathrm{exc}} = 570\,\mathrm{nm}$ and $\lambda_{\mathrm{em}} \approx 650\,\mathrm{nm}$, respectively. The theoretical enhancement factor is calculated for a collection $\mathrm{NA_{col}} = 0$, while experimentally we integrate the signal over a non-null NA of $\mathrm{NA_{col}} = 0.3$.

	$\langle \gamma_{\mathrm{exc}}/\gamma^0_{\mathrm{exc}} \rangle$	$\langle \mathrm{D_{em}}/\mathrm{D^0_{em}} \rangle$	$\langle \gamma_{\mathrm{r}}/\gamma^0_{\mathrm{r}} \rangle$	$\langle \tau_0/\tau \rangle$	$\langle \mathrm{EF_{th}} \rangle$	$\langle \mathrm{EF_{exp}} \rangle$
Antenna A	7.3	1.31	156.2	1.79	841	654
Antenna B	5.0	1.26	107.9	1.17	585	349
Antenna C	3.8	1.21	43.9	1.12	183	98

4.6.10 Optical constants of amorphous silicon and gold

We fit our experimental data of the optical constants of our amorphous Si (i.e. refractive index n and extinction coefficient κ, obtained via ellipsometry measurements, shown in Figure 4.18a,b), by a Lorentz model with 1 pole (or oscillator), which is in a quantitative agreement with the experimental data for wavelengths $\lambda > 550\,\mathrm{nm}$. The complex permittivity $\varepsilon = \varepsilon' + \mathrm{i}\varepsilon''$, which is related to the optical constants by the relations $\varepsilon' = n^2 - \kappa^2$ and $\varepsilon'' = 2n\kappa$, that we use in the case of Si reads:

$$\varepsilon_{\mathrm{Si}}(\omega) = \varepsilon_{\infty,\mathrm{Si}}\left[1 - \frac{\omega_{p,\mathrm{Si}}^2}{\omega^2 - \omega_{0,\mathrm{Si}}^2 + \mathrm{i}\omega\gamma_{\mathrm{Si}}}\right] \tag{4.8}$$

with $\varepsilon_{\infty,\mathrm{Si}} = 1$, $\omega_{p,\mathrm{Si}} = 15 \times 10^{15}\,[\mathrm{rad/s}]$, $\omega_{0,\mathrm{Si}} = 5 \times 10^{15}\,[\mathrm{rad/s}]$, and $\gamma_{\mathrm{Si}} = 0.3 \times 10^{15}\,[\mathrm{rad/s}]$.

In the case of the Au substrate, we did not measure the optical constants and assumed that they correspond closely to the values measured by Johnson and Christy [197]. In order to fit these experimental data, we used a Lorentz-Drude model with 2 poles (oscillators), which is also in a quantitative agreement with the experimental data for wavelengths $\lambda > 550\,\mathrm{nm}$ (see Figure 4.18c,d). The complex permittivity that we use in the case of Au reads:

$$\varepsilon_{\mathrm{Au}}(\omega) = \varepsilon_{\infty,\mathrm{Au}}\left[1 - \frac{\omega_{p,1,\mathrm{Au}}^2}{\omega^2 + \mathrm{i}\omega\gamma_{1,\mathrm{Au}}} - \frac{\omega_{p,2,\mathrm{Au}}^2}{\omega^2 - \omega_{0,2,\mathrm{Au}}^2 + \mathrm{i}\omega\gamma_{2,\mathrm{Au}}}\right] \tag{4.9}$$

with $\varepsilon_{\infty,\mathrm{Au}} = 6$, $\omega_{p,1,\mathrm{Au}} = 5.37 \times 10^{15}\,[\mathrm{rad/s}]$, $\gamma_{1,\mathrm{Au}} = 6.216 \times 10^{13}\,[\mathrm{rad/s}]$, $\omega_{p,2,\mathrm{Au}} = 2.2636 \times 10^{15}\,[\mathrm{rad/s}]$, $\omega_{0,2,\mathrm{Au}} = 4.572 \times 10^{15}\,[\mathrm{rad/s}]$, and $\gamma_{2,\mathrm{Au}} = 1.332 \times 10^{15}\,[\mathrm{rad/s}]$.

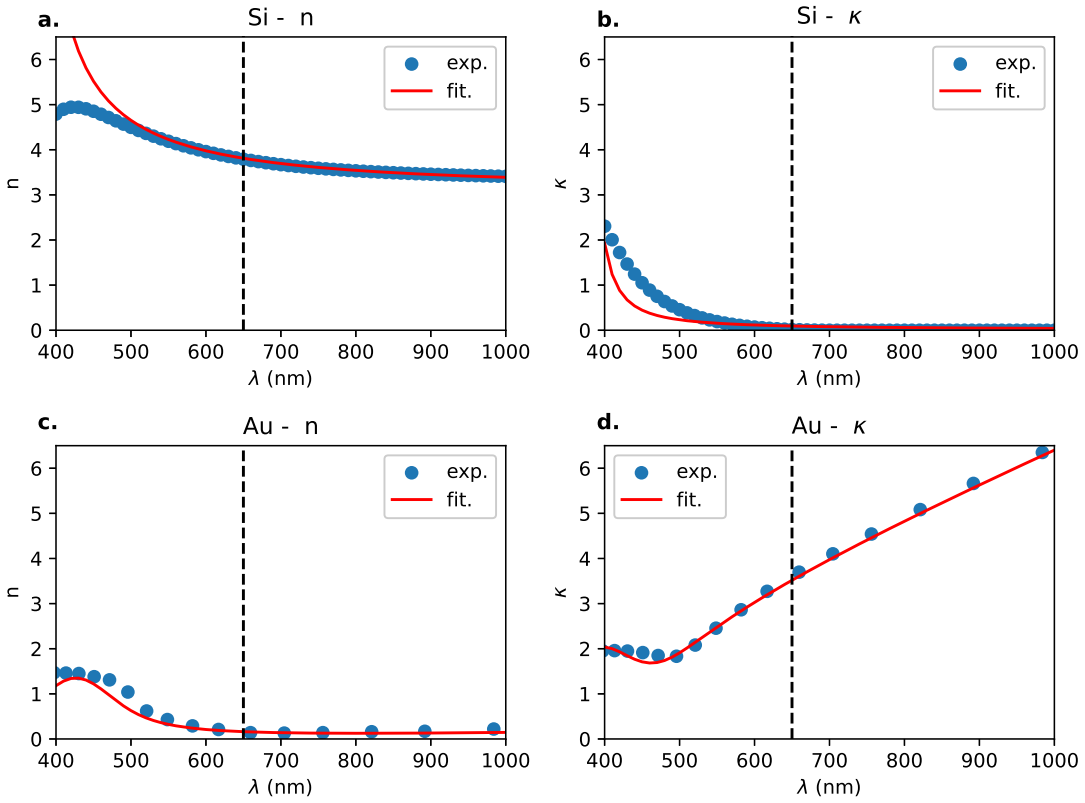

FIGURE 4.18: Fitting of refractive index n (**a**) and extinction coefficient κ (**b**) of the amorphous silicon used for the fabrication of the nanoantennas, and of the gold used for the substrate (**c** and **d**). The fitting parameters for the analytical curves (red lines) are given in the Methods section. The experimental data (blue points) were obtained via ellipsometry measurements in the case of silicon, and taken from Ref. [197] in the case of gold. The wavelength of maximum emission of the quantum dots at 650 nm is also shown (vertical black dashed line).

4.7 Methods

4.7.1 Fabrication

The whole antenna structure process flow is shown in Figure 4.19. Details of each step of the process are given below:

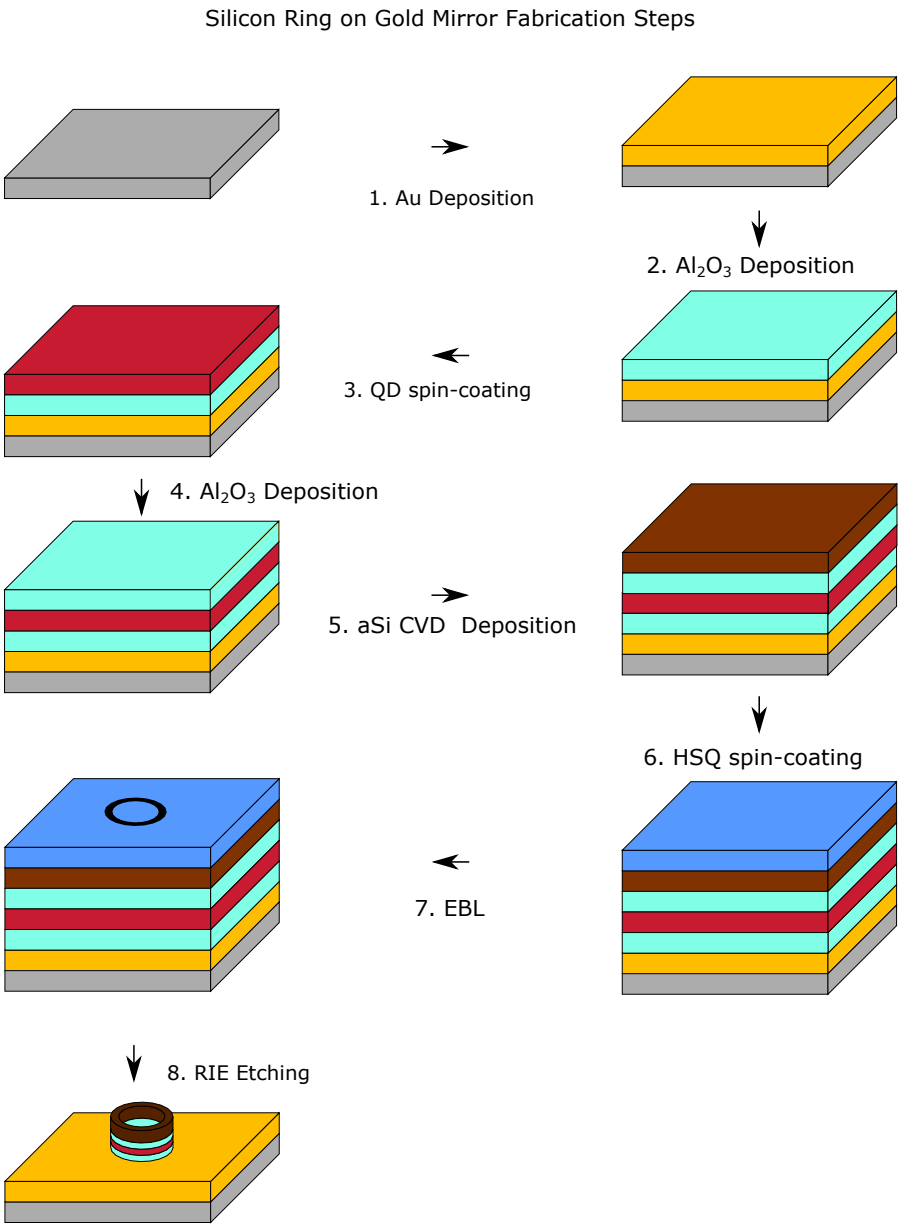

FIGURE 4.19: Schematic showing nanoantenna fabrication steps

1. We deposited a 100 nm gold thin film onto a silicon substrate with a 5 nm titanium adhesion layer by EBPVD (Denton Explorer) at a rate of 0.1Å/s.

2. Next, using ALD (Beneq TFS 200), we deposited several nanometers (30 cycles) of alumina from trimethylaluminum and H_2O precursors at 120°C.

3. After that, a layer of CdSe/ZnS alloyed quantum dots [239] were spin-coated at 2000 rpm for 1 min from a solution of 5 mg QDs per mL in toluene (shown on Figure 4.1c).

4. The quantum dots were then covered by another layer of alumina (30 cycles), this time using ALD at a temperature of 80°C.

5. For the ring structure, we deposited an $\approx$ 230 nm thick film of amorphous silicon by ICP-CVD (Oxford PlasmaPro 100) at 80°C from a SiH_4 precursor (45 sccm SiH_4 and 30 sccm Ar at 8 mTorr process pressure, 50 W RF power at 20 DC forward bias and 3000 W ICP RF power).

6. Hydrogen silsesquioxane e-beam resist (Dow Corning XR-1541-06), spin-coated at 5000 rpm for 1 min, and a change dissipation layer (Espacer 300AX01), spin coated at 1500 rpm for 1 min, were used for the EBL writing.

7. EBL (Elionix ELS-7000) was performed at an acceleration voltage 100 kV and a current of 500 pA, with a dose of $\approx 300\,mC/cm^2$. The sample was then developed in a NaOH/NaCl salty solution (1% wt. /4% wt. in de-ionized water) for 60 s and then rinsed by de-ionized water to stop the development.

8. The final structure created by ICP-RIE etching (Oxford Plasmalab 100) using chlorine gas, with a slight over etch to etch any quantum dots not protected by the silicon structures (22 sccm Cl_2 at 5 mTorr process pressure, 100 W RF power and 300 W ICP RF power).

4.7.2 Optical Characterization

The same optical setup, as described in Chapter 2, Section 2.8.3, was used.

All optical measurements were performed in a microspectrometer setup, based on an inverted microscope (Nikon Ti-U) and a spectrometer system (Andor SR-303i spectrograph with a 150 lines/mm grating coupled to a 400 × 1600 pixel Andor Newton 971 EMCCD). Incident light was focused on the sample by a 100× objective lens with a 0.9NA (Nikon LU Plan Fluor). Signal collected by the same objective lens was then projected onto the spectrograph entrance slit with a width of 250 μm.

4.7.2.1 Dark-field scattering measurements:

For dark-field scattering, white light from a halogen lamp was used to excite the sample, with the central low-$\vec{k}$ portion of the beam blocked from entering the objective lens, meaning only light scattered by the nanoantennas was collected and sent to the spectrograph. Reflectance of an silver mirror was used as the Reference.

4.7.2.2 Photoluminescence spectroscopy:

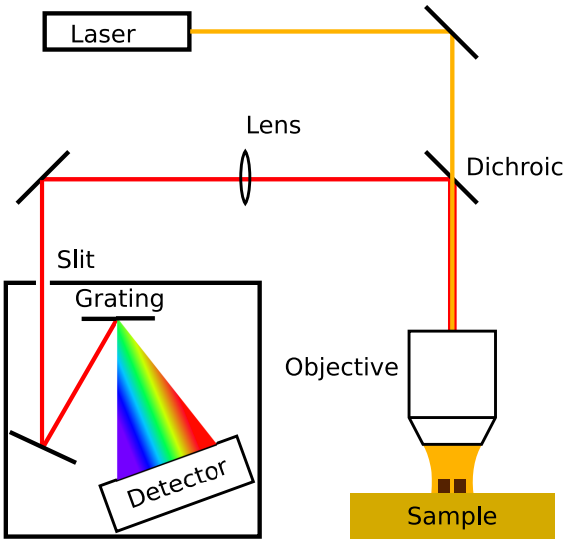

FIGURE 4.20: Schematic of photoluminescence measurement setup.

For photoluminescence measurements, a supercontinuum source (SuperK Power, NKT Photonics) with band-pass filter (SuperK Varia, NKT Photonics), pulse duration 70 ps, 78 MHz repetition rate was used to excite PL. The band-pass filter was

used to scan the pump wavelength from 488 to 588 nm with a 10 nm bandwidth. Average pump power was maintained at $\approx 250\,\mu$W. The pump laser was focused onto the sample substrate by the same 100× 0.9 NA objective lens, resulting in an approximately $1.2\,\mu$m diameter laser spot (see Section 4.6.8) for details on the method used to estimate the laser spot size). A 610 nm long pass filter was used to cut off any pump laser light in the collection beam path, the 610 nm cut-off can be clearly seen in all the photoluminescence curves on Figure 4.4 and in Figure 4.7, Figure 4.8a and Figure 4.15.

A schematic of the setup used for photoluminescence measurements is shown on Figure 4.20.

See Chapter 4, Section 2.8.3.1.

4.7.2.3 Back-focal-plane imaging

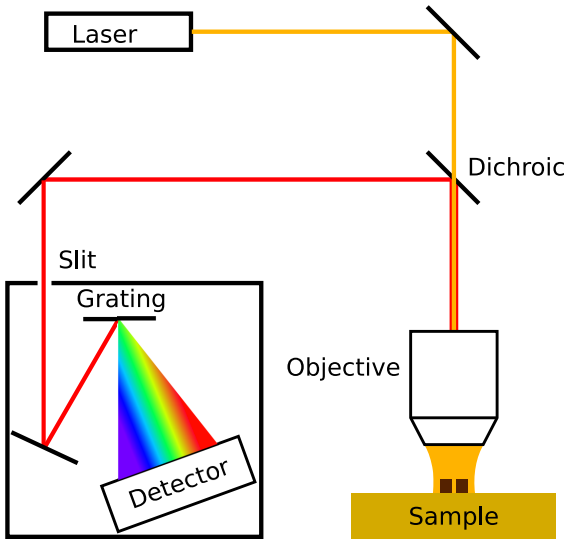

FIGURE 4.21: Schematic of photoluminescence back focal plane measurement setup.

To capture back-focal-plane images, the same 100× 0.9NA objective lens was used to collect light emitted by the nanoantennas, except that, instead of the image plane, the back focal plane of the objective was projected onto a CCD. The maximum collected angle, according to $NA = n \sin\theta$, and in our case, $n = 1$ (air), is about $\theta = 64.2°$. A schematic of the setup in shown on Figure 4.21.

Grainy features seen in all of the back-focal-plane images are artifacts related to dust in the collection system and are unrelated to the sample.

4.7.2.4 Back-focal-plane spectroscopy

To measure angle-resolved PL spectra, the same 100× 0.9NA objective lens was used to collect light emitted by the nanoantennas, except that, instead of the image plane, the back focal plane of the objective was projected onto the spectrograph entrance slit. The maximum collected angle, according to $NA = n \sin\theta$, and in our case, $n = 1$ (air), is about $\theta = 64.2°$.

4.7.2.5 Lifetime measurements

Time-resolved photoluminescence was studied using a Picoquant Microtime 200 TCSPC system coupled to our microspectometer setup. The same supercontinuum source was used to excite the sample. Spectrally integrated PL in a narrow 5 nm range, centered at 650 nm was collected using a Si single photon avalanche photodiode. The instrument response function (IRF) was recorded using excitation light scattered from the sample, where the IRF was measured to be 77 ps. PL decay measurements were fit using reconvolution with the measured IRF by a bi-exponential function using reconvolution [247].

4.7.3 Numerical simulations

4.7.3.1 Scattering cross-sections

To compute the scattering cross-sections, we used the finite-difference time-domain (FDTD) method in Ansys Lumerical FDTD. The Si particle (nanoantenna) in the presence of Au mirror was surrounded by a Total-Field Scattered-Field (TFSF) source, which simulates a planewave excitation and allows to separate directly the scattered field from the incident field. The distance between the TFSF box and nanoantenna was set to be larger than 100 nm. The incident wave was chosen to be linearly polarized and coming at normal incidence from the top of the nanoantenna. The scattering cross-section (i.e. the power flowing out of the particle divided by the source intensity, with a unit of m^2) was calculated using six plane monitors that formed a closed box surrounding the particle and located outside the TFSF source. The distance between the monitor box and the TFSF box was about 50 nm. Note that we consider for the simulations that the gap between the Si particle and Au mirror is filled with a homogeneous medium of refractive index corresponding to the one of alumina, i.e. $n = 1.77$.

See Chapter 2, Section 2.8.1.3.

4.7.3.2 Mode calculations

The quasi-normal modes (QNMs), denoted $\mathbf{E}_\alpha(\mathbf{r})$, can be defined as an eigenvalue problem of the solution of Maxwell equations in the absence of sources:

$$\nabla \times \frac{1}{\mu_0} \nabla \times \mathbf{E}_\alpha(\mathbf{r}) = \omega_\alpha^2 \varepsilon(\mathbf{r}, \omega_\alpha) \mathbf{E}_\alpha(\mathbf{r}) \tag{4.10}$$

where $\omega_\alpha = \omega'_\alpha + \mathrm{i}\,\omega''_\alpha$ denotes the complex eigenfrequency associated with the eigenmode $\mathbf{E}_\alpha(\mathbf{r})$, and supplemented by outgoing boundary conditions (also known as the Sommerfeld radiation condition as $|\mathbf{r}| \to \infty$). Note that $\omega''_\alpha < 0$ due to the convention "$\mathrm{e}^{-\mathrm{i}\omega t}$" used for the time-harmonic fields. Here, the system is considered nonmagnetic with a vacuum permeability μ_0, and $\varepsilon(\mathbf{r}, \omega)$ denotes the relative permeability of the medium. the complex eigenwavelengths are defined as $\lambda_\alpha \equiv 2\pi c/\omega_\alpha$.

In order to solve Equation (4.10) and obtain the eigenmodes and eigenfrequencies in the configurations shown in Figure 4.1g, we employed the "QNMEig solver", developped by IOGS-CNRS [251], which, computes and normalizes the QNMs of plasmonic and photonic resonators, implemented using COMSOL Multiphysics. The QNMEig solver needs all dispersive material permittivities to be modelled by a N-pole Lorentz-Drude model, in order to reformulate Equation (4.10) into a linear eigenvalue problem (see, for example, [251]). The parameters of the Lorentz-Drude model that we used for the dispersive permittivities of amorphous silicon (nanoantenna) and gold (substrate) can be found in Section 4.6.10.

4.7.3.3 Excitation enhancement simulations

To compute the term $\eta_{\text{exc}}(\mathbf{r}, \lambda_{\text{exc}})$ in Equation (4.2) shown in Figure 4.2, we use the fact that the normalized excitation rate can be readily expressed as [252]:

$$\eta_{\text{exc}}(\mathbf{r}, \lambda_{\text{exc}}) = \left| \frac{\mathbf{u} \cdot \mathbf{E}(\mathbf{r}, \lambda_{\text{exc}})}{\mathbf{u} \cdot \mathbf{E}_0(\mathbf{r}, \lambda_{\text{exc}})} \right|^2 \tag{4.11}$$

where we recall that $\mathbf{u}$ is a unit vector showing the orientation of the emitter dipole moment, $\mathbf{r}$ is the position of the emitter, and $\mathbf{E}(\mathbf{r})$ (resp. $\mathbf{E}_0(\mathbf{r})$) is the electric field at the emitter position $\mathbf{r}$ for a given excitation source in the nanoantenna case (resp. in the Reference case). In our case, we consider illumination as a *linearly* polarized planewave coming at *normal incidence* from the top of the nanoantenna. We computed, using Ansys Lumerical FDTD, this enhancement factor by integrating the electric field intensity in the horizontal plane (i.e. parallel to the substrate) and located in the middle of the nanogap over an area corresponding to the ring horizontal cross-section, which we obtained the averaged excitation enhancement $\langle \eta_{\text{exc}} \rangle$ after averaging over all directions to account for randomly distributed and oriented dipole emitters, and normalizing by the case without Si nanoantenna.

4.7.3.4 Emission enhancement simulations

The calculations of the radiative emission enhancement $\eta_{\text{em}}(\mathbf{r}, \lambda_{\text{em}})$ from Equation (4.2) and shown in Figure 4.4 were carried out using the reciprocity principle, following the method well described in Ref. [253]. This method was implemented

in Ansys Lumerical FDTD, where planewave sources were used with two orthogonal linear polarizations to excite the nanoantenna, using the TFSF source tool. Then, the near-field response was recorded in a plane located in the middle of the gap by point monitors, distributed in an area with the same size as the nanoantenna cross-section, and with a density of $3\,600\,\mu\mathrm{m}^{-2}$ (i.e. we use approximately 408 point monitors homogeneously distributed below the ring within an area of πR^2 with $R = D_{\mathrm{out}}/2 = 190\,\mathrm{nm}$). By reciprocity, the power recorded in each point monitor and calculated from the projection of the electric field along axis i ($i = x$, y or z) is equal to the emission power of light with the same polarization as the source from a point electric dipole oriented along i and located at the same position as the monitor. To obtain the averaged emission enhancement $\langle \eta_{\mathrm{em}} \rangle$ of the assembly of electric dipoles randomly oriented and distributed uniformly under the nanoantenna, the power over all orientations i and over the spatial distribution of monitors was integrated, averaged over two orthogonal linear polarizations, in the direction out-of-plane (normal incidence), and normalized to the case without nanoantenna.

4.7.3.5 Directional enhancement simulations

To obtain the directivity patterns shown in Figure 4.5, we use the same reciprocal simulations as mentioned above, and made a sweep over all angles of incidence. In Figure 4.5, we show the emission angular power distribution (averaged over two orthogonal linear polarizations).

In order to quantify the percentage of light that can be collected in the upward direction with given collection NA $\mathrm{NA}_{\mathrm{col}}$, we use the relation (see e.g. [94]):

$$\mathrm{D}_{\mathrm{em}} = \frac{\int_0^{2\pi} \int_0^{\theta_{\mathrm{col}}} p(\theta,\phi) \sin(\theta) \mathrm{d}\theta \mathrm{d}\phi}{\int_0^{2\pi} \int_0^{\pi} p(\theta,\phi) \sin(\theta) \mathrm{d}\theta \mathrm{d}\phi} \tag{4.12}$$

with $p(\theta, \phi)$ being the angular power radiated into a certain solid angle (parametrized by θ and ϕ), and θ_{col} is defined as $\theta_{\mathrm{col}} = \sin^{-1}(\mathrm{NA}_{\mathrm{col}})$. We consider only one direction for the calculated radiation patterns, which is the upward direction to be consistent with the enhancement spectra shown in Figure 4.4, that is we set $\theta_{\mathrm{col}} = 0$ in Equation (4.12).

Chapter 5

Conclusions and proposed future work

5.1 Conclusions

In this dissertation I have developed and demonstrated the full cycle of designing, fabricating and characterizing hybrid plasmonic-dielectric nanoantennas. Starting from developing optimization techniques for complex geometries, through antennas fabrication, localization of quantum emitters to couple to the antenna and culminating in demonstrating a functioning hybrid nanoantenna coupled to quantum dots showing tunable out-of-plane directivity and providing over 650× directional enhancement and over 50× Purcell factor.

Chapter 2 focuses on my original antenna design, a silicon ring and gold bowtie antenna, where the bowtie provides most of the fluorescence enhancement and the ring provides directivity. To optimize this design, several optimization techniques were developed, applicable to antennas with differing degrees of freedom. A gradient descent method, while quick and easy to understand, but limited to designs with small numbers of degrees of freedom, was used to optimize the bowtie and later cylinder dimer portion of the antenna. After adding the ring to the nanoantenna, there were too many degrees of freedom to efficiently utilize the gradient descent method, so I switched to genetic algorithms to optimize the whole structure. This required some thought to be put into figures-of-merit for the antennas,

because optimizing for fluorescence enhancement and for directivity can potentially be conflicting optimization objectives.

After optimizing the antenna, fabrication also posed challenges because of the required precision in mask alignment and bowtie parameters. At this point I decided to switch from a bowtie structure to a cylinder dimer structure because of less stringent fabrication requirements and also because the cylinder dimer offered more tunability. An issue that needed to be accounted for was proximity effects caused by the ring structure during the subsequent dimer fabrication. After fabrication issues were resolved, I switched to localising quantum emitters to couple to the antennas.

Chapter 3 focuses on the methods of quantum emitter localization that I explored. For the original ring-and-bowtie design, the most promising method was the direct creation of emitting defects in hydrogen silsesquioxane resist by e-beam exposure. This allows for very good precision, aligning the emitting HSQ almost perfectly to the nanoantenna hot spot. Unfortunately this requires an additional mask alignment step, which is the most difficult part of the whole fabrication process.

An alternative method, allowing for quantum emitter localization without any additional mask alignment, was also explored — evenly distributing emitters all over the sample substrate and then using the subsequently fabricated antenna structure as a mask to protect the emitters that I want coupled to the antenna, while removing the rest. This is a very simple method, but one that required me to change my antenna design — in the original design, the antenna hot spot was in the gap between the cylinders of the gold dimer, while this method of emitter localization would leave emitters below the antenna. This bring me to the final chapter.

In Chapter 4 I take the simple method of quantum emitter localization, and couple the emitters to a silicon ring on gold mirror antenna structure, demonstrating highly directional enhancement of quantum emitter fluorescence by a hybrid particle-on-mirror antenna. The antenna structure achieves up to 650× directional enhancement, by 8.8× pump enhancement, 1.5× directivity and 50× radiative Purcell enhancement.

5.2 Proposed future work

In my project I coupled multiple quantum dots or multiple emitting defects to nanoantennas for fluorescence and directivity demonstrations. The next logical step would be to couple a single quantum emitter to the antenna, to be able to demonstrate enhancement of a perfectly localized single photon emitter. To this effect, in Chapter 3 I explored creation of single photon emitters in hexagonal boron nitride, unfortunately, as of yet, was unable to produce stable emitters, despite attempting to reproduce results of multiple papers [124, 154].

Another vector for further research would be more robust antenna design and optimization algorithms. Since, for my project, known antennas structures were used, I only focused on the optimization of those structures, meaning that many, potentially even better, designs remained outside the scope of my thesis. Several methods for antenna design have recently been proposed, unbound by concrete geometries [120, 119], utilizing these methods could potentially allow for more efficient antenna designs.

List of Author's Awards, Patents, and Publications[1]

Journal Articles

- **Pavel A. Dmitriev***, Emmanuel Lassalle*, Lu Ding, Darren C. J. Neo, Vytautas Valuckas, Ramón Paniagua-Dominguez, Joel K.W. Yang, Hilmi Volkan Demir, Arseniy I. Kuznetsov, "Hybrid Dielectric-Plasmonic Nanoantenna with Multi-Resonances for Subwavelength Photon Sources," *Under review in ACS Photonics* [1].

Conference Presentations

- **Pavel A. Dmitriev**, Jinfa Ho, Son Tung Ha, Vytautas Valuckas, Ramón Paniagua-Dominguez, Hilmi Volkan Demir, Joel KW Yang, Arseniy I. Kuznetsov, "Hybrid metal-dielectric nanoantennas for out-of-plane fluorescence enhancement," in *ICMAT 2019, Singapore*.
- **Pavel A. Dmitriev***, Emmanuel Lassalle*, Lu Ding, Darren C. J. Neo, Vytautas Valuckas, Ramón Paniagua-Dominguez, Joel K.W. Yang, Hilmi Volkan Demir, Arseniy I. Kuznetsov, "Hybrid Dielectric-Plasmonic Nanoantennas with Dual Resonance for Fluorescence Enhancement," in *QTN 2022, Singapore*.
- **Pavel A. Dmitriev***, Emmanuel Lassalle*, Lu Ding, Zhenying Pan, Darren C. J. Neo, Vytautas Valuckas, Ramón Paniagua-Dominguez, Joel K.W. Yang, Hilmi Volkan Demir, Arseniy I. Kuznetsov, "Hybrid dielectric-plasmonic nanoantenna for efficient, bright and unidirectional photon sources," in *MH 2022, Singapore*.

[1]The superscript * indicates joint first authors

Bibliography

[1] Pavel A. Dmitriev et al. *Hybrid dielectric-plasmonic nanoantenna for efficient, bright and unidirectional photon sources*. 2022. DOI: 10.48550/ARXIV.2206.13059.

[2] Lukas Novotny and Bert Hecht. *Principles of nano-optics*. Cambridge university press, 2012.

[3] Frederick Sanger, Steven Nicklen, and Alan R Coulson. "DNA sequencing with chain-terminating inhibitors". In: *Proceedings of the national academy of sciences* 74.12 (1977), pp. 5463–5467.

[4] David L Meadows and Jerome S Schultz. "Design, manufacture and characterization of an optical fiber glucose affinity sensor based on an homogeneous fluorescence energy transfer assay system". In: *Analytica Chimica Acta* 280.1 (1993), pp. 21–30.

[5] Francis Ka-Ming Chan et al. "Fluorescence resonance energy transfer analysis of cell surface receptor interactions and signaling using spectral variants of the green fluorescent protein". In: *Cytometry: The Journal of the International Society for Analytical Cytology* 44.4 (2001), pp. 361–368.

[6] Wikimedia Commons. *File:FluorescenceFilters 2008-09-28.svg — Wikimedia Commons, the free media repository*. [Online; accessed 23-December-2021]. 2020. URL: https://commons.wikimedia.org/w/index.php?title=File:FluorescenceFilters_2008-09-28.svg&oldid=510174890.

[7] Hilmi Volkan Demir et al. "Quantum dot integrated LEDs using photonic and excitonic color conversion". In: *Nano Today* 6.6 (2011), pp. 632–647.

[8] TA Kennedy et al. "Single-Qubit Operations with the Nitrogen-Vacancy Center in Diamond". In: *physica status solidi (b)* 233.3 (2002), pp. 416–426.

[9] Christian Kurtsiefer et al. "Stable solid-state source of single photons". In: *Physical review letters* 85.2 (2000), p. 290.

[10] Gleb M Akselrod et al. "Probing the mechanisms of large Purcell enhancement in plasmonic nanoantennas". In: *Nature Photonics* 8.11 (2014), p. 835.

[11] Jako Straubel et al. "Plasmonic nanoantenna based triggered single-photon source". In: *Physical Review B* 93.19 (2016), p. 195412.

[12] Thang B Hoang, Gleb M Akselrod, and Maiken H Mikkelsen. "Ultrafast room-temperature single photon emission from quantum dots coupled to plasmonic nanocavities". In: *Nano letters* 16.1 (2015), pp. 270–275.

[13] Alberto G Curto et al. "Unidirectional emission of a quantum dot coupled to a nanoantenna". In: *Science* 329.5994 (2010), pp. 930–933.

[14] Heykel Aouani et al. "Bright unidirectional fluorescence emission of molecules in a nanoaperture with plasmonic corrugations". In: *Nano letters* 11.2 (2011), pp. 637–644.

[15] Eduard I Moiseev et al. "Light Outcoupling from Quantum Dot-Based Microdisk Laser via Plasmonic Nanoantenna". In: *ACS Photonics* 4.2 (2017), pp. 275–281.

[16] Lukas Novotny and Niek Van Hulst. "Antennas for light". In: *Nature photonics* 5.2 (2011), pp. 83–90.

[17] Shangjr Gwo et al. "Plasmonic metasurfaces for nonlinear optics and quantitative SERS". In: *Acs Photonics* 3.8 (2016), pp. 1371–1384.

[18] Alex Krasnok et al. "Spectroscopy and Biosensing with Optically Resonant Dielectric Nanostructures". In: *Advanced Optical Materials* 6.5 (2018), p. 1701094.

[19] Jian-An Huang et al. "SERS-Enabled Lab-on-a-Chip Systems". In: *Advanced Optical Materials* 3.5 (2015), pp. 618–633.

[20] George P Zograf et al. "All-optical nanoscale heating and thermometry with resonant dielectric nanoparticles for controllable drug release in living cells". In: *Laser & Photonics Reviews* 14.3 (2020), p. 1900082.

[21] George P Zograf et al. "Resonant nonplasmonic nanoparticles for efficient temperature-feedback optical heating". In: *Nano letters* 17.5 (2017), pp. 2945–2952.

[22] SV Makarov et al. "Nanoscale generation of white light for ultrabroadband nanospectroscopy". In: *Nano letters* 18.1 (2018), pp. 535–539.

[23] Pavel A Dmitriev et al. "Resonant Raman scattering from silicon nanoparticles enhanced by magnetic response". In: *Nanoscale* 8.18 (2016), pp. 9721–9726.

[24] Jon A Schuller et al. "Plasmonics for extreme light concentration and manipulation". In: *Nature materials* 9.3 (2010), p. 193.

[25] Gabriel Lozano et al. "Plasmonics for solid-state lighting: enhanced excitation and directional emission of highly efficient light sources". In: *Light: Science & Applications* 2.5 (2013), e66.

[26] Nan Zhang et al. "High sensitivity molecule detection by plasmonic nanoantennas with selective binding at electromagnetic hotspots". In: *Nanoscale* 6.3 (2014), pp. 1416–1422.

[27] Palash Bharadwaj and Lukas Novotny. "Spectral dependence of single molecule fluorescence enhancement". In: *Optics Express* 15.21 (2007), pp. 14266–14274.

[28] Nitzan Livneh et al. "Efficient collection of light from colloidal quantum dots with a hybrid metal–dielectric nanoantenna". In: *Acs Photonics* 2.12 (2015), pp. 1669–1674.

[29] Xue-Wen Chen, Vahid Sandoghdar, and Mario Agio. "Coherent interaction of light with a metallic structure coupled to a single quantum emitter: from superabsorption to cloaking". In: *Physical review letters* 110.15 (2013), p. 153605.

[30] Jean-Jacques Greffet, Marine Laroche, and François Marquier. "Impedance of a nanoantenna and a single quantum emitter". In: *Physical Review Letters* 105.11 (2010), p. 117701.

[31] Aleksandr E Krasnok et al. "Optical nanoantennas". In: *Physics-Uspekhi* 56.6 (2013), p. 539.

[32] Alexander E Krasnok et al. "An antenna model for the Purcell effect". In: *Scientific reports* 5.1 (2015), pp. 1–16.

[33] Palash Bharadwaj, Bradley Deutsch, and Lukas Novotny. "Optical antennas". In: *Advances in Optics and Photonics* 1.3 (2009), pp. 438–483.

[34] EM PURCELL. "Spontaneous emission probabilities at radio frequencies". In: *Phys. Rev.* 69 (1946), p. 681.

[35] Elias Burstein and Claude Weisbuch. *Confined electrons and photons: New physics and applications*. Vol. 340. Springer Science & Business Media, 2012.

[36] Wei Zhou et al. "Lasing action in strongly coupled plasmonic nanocavity arrays". In: *Nature nanotechnology* 8.7 (2013), pp. 506–511.

[37] Stefan A Maier. "Plasmonic field enhancement and SERS in the effective mode volume picture". In: *Optics Express* 14.5 (2006), pp. 1957–1964.

[38] A Femius Koenderink. "On the use of Purcell factors for plasmon antennas". In: *Optics letters* 35.24 (2010), pp. 4208–4210.

[39] Fengwen Wang et al. "Maximizing the quality factor to mode volume ratio for ultra-small photonic crystal cavities". In: *Applied Physics Letters* 113.24 (2018), p. 241101.

[40] Wolfgang Becker. "Fluorescence lifetime imaging–techniques and applications". In: *Journal of microscopy* 247.2 (2012), pp. 119–136.

[41] A Femius Koenderink. "Single-photon nanoantennas". In: *ACS photonics* 4.4 (2017), pp. 710–722.

[42] Lukas Novotny. "Effective wavelength scaling for optical antennas". In: *Physical review letters* 98.26 (2007), p. 266802.

[43] Vincenzo Giannini et al. "Plasmonic nanoantennas: fundamentals and their use in controlling the radiative properties of nanoemitters". In: *Chemical reviews* 111.6 (2011), pp. 3888–3912.

[44] Mark W Knight et al. "Aluminum plasmonic nanoantennas". In: *Nano letters* 12.11 (2012), pp. 6000–6004.

[45] Brock Doiron et al. “Quantifying figures of merit for localized surface plasmon resonance applications: a materials survey”. In: *Acs Photonics* 6.2 (2019), pp. 240–259.

[46] Jian-Feng Li, Chao-Yu Li, and Ricardo F Aroca. “Plasmon-enhanced fluorescence spectroscopy”. In: *Chemical Society Reviews* 46.13 (2017), pp. 3962–3979.

[47] Gleb M Akselrod et al. “Efficient nanosecond photoluminescence from infrared PbS quantum dots coupled to plasmonic nanoantennas”. In: *Acs Photonics* 3.10 (2016), pp. 1741–1746.

[48] Thang B Hoang, Gleb M Akselrod, and Maiken H Mikkelsen. “Ultrafast room-temperature single photon emission from quantum dots coupled to plasmonic nanocavities”. In: *Nano letters* 16.1 (2016), pp. 270–275.

[49] Rohit Chikkaraddy et al. “Single-molecule strong coupling at room temperature in plasmonic nanocavities”. In: *Nature* 535.7610 (2016), p. 127.

[50] Denis G Baranov et al. “Novel nanostructures and materials for strong light–matter interactions”. In: *ACS Photonics* 5.1 (2017), pp. 24–42.

[51] Lev Dykman and Nikolai Khlebtsov. “Gold nanoparticles in biomedical applications: recent advances and perspectives”. In: *Chemical Society Reviews* 41.6 (2012), pp. 2256–2282.

[52] Andrea Alù and Nader Engheta. “Wireless at the nanoscale: optical interconnects using matched nanoantennas”. In: *Physical review letters* 104.21 (2010), p. 213902.

[53] Andrea Alu and Nader Engheta. “Tuning the scattering response of optical nanoantennas with nanocircuit loads”. In: *Nature photonics* 2.5 (2008), p. 307.

[54] Hadi Eghlidi et al. “Resolution and enhancement in nanoantenna-based fluorescence microscopy”. In: *Nano letters* 9.12 (2009), pp. 4007–4011.

[55] Thomas S van Zanten, Maria J Lopez-Bosque, and Maria F Garcia-Parajo. “Imaging Individual Proteins and Nanodomains on Intact Cell Membranes with a Probe-Based Optical Antenna”. In: *Small* 6.2 (2010), pp. 270–275.

[56] Mathieu Mivelle, Thomas S van Zanten, and Maria F Garcia-Parajo. “Hybrid photonic antennas for subnanometer multicolor localization and nanoimaging of single molecules”. In: *Nano letters* 14.8 (2014), pp. 4895–4900.

[57] Shunping Zhang et al. “Substrate-induced Fano resonances of a plasmonic nanocube: a route to increased-sensitivity localized surface plasmon resonance sensors revealed”. In: *Nano letters* 11.4 (2011), pp. 1657–1663.

[58] Jesica V Pellegrotti et al. “Plasmonic Photothermal Fluorescence Modulation for Homogeneous Biosensing”. In: *ACS Sensors* 1.11 (2016), pp. 1351–1357.

[59] Harry A Atwater and Albert Polman. “Plasmonics for improved photovoltaic devices”. In: *Nature materials* 9.3 (2010), p. 205.

[60] Pierpaolo Spinelli et al. "Plasmonic light trapping in thin-film Si solar cells". In: *Journal of Optics* 14.2 (2012), p. 024002.

[61] Mark W Knight et al. "Photodetection with active optical antennas". In: *Science* 332.6030 (2011), pp. 702–704.

[62] Christian Enkrich et al. "Magnetic metamaterials at telecommunication and visible frequencies". In: *Physical review letters* 95.20 (2005), p. 203901.

[63] Pablo Albella et al. "Electric and magnetic field enhancement with ultralow heat radiation dielectric nanoantennas: considerations for surface-enhanced spectroscopies". In: *Acs Photonics* 1.6 (2014), pp. 524–529.

[64] Martín Caldarola et al. "Non-plasmonic nanoantennas for surface enhanced spectroscopies with ultra-low heat conversion". In: *Nature communications* 6 (2015), p. 7915.

[65] Pascal Anger, Palash Bharadwaj, and Lukas Novotny. "Enhancement and quenching of single-molecule fluorescence". In: *Physical review letters* 96.11 (2006), p. 113002.

[66] Jennifer T Choy et al. "Spontaneous emission and collection efficiency enhancement of single emitters in diamond via plasmonic cavities and gratings". In: *Applied Physics Letters* 103.16 (2013), p. 161101.

[67] Luozhou Li et al. "Efficient photon collection from a nitrogen vacancy center in a circular bullseye grating". In: *Nano letters* 15.3 (2015), pp. 1493–1497.

[68] Aleksandr Vaskin et al. "Light-emitting metasurfaces". In: *Nanophotonics* 8.7 (2019), pp. 1151–1198.

[69] Y Yermakov et al. "Effective surface conductivity of optical hyperbolic metasurfaces: from far-field characterization to surface wave analysis". In: *Scientific reports* 8.1 (2018), pp. 1–10.

[70] D Costantini et al. "Plasmonic metasurface for directional and frequency-selective thermal emission". In: *Physical Review Applied* 4.1 (2015), p. 014023.

[71] Alexander E Krasnok et al. "All-dielectric optical nanoantennas". In: *Optics Express* 20.18 (2012), pp. 20599–20604.

[72] Isabelle Staude and Jörg Schilling. "Metamaterial-inspired silicon nanophotonics". In: *Nature Photonics* 11.5 (2017), pp. 274–284.

[73] Arseniy I Kuznetsov et al. "Optically resonant dielectric nanostructures". In: *Science* 354.6314 (2016).

[74] Arseniy I Kuznetsov et al. "Magnetic light". In: *Scientific reports* 2.1 (2012), pp. 1–6.

[75] Yuan Hsing Fu et al. "Directional visible light scattering by silicon nanoparticles". In: *Nature communications* 4 (2013), p. 1527.

[76] Boris S Luk'yanchuk et al. "Optimum forward light scattering by spherical and spheroidal dielectric nanoparticles with high refractive index". In: *ACS Photonics* 2.7 (2015), pp. 993–999.

[77] Isabelle Staude et al. “Tailoring directional scattering through magnetic and electric resonances in subwavelength silicon nanodisks”. In: *ACS nano* 7.9 (2013), pp. 7824–7832.

[78] Debabrata Sikdar, Wenlong Cheng, and Malin Premaratne. “Optically resonant magneto-electric cubic nanoantennas for ultra-directional light scattering”. In: *Journal of Applied Physics* 117.8 (2015), p. 083101.

[79] Zhaogang Dong et al. “Silicon Nanoantenna Mix Arrays for a Trifecta of Quantum Emitter Enhancements”. In: *Nano Letters* (2021).

[80] ED Palik and G Ghosh. “Handbook of optical constants of solids (New York: Academic)”. In: (1985).

[81] Kevin Luke et al. “Broadband mid-infrared frequency comb generation in a Si 3 N 4 microresonator”. In: *Optics letters* 40.21 (2015), pp. 4823–4826.

[82] David E Aspnes and AA Studna. “Dielectric functions and optical parameters of si, ge, gap, gaas, gasb, inp, inas, and insb from 1.5 to 6.0 ev”. In: *Physical review B* 27.2 (1983), p. 985.

[83] Takahiro Kawashima et al. “Optical properties of hexagonal GaN”. In: *Journal of applied physics* 82.7 (1997), pp. 3528–3535.

[84] Pablo Albella et al. “Low-loss electric and magnetic field-enhanced spectroscopy with subwavelength silicon dimers”. In: *The Journal of Physical Chemistry C* 117.26 (2013), pp. 13573–13584.

[85] Sergey I Lepeshov et al. “Hybrid nanophotonics”. In: *Physics-Uspekhi* 61.11 (2019), p. 1035.

[86] Toshihiko Shibanuma et al. “Efficient third harmonic generation from metal–dielectric hybrid nanoantennas”. In: *Nano letters* 17.4 (2017), pp. 2647–2651.

[87] Jinfa Ho et al. “Highly directive hybrid metal–dielectric Yagi-Uda nanoantennas”. In: *ACS nano* 12.8 (2018), pp. 8616–8624.

[88] Aili Maimaiti et al. “Low-Loss Hybrid High-Index Dielectric Particles on a Mirror for Extreme Light Confinement”. In: *Advanced Optical Materials* 8.6 (2020), p. 1901820.

[89] Evgenia Rusak et al. “Hybrid nanoantennas for directional emission enhancement”. In: *Applied Physics Letters* 105.22 (2014), p. 221109.

[90] Qing Wang et al. “Hybrid photonic-plasmonic molecule based on metal/Si disks”. In: *Optics Express* 21.9 (2013), pp. 11037–11047.

[91] Hao Wang et al. “Janus magneto–electric nanosphere dimers exhibiting unidirectional visible light scattering and strong electromagnetic field enhancement”. In: *ACS nano* 9.1 (2015), pp. 436–448.

[92] Heiko Linnenbank et al. “Second harmonic generation spectroscopy on hybrid plasmonic/dielectric nanoantennas”. In: *Light: Science & Applications* 5.1 (2016), e16013.

[93] Yi Yang et al. "Low-loss plasmonic dielectric nanoresonators". In: *Nano letters* 17.5 (2017), pp. 3238–3245.

[94] A Barreda et al. "Metal, dielectric and hybrid nanoantennas for enhancing the emission of single quantum dots: A comparative study". In: *Journal of Quantitative Spectroscopy and Radiative Transfer* 276 (2021), p. 107900.

[95] Song Sun et al. "Metal–dielectric hybrid dimer nanoantenna: Coupling between surface plasmons and dielectric resonances for fluorescence enhancement". In: *The Journal of Physical Chemistry C* 121.23 (2017), pp. 12871–12884.

[96] Yinhui Kan et al. "Directional Off-Normal Photon Streaming from Hybrid Plasmon-Emitter Coupled Metasurfaces". In: *ACS Photonics* 7.5 (2020), pp. 1111–1116.

[97] Sebastian KH Andersen et al. "Hybrid plasmonic bullseye antennas for efficient photon collection". In: *Acs Photonics* 5.3 (2018), pp. 692–698.

[98] Nitzan Livneh et al. "Highly directional room-temperature single photon device". In: *Nano letters* 16.4 (2016), pp. 2527–2532.

[99] Ugo Stella et al. "Enhanced directional light emission assisted by resonant Bloch Surface Waves in circular cavities". In: *ACS Photonics* 6.8 (2019), pp. 2073–2082.

[100] R Levy. "Iterative design of antenna structures". In: *The Deep Space Network Progress Report* (1972), pp. 100–111.

[101] Douglas H Werner and Suman Ganguly. "An overview of fractal antenna engineering research". In: *IEEE Antennas and propagation Magazine* 45.1 (2003), pp. 38–57.

[102] Mohammad Ali Dorostkar, Mohammad Tariqul Islam, and Rezaul Azim. "Design of a novel super wide band circular-hexagonal fractal antenna". In: *Progress In Electromagnetics Research* 139 (2013), pp. 229–245.

[103] Will PMN Keizer. "Large planar array thinning using iterative FFT techniques". In: *IEEE Transactions on Antennas and Propagation* 57.10 (2009), pp. 3359–3362.

[104] J Michael Johnson and Yahya Rahmat-Samii. "Genetic algorithm optimization and its application to antenna design". In: *Proceedings of IEEE Antennas and Propagation Society International Symposium and URSI National Radio Science Meeting*. Vol. 1. IEEE. 1994, pp. 326–329.

[105] Hou-Tong Chen, Antoinette J Taylor, and Nanfang Yu. "A review of metasurfaces: physics and applications". In: *Reports on progress in physics* 79.7 (2016), p. 076401.

[106] Sensong An et al. "Multifunctional metasurface design with a generative adversarial network". In: *Advanced Optical Materials* 9.5 (2021), p. 2001433.

[107] Fufang Wen, Jiaqi Jiang, and Jonathan A Fan. "Robust freeform metasurface design based on progressively growing generative networks". In: *ACS Photonics* 7.8 (2020), pp. 2098–2104.

[108] Christopher Yeung et al. “Elucidating the behavior of nanophotonic structures through explainable machine learning algorithms”. In: *ACS Photonics* 7.8 (2020), pp. 2309–2318.

[109] Zhaxylyk A Kudyshev et al. “Machine learning–assisted global optimization of photonic devices”. In: *Nanophotonics* 10.1 (2021), pp. 371–383.

[110] Dayu Zhu et al. “Building multifunctional metasystems via algorithmic construction”. In: *ACS nano* 15.2 (2021), pp. 2318–2326.

[111] Zhaocheng Liu et al. “Tackling Photonic Inverse Design with Machine Learning”. In: *Advanced Science* 8.5 (2021), p. 2002923.

[112] Clément Majorel et al. “Deep learning enabled strategies for modelling of complex aperiodic plasmonic metasurfaces of arbitrary size”. In: *arXiv preprint arXiv:2110.02109* (2021).

[113] Nicholas J Dinsdale et al. “Deep learning enabled design of complex transmission matrices for universal optical components”. In: *ACS Photonics* 8.1 (2021), pp. 283–295.

[114] Peter R Wiecha et al. “Deep learning in nano-photonics: inverse design and beyond”. In: *Photonics Research* 9.5 (2021), B182–B200.

[115] Thorsten Feichtner, Oleg Selig, and Bert Hecht. “Plasmonic nanoantenna design and fabrication based on evolutionary optimization”. In: *Optics express* 25.10 (2017), pp. 10828–10842.

[116] Peter R Wiecha et al. “Design of plasmonic directional antennas via evolutionary optimization”. In: *Optics express* 27.20 (2019), pp. 29069–29081.

[117] Peter R Wiecha and Otto L Muskens. “Deep learning meets nanophotonics: a generalized accurate predictor for near fields and far fields of arbitrary 3D nanostructures”. In: *Nano letters* 20.1 (2019), pp. 329–338.

[118] Peter R Wiecha et al. “Evolutionary multi-objective optimization of colour pixels based on dielectric nanoantennas”. In: *Nature nanotechnology* 12.2 (2017), pp. 163–169.

[119] Jonathan Trisno et al. “Applying machine learning to the optics of dielectric nanoblobs”. In: *Advanced Photonics Research* 1.2 (2020), p. 2000068.

[120] Sandro Mignuzzi et al. “Nanoscale design of the local density of optical states”. In: *Nano letters* 19.3 (2019), pp. 1613–1617.

[121] Shunfa Liu, Kartik Srinivasan, and Jin Liu. “Nanoscale Positioning Approaches for Integrating Single Solid-State Quantum Emitters with Photonic Nanostructures”. In: *Laser & Photonics Reviews* (2021), p. 2100223.

[122] Tim Schroder et al. “Fiber-integrated diamond-based single photon source”. In: *Nano letters* 11.1 (2011), pp. 198–202.

[123] Andreas W Schell et al. “A scanning probe-based pick-and-place procedure for assembly of integrated quantum optical hybrid devices”. In: *Review of Scientific Instruments* 82.7 (2011), p. 073709.

[124] Joshua Ziegler et al. “Deterministic quantum emitter formation in hexagonal boron nitride via controlled edge creation”. In: *Nano letters* 19.3 (2019), pp. 2121–2127.

[125] Christian D Dieleman et al. “Universal direct patterning of colloidal quantum dots by (extreme) ultraviolet and electron beam lithography”. In: *Nanoscale* 12.20 (2020), pp. 11306–11316.

[126] Reuben M Bakker et al. “Nanoantenna array-induced fluorescence enhancement and reduced lifetimes”. In: *New Journal of Physics* 10.12 (2008), p. 125022.

[127] Humberto R Gutiérrez et al. “Extraordinary room-temperature photoluminescence in triangular WS2 monolayers”. In: *Nano letters* 13.8 (2013), pp. 3447–3454.

[128] Lin Liu et al. “Strong plasmon–exciton interactions on nanoantenna array–monolayer WS2 hybrid system”. In: *Advanced Optical Materials* 8.5 (2020), p. 1901002.

[129] Battulga Munkhbat et al. “Electrical control of hybrid monolayer tungsten disulfide–plasmonic nanoantenna light–matter states at cryogenic and room temperatures”. In: *ACS nano* 14.1 (2020), pp. 1196–1206.

[130] Jorge Cuadra et al. “Observation of tunable charged exciton polaritons in hybrid monolayer WS2- plasmonic nanoantenna system”. In: *Nano letters* 18.3 (2018), pp. 1777–1785.

[131] Johannes Kern et al. “Nanoantenna-enhanced light–matter interaction in atomically thin WS2”. In: *Acs Photonics* 2.9 (2015), pp. 1260–1265.

[132] Ahmet Fatih Cihan et al. “Silicon Mie resonators for highly directional light emission from monolayer MoS 2”. In: *Nature Photonics* 12.5 (2018), pp. 284–290.

[133] K Kuruma et al. “Position dependent optical coupling between single quantum dots and photonic crystal nanocavities”. In: *Applied Physics Letters* 109.7 (2016), p. 071110.

[134] T Kojima et al. “Accurate alignment of a photonic crystal nanocavity with an embedded quantum dot based on optical microscopic photoluminescence imaging”. In: *Applied Physics Letters* 102.1 (2013), p. 011110.

[135] Manuel Gschrey et al. “Resolution and alignment accuracy of low-temperature in situ electron beam lithography for nanophotonic device fabrication”. In: *Journal of Vacuum Science & Technology B, Nanotechnology and Microelectronics: Materials, Processing, Measurement, and Phenomena* 33.2 (2015), p. 021603.

[136] Alpan Bek et al. “Fluorescence enhancement in hot spots of AFM-designed gold nanoparticle sandwiches”. In: *Nano Letters* 8.2 (2008), pp. 485–490.

[137] Sergey V Makarov et al. “Nanoscale generation of white light for ultrabroadband nanospectroscopy”. In: *Nano letters* 18.1 (2017), pp. 535–539.

[138] Daniel Ratchford et al. “Manipulating coupling between a single semiconductor quantum dot and single gold nanoparticle”. In: *Nano letters* 11.3 (2011), pp. 1049–1054.

[139] Sadahiro Masuo et al. “Direct observation of multiphoton emission enhancement from a single quantum dot using AFM manipulation of a cubic gold nanoparticle”. In: *ACS Photonics* 3.1 (2016), pp. 109–116.

[140] Florian Werschler et al. “Efficient emission enhancement of single CdSe/CdS/PMMA quantum dots through controlled near-field coupling to plasmonic bullseye resonators”. In: *Nano letters* 18.9 (2018), pp. 5396–5400.

[141] Timothy Eastman and Da-Ming Zhu. “Adhesion forces between surface-modified AFM tips and a mica surface”. In: *Langmuir* 12.11 (1996), pp. 2859–2862.

[142] Andrey I Denisyuk, Filipp E Komissarenko, and Ivan S Mukhin. “Electrostatic pick-and-place micro/nanomanipulation under the electron beam”. In: *Microelectronic engineering* 121 (2014), pp. 15–18.

[143] Michael K Yakes et al. “Leveraging crystal anisotropy for deterministic growth of InAs quantum dots with narrow optical linewidths”. In: *Nano letters* 13.10 (2013), pp. 4870–4875.

[144] Dan Dalacu et al. “Deterministic emitter-cavity coupling using a single-site controlled quantum dot”. In: *Physical Review B* 82.3 (2010), p. 033301.

[145] Dan Dalacu et al. “Directed self-assembly of single quantum dots for telecommunication wavelength optical devices”. In: *Laser & Photonics Reviews* 4.2 (2010), pp. 283–299.

[146] Chi Zhang et al. “Light emissions from a silicon nanocrystal thin film prepared by phase separation of hydrogen silsesquioxane”. In: *Physica E: Low-dimensional Systems and Nanostructures* 89 (2017), pp. 57–60.

[147] Colin M Hessel et al. “Direct Patterning, Conformal Coating, and Erbium Doping of Luminescent nc-Si/SiO2 Thin Films from Solution Processable Hydrogen Silsesquioxane”. In: *Advanced Materials* 19.21 (2007), pp. 3513–3516.

[148] Wen-Jie Zhou et al. “Optical properties of high photoluminescence silicon nanocrystals embedded in SiO2 matrices obtained by annealing hydrogen silsesquioxane”. In: *Optical Materials* 84 (2018), pp. 874–878.

[149] Raffaello Mazzaro, Francesco Romano, and Paola Ceroni. “Long-lived luminescence of silicon nanocrystals: from principles to applications”. In: *Physical chemistry chemical physics* 19.39 (2017), pp. 26507–26526.

[150] Mehran Kianinia et al. “Robust Solid State Quantum System Operating at 800 K”. In: *CLEO: Applications and Technology*. Optical Society of America. 2017, JTu5A–24.

[151] LJ Martínez et al. “Efficient single photon emission from a high-purity hexagonal boron nitride crystal”. In: *Physical review B* 94.12 (2016), p. 121405.

[152] Gabriele Grosso et al. "Tunable and high-purity room temperature single-photon emission from atomic defects in hexagonal boron nitride". In: *Nature communications* 8.1 (2017), pp. 1–8.

[153] Samuel Grenadier et al. "Dry etching techniques for active devices based on hexagonal boron nitride epilayers". In: *Journal of Vacuum Science & Technology A: Vacuum, Surfaces, and Films* 31.6 (2013), p. 061517.

[154] Zai-Quan Xu et al. "Single photon emission from plasma treated 2D hexagonal boron nitride". In: *Nanoscale* 10.17 (2018), pp. 7957–7965.

[155] Toan Trong Tran et al. "Robust multicolor single photon emission from point defects in hexagonal boron nitride". In: *ACS nano* 10.8 (2016), pp. 7331–7338.

[156] Noah Mendelson et al. "Identifying carbon as the source of visible single-photon emission from hexagonal boron nitride". In: *Nature Materials* 20.3 (2021), pp. 321–328.

[157] Nicola Palombo Blascetta et al. "Nanoscale imaging and control of hexagonal boron nitride single photon emitters by a resonant nanoantenna". In: *Nano letters* 20.3 (2020), pp. 1992–1999.

[158] Clarisse Fournier et al. "Position-controlled quantum emitters with reproducible emission wavelength in hexagonal boron nitride". In: *Nature Communications* 12.1 (2021), pp. 1–6.

[159] Ali Bagheri and Jianyong Jin. "Photopolymerization in 3D printing". In: *ACS Applied Polymer Materials* 1.4 (2019), pp. 593–611.

[160] En-Shinn Wu et al. "Two-photon lithography for microelectronic application". In: *Optical/Laser Microlithography V*. Vol. 1674. International Society for Optics and Photonics. 1992, pp. 776–782.

[161] Shoji Maruo, Osamu Nakamura, and Satoshi Kawata. "Three-dimensional microfabrication with two-photon-absorbed photopolymerization". In: *Optics letters* 22.2 (1997), pp. 132–134.

[162] J Serbin et al. "Femtosecond laser-induced two-photon polymerization of inorganic–organic hybrid materials for applications in photonics". In: *Optics letters* 28.5 (2003), pp. 301–303.

[163] Jesper Serbin, Aleksandr Ovsianikov, and Boris Chichkov. "Fabrication of woodpile structures by two-photon polymerization and investigation of their optical properties". In: *Optics Express* 12.21 (2004), pp. 5221–5228.

[164] Kosei Ueno et al. "Nanoparticle plasmon-assisted two-photon polymerization induced by incoherent excitation source". In: *Journal of the American Chemical Society* 130.22 (2008), pp. 6928–6929.

[165] Simon O'Kane. "Quasi-analytic modal expansion methods for optical modelling of cylindrical nanostructures in GaN LEDs". PhD thesis. University of Bath, 2015.

[166] David A Powell. "Interference between the modes of an all-dielectric metaatom". In: *Physical Review Applied* 7.3 (2017), p. 034006.

[167] John B Schneider. *Understanding the FDTD method*. 2010. URL: `https://github.com/john-b-schneider/uFDTD`.

[168] Ardavan F Oskooi et al. "MEEP: A flexible free-software package for electromagnetic simulations by the FDTD method". In: *Computer Physics Communications* 181.3 (2010), pp. 687–702.

[169] Lumerical. "FDTD Solutions". In: (). URL: `http://www.lumerical.com/tcad-products/fdtd`.

[170] PJ Schuck et al. "Improving the mismatch between light and nanoscale objects with gold bowtie nanoantennas". In: *Physical review letters* 94.1 (2005), p. 017402.

[171] Anika Kinkhabwala et al. "Large single-molecule fluorescence enhancements produced by a bowtie nanoantenna". In: *Nature Photonics* 3.11 (2009), p. 654.

[172] Anika A Kinkhabwala et al. "Fluorescence correlation spectroscopy at high concentrations using gold bowtie nanoantennas". In: *Chemical Physics* 406 (2012), pp. 3–8.

[173] Arseniy Kuznetsov and Yuan Hsing Fu. *Antenna, assembly, and methods of forming the same*. US Patent 10,873,135. Dec. 2020.

[174] Johnathan Yik et al. *Antenna, antenna array, and methods of forming the same*. International Publication Number, WO2020171771A1. Aug. 2020.

[175] Vladimir A Zenin et al. "Engineering nanoparticles with pure high-order multipole scattering". In: *ACS Photonics* 7.4 (2020), pp. 1067–1075.

[176] Tianhua Feng et al. "All-dielectric hollow nanodisk for tailoring magnetic dipole emission". In: *Optics letters* 41.21 (2016), pp. 5011–5014.

[177] Jan A Snyman and Daniel N Wilke. *Practical Mathematical Optimization: Basic Optimization Theory and Gradient-Based Algorithms*. Vol. 133. Springer, 2018.

[178] Regina Burachik et al. "Full convergence of the steepest descent method with inexact line searches". In: *Optimization* 32.2 (1995), pp. 137–146.

[179] KC Kiwiel and K Murty. "Convergence of the steepest descent method for minimizing quasiconvex functions". In: *Journal of Optimization Theory and Applications* 89.1 (1996), pp. 221–226.

[180] Ya-xiang Yuan. "A new stepsize for the steepest descent method". In: *Journal of Computational Mathematics* (2006), pp. 149–156.

[181] Juan C Meza. "Steepest descent". In: *Wiley Interdisciplinary Reviews: Computational Statistics* 2.6 (2010), pp. 719–722.

[182] Jörg Fliege and Benar Fux Svaiter. "Steepest descent methods for multicriteria optimization". In: *Mathematical methods of operations research* 51.3 (2000), pp. 479–494.

[183] Dirk Thierens and David Goldberg. "Convergence models of genetic algorithm selection schemes". In: *International conference on parallel problem solving from nature*. Springer. 1994, pp. 119–129.

[184] Andy J Keane. "Genetic algorithm optimization of multi-peak problems: studies in convergence and robustness". In: *Artificial Intelligence in Engineering* 9.2 (1995), pp. 75–83.

[185] Dinabandhu Bhandari, CA Murthy, and Sankar K Pal. "Genetic algorithm with elitist model and its convergence". In: *International journal of pattern recognition and artificial intelligence* 10.06 (1996), pp. 731–747.

[186] Jerome Andre, Patrick Siarry, and Thomas Dognon. "An improvement of the standard genetic algorithm fighting premature convergence in continuous optimization". In: *Advances in engineering software* 32.1 (2001), pp. 49–60.

[187] Matthieu Loumaigne et al. "The intrinsic luminescence of individual plasmonic nanostructures in aqueous suspension by photon time-of-flight spectroscopy". In: *Nanoscale* 7.19 (2015), pp. 9013–9024.

[188] Yuan-Fong Chou Chau et al. "Tunable optical performances on a periodic array of plasmonic bowtie nanoantennas with hollow cavities". In: *Nanoscale research letters* 11.1 (2016), pp. 1–9.

[189] Stephanie Dodson et al. "Optimizing electromagnetic hotspots in plasmonic bowtie nanoantennae". In: *The journal of physical chemistry letters* 4.3 (2013), pp. 496–501.

[190] Linhan Lin and Yuebing Zheng. "Optimizing plasmonic nanoantennas via coordinated multiple coupling". In: *Scientific reports* 5.1 (2015), pp. 1–11.

[191] Wei Ding et al. "Surface plasmon resonances in silver Bowtie nanoantennas with varied bow angles". In: *Journal of Applied Physics* 108.12 (2010), p. 124314.

[192] KB Crozier et al. "Optical antennas: Resonators for local field enhancement". In: *Journal of applied physics* 94.7 (2003), pp. 4632–4642.

[193] David P Fromm et al. "Gap-dependent optical coupling of single "bowtie" nanoantennas resonant in the visible". In: *Nano letters* 4.5 (2004), pp. 957–961.

[194] Nils Pfullmann et al. "Bow-tie nano-antenna assisted generation of extreme ultraviolet radiation". In: *New journal of Physics* 15.9 (2013), p. 093027.

[195] Chelsea Carlson and Stephen Hughes. "Dissipative modes, Purcell factors, and directional beta factors in gold bowtie nanoantenna structures". In: *Physical Review B* 102.15 (2020), p. 155301.

[196] Bedir B Yousif and Ahmed S Samra. "Optical responses of plasmonic gold nanoantennas through numerical simulation". In: *Journal of nanoparticle research* 15.1 (2013), pp. 1–15.

[197] Peter B Johnson and R-W_ Christy. "Optical constants of the noble metals". In: *Physical review B* 6.12 (1972), p. 4370.

[198] Moataz Eissa et al. “Fabrication of Si photonic waveguides by electron beam lithography using improved proximity effect correction”. In: *Japanese Journal of Applied Physics* 59.12 (2020), p. 126502.

[199] R Wüest. “Proximity-effect induced density limitations for electron-beam patterned planar photonic nanomaterials”. In: *Photonics and Nanostructures-Fundamentals and Applications* 7.4 (2009), pp. 212–219.

[200] Mustafa H Chowdhury et al. “Systematic computational study of the effect of silver nanoparticle dimers on the coupled emission from nearby fluorophores”. In: *The Journal of Physical Chemistry C* 112.30 (2008), pp. 11236–11249.

[201] Liyong Jiang et al. “Accurate modeling of dark-field scattering spectra of plasmonic nanostructures”. In: *ACS nano* 9.10 (2015), pp. 10039–10046.

[202] Melanie Mitchell. *An introduction to genetic algorithms*. MIT press, 1998.

[203] Félix-Antoine Fortin et al. “DEAP: Evolutionary Algorithms Made Easy”. In: *Journal of Machine Learning Research* 13 (Dec. 2012), pp. 2171–2175.

[204] André Meister et al. “FluidFM: combining atomic force microscopy and nanofluidics in a universal liquid delivery system for single cell applications and beyond”. In: *Nano letters* 9.6 (2009), pp. 2501–2507.

[205] Yunan Gao, Mark C Weidman, and William A Tisdale. “CdSe nanoplatelet films with controlled orientation of their transition dipole moment”. In: *Nano Letters* 17.6 (2017), pp. 3837–3843.

[206] Onur Erdem et al. “Orientation-controlled nonradiative energy transfer to colloidal nanoplatelets: Engineering dipole orientation factor”. In: *Nano Letters* 19.7 (2019), pp. 4297–4305.

[207] Suresh Narayanan, Jin Wang, and Xiao-Min Lin. “Dynamical self-assembly of nanocrystal superlattices during colloidal droplet evaporation by in situ small angle X-ray scattering”. In: *Physical review letters* 93.13 (2004), p. 135503.

[208] Huan Min et al. “Approach to fabricating a compact gold nanoparticle film with the assistance of a surfactant”. In: *Langmuir* 33.27 (2017), pp. 6732–6738.

[209] Adam James Watson et al. “Transfer of large-scale two-dimensional semiconductors: challenges and developments”. In: *2D Materials* (2021).

[210] Marina Radulaski et al. “Nanodiamond integration with photonic devices”. In: *Laser & Photonics Reviews* 13.8 (2019), p. 1800316.

[211] Asma Khalid et al. “Lifetime reduction and enhanced emission of single photon color centers in nanodiamond via surrounding refractive index modification”. In: *Scientific reports* 5.1 (2015), pp. 1–12.

[212] Matthew J Crane et al. “High-pressure, high-temperature molecular doping of nanodiamond”. In: *Science advances* 5.5 (2019), eaau6073.

[213] Tsutomu Shimizu-Iwayama et al. “Optical properties of silicon nanoclusters fabricated by ion implantation”. In: *Journal of Applied Physics* 83.11 (1998), pp. 6018–6022.

[214] Margit Zacharias et al. "Size-controlled highly luminescent silicon nanocrystals: A SiO/SiO 2 superlattice approach". In: *Applied Physics Letters* 80.4 (2002), pp. 661–663.

[215] M Glover and A Meldrum. "Effect of "buffer layers" on the optical properties of silicon nanocrystal superlattices". In: *Optical Materials* 27.5 (2005), pp. 977–982.

[216] David Jurbergs et al. "Silicon nanocrystals with ensemble quantum yields exceeding 60%". In: *Applied physics letters* 88.23 (2006), p. 233116.

[217] AL Lereu et al. "Individual gold dimers investigated by far-and near-field imaging". In: *Journal of Microscopy* 229.2 (2008), pp. 254–258.

[218] G Singh et al. "Hydrogen silsesquioxane (HSQ): a perfect negative tone resist for developing nanostructure patterns on a silicon platform". In: *Advanced Fabrication Technologies for Micro/Nano Optics and Photonics IV* 7927 (2011), pp. 233–238.

[219] Hannah L Stern et al. "Spectrally resolved photodynamics of individual emitters in large-area monolayers of hexagonal boron nitride". In: *ACS nano* 13.4 (2019), pp. 4538–4547.

[220] James Callum Stewart et al. "Quantum emitter localization in layer-engineered hexagonal boron nitride". In: *ACS nano* 15.8 (2021), pp. 13591–13603.

[221] Mehdi Abdi et al. "Color centers in hexagonal boron nitride monolayers: a group theory and ab initio analysis". In: *ACS Photonics* 5.5 (2018), pp. 1967–1976.

[222] Junkai Ren et al. "Defect-assisted photoluminescence in hexagonal boron nitride nanosheets". In: *2D Materials* 7.4 (2020), p. 045023.

[223] Xiangzhi Li et al. "Nonmagnetic quantum emitters in boron nitride with ultranarrow and sideband-free emission spectra". In: *ACS nano* 11.7 (2017), pp. 6652–6660.

[224] Johannes E Fröch et al. "Coupling hexagonal boron nitride quantum emitters to photonic crystal cavities". In: *ACS nano* 14.6 (2020), pp. 7085–7091.

[225] Zav Shotan et al. "Photoinduced modification of single-photon emitters in hexagonal boron nitride". In: *Acs Photonics* 3.12 (2016), pp. 2490–2496.

[226] Luc Museur et al. "Photoluminescence of hexagonal boron nitride: effect of surface oxidation under UV-laser irradiation". In: *Journal of luminescence* 127.2 (2007), pp. 595–600.

[227] Jon A Schuller et al. "Orientation of luminescent excitons in layered nanomaterials". In: *Nature nanotechnology* 8.4 (2013), pp. 271–276.

[228] Cuong Dang et al. "Red, green and blue lasing enabled by single-exciton gain in colloidal quantum dot films". In: *Nature nanotechnology* 7.5 (2012), pp. 335–339.

[229] Onur Erdem et al. "Thickness-tunable self-assembled colloidal nanoplatelet films enable ultrathin optical gain media". In: *Nano Letters* 20.9 (2020), pp. 6459–6465.

[230] Angang Dong et al. “Binary nanocrystal superlattice membranes self-assembled at the liquid–air interface”. In: *Nature* 466.7305 (2010), pp. 474–477.

[231] Benjamin T Diroll et al. “Smectic nanorod superlattices assembled on liquid subphases: Structure, orientation, defects, and optical polarization”. In: *Chemistry of Materials* 27.8 (2015), pp. 2998–3008.

[232] Burak Guzelturk et al. “Amplified spontaneous emission and lasing in colloidal nanoplatelets”. In: *ACS nano* 8.7 (2014), pp. 6599–6605.

[233] Fu Feng et al. “Probing the fluorescence dipoles of single cubic CdSe/CdS nanoplatelets with vertical or horizontal orientations”. In: *ACS photonics* 5.5 (2018), pp. 1994–1999.

[234] Sushant Shendre et al. “Ultrahigh-efficiency aqueous flat nanocrystals of CdSe/CdS@ Cd 1- x Zn x S colloidal core/crown@ alloyed-shell quantum wells”. In: *Nanoscale* 11.1 (2019), pp. 301–310.

[235] Whi Dong Kim et al. “Pushing the efficiency envelope for semiconductor nanocrystal-based electroluminescence devices using anisotropic nanocrystals”. In: *Chemistry of Materials* 31.9 (2019), pp. 3066–3082.

[236] Burak Guzelturk et al. “Stacking in colloidal nanoplatelets: tuning excitonic properties”. In: *ACS nano* 8.12 (2014), pp. 12524–12533.

[237] Sotirios Baskoutas and Andreas F Terzis. “Size-dependent band gap of colloidal quantum dots”. In: *Journal of applied physics* 99.1 (2006), p. 013708.

[238] Jin Young Kim et al. “25th anniversary article: colloidal quantum dot materials and devices: a quarter-century of advances”. In: *Advanced Materials* 25.36 (2013), pp. 4986–5010.

[239] Jaehoon Lim et al. “Influence of Shell Thickness on the Performance of Light-Emitting Devices Based on CdSe/Zn1-XCdXS Core/Shell Heterostructured Quantum Dots”. In: *Advanced Materials* 26.47 (2014), pp. 8034–8040.

[240] Emanuela Piscopiello et al. “Formation of epitaxial gold nanoislands on (100) silicon”. In: *Physical Review B* 78.3 (2008), p. 035305.

[241] Robert Filter et al. “Circular optical nanoantennas: an analytical theory”. In: *Physical Review B* 85.12 (2012), p. 125429.

[242] Taeyjuana Y Lyons, Denise N Williams, and Zeev Rosenzweig. “Addition of fluorescence lifetime spectroscopy to the tool kit used to study the formation and degradation of luminescent quantum dots in solution”. In: *Langmuir* 33.12 (2017), pp. 3018–3027.

[243] Philippe Lalanne et al. “Light Interaction with Photonic and Plasmonic Resonances”. In: *Laser & Photonics Reviews* 12.5 (2018), p. 1700113. DOI: https://doi.org/10.1002/lpor.201700113.

[244] Gleb M Akselrod et al. “Leveraging nanocavity harmonics for control of optical processes in 2D semiconductors”. In: *Nano Letters* 15.5 (2015), pp. 3578–3584.

[245] Korenobu Matsuzaki et al. "On quantum efficiency measurements and plasmonic antennas". In: *ACS Photonics* 8.6 (2021), pp. 1508–1521.

[246] Hiroshi Sugimoto and Minoru Fujii. "Broadband dielectric–metal hybrid nanoantenna: Silicon nanoparticle on a mirror". In: *Acs Photonics* 5.5 (2018), pp. 1986–1993.

[247] Pavel Dmitriev. *kitchenknif/lifetime_reconvolution: v0.9*. Version v0.9. Feb. 2022. DOI: 10.5281/zenodo.6198822.

[248] Peter Ceperley. Mar. 2016. URL: http://resonanceswavesandfields.blogspot.com/2016/03/all-postings-by-author-previous-3.html#eqn43.

[249] Aristeidis Karalis et al. "Surface-plasmon-assisted guiding of broadband slow and subwavelength light in air". In: *Physical review letters* 95.6 (2005), p. 063901.

[250] C. Sauvan et al. "Theory of the Spontaneous Optical Emission of Nanosize Photonic and Plasmon Resonators". In: *Phys. Rev. Lett.* 110 (23 June 2013), p. 237401. DOI: 10.1103/PhysRevLett.110.237401.

[251] Wei Yan, Rémi Faggiani, and Philippe Lalanne. "Rigorous modal analysis of plasmonic nanoresonators". In: *Physical Review B* 97.20 (2018), p. 205422.

[252] Haitao Chen et al. "Manipulation of photoluminescence of two-dimensional MoSe 2 by gold nanoantennas". In: *Scientific reports* 6.1 (2016), pp. 1–11.

[253] Shuyu Zhang et al. "Calculation of the emission power distribution of microstructured OLEDs using the reciprocity theorem". In: *Synthetic Metals* 205 (2015), pp. 127–133.